High Resolution Diode Laser Spectroscopy of Transient Species

A thesis submitted for the degree of Doctor of Philosophy

by

Martin B. Crow

Balliol College, University of Oxford

Trinity Term, 2012

High Resolution Diode Laser Spectroscopy of Transient Species

A thesis submitted for the degree of Doctor of Philosophy
Martin B. Crow
Balliol College, University of Oxford
Trinity Term 2012

Abstract

This thesis presents applications of near infrared diode lasers to high resolution spectroscopy of transient radical species. Firstly, time resolved near infrared laser gain *versus* absorption is utilised in Chapter 2 to determine the I* quantum yield following ultraviolet photolysis of iodobenzene and its fluorinated analogues. The experimental method is first confirmed by comparison with literature values of the quantum yield for iodomethane photolysis, returning a quantum yield of $\Phi(I^*) = 0.71 \pm 0.04$ in good agreement with the literature, before being applied to determine the I* quantum yield following 248 nm and 266 nm photolysis of iodobenzene ($\Phi(I^*) = 0.28 \pm 0.04$) and pentafluoroiodobenzene ($\Phi(I^*) = 0.32 \pm 0.05$). The I* quantum yields for 4-fluoroiodobenzene, 2,4-difluoroiodobenzene and 3,5-difluoroiodobenzene are also reported in order to determine the effect of selective fluorination on the dynamics of the photodissociation process. This work complements velocity-map ion imaging studies and spin-orbit resolved *ab initio* calculations of the ultraviolet photolysis of these compounds.

Chapter 3 details the development of a narrow-bandwidth tunable continuous wave ultraviolet radiation source, through sum frequency mixing of tunable near infrared diode lasers with a fixed frequency, high powered, solid state laser. The application of the UV radiation source to spectroscopy of the $\tilde{A}\ ^1A_2 - \tilde{X}\ ^1A_1$ electronic band of formaldehyde is explored, where absolute absorption cross sections are determined for rotational transitions within the $2_0^2 4_0^1$ and $2_0^2 4_0^3$ vibronic bands. The sub-Doppler resolution has allowed refinement of the rotational constants for the slowly predissociating excited state of the $2_0^2 4_0^3$ vibronic band. The lifetimes of several rotational levels is determined to be in the range 0.74 ns to 1.46 ns.

In Chapter 4 the UV radiation source developed in Chapter 3 is applied to the $A\ ^2\Sigma^+ - X\ ^2\Pi$ electronic band of the OH radical. Firstly, this source is utilised to probe a continuous supply of hydroxyl radicals using cavity-enhanced absorption spectroscopy and wavelength modulation spectroscopy. Pressure induced broadening parameters for the $Q_1(2)$ rotational transition for He, Ne, Ar and N_2 buffer gases are also measured. Following the successful application of this source to probe a continuous OH source at atmospheric pressure, the UV spectrometer is used to probe OH radicals from nitric acid photolysis at 193 nm, where the nascent speed distribution and Doppler lineshape is shown to be in excellent agreement with the literature. Time resolved absorption spectroscopy of the nascent OH fragment also returns a translational relaxation constant of $k_{\text{trans}} = (3.85 \pm 1.06) \times 10^{-10} \text{cm}^3 \text{molecule}^{-1} \text{s}^{-1}$, which is in good agreement with literature values. These preliminary results indicate the potential of this narrow-bandwidth tunable UV source as an absorption-spectroscopy-based probe of nascent Doppler profiles.

Chapter 5 presents the application of frequency-modulated radiation from a near infrared diode laser as a probe of the angular momentum polarisation of the nascent CN fragments, produced by 266 nm photolysis of ICN. These CN fragments are probed in the high rotational states of both the ground and first excited vibrational level on the

$A\ ^2\Pi - X\ ^2\Sigma^+$ electronic transition; in particular these constitute the first measurements of alignment and orientation in the first excited vibrational level at this photolysis wavelength. The alignment parameters reported for both vibrational levels are comparable, indicating that the incoherent dynamics contributing to their formation are the same. In contrast, the orientation of the $v = 1$ CN fragment is shown to be of opposite sign to that of $v = 0$ at this photolysis wavelength, although the absolute differences in their orientation parameters are similar to that observed for photolysis at 248 nm. This observation is consistent with coherent orientation arising from phase differences between wavepackets propagating on multiple excited potential energy surfaces.

Acknowledgments

I must begin this list with Grant, without his tutorials I might never have found my love of physical chemistry, despite the cryptic clues. A great many thanks to Sarah T and especially Graham, without whom this just not would have worked. Graham can and did make everything work.

I have thoroughly enjoyed my five years working in the Ritchie Group and the many wonderful people I shared that time with. Many thanks to the Monday pub crew, unintentionally misnomered as "the lads": Alex 'Never knowingly weird, fralex, Gillon, G1000, Gilly' Gilchrist for understanding my Arnie quotes, no matter how obscure; Lee 'Oh no, he's turned Leemo' Moore for suffering (and putting up) with me, in the words of the Doctor 'allons-y' there I said it; Rich 'Brick' Dear for his unending kindness and support (particularly physics based games) throughout; and Richard Walker for the many great times spent in pubs, the manor, the house and his unobtainable kongregate score. Thanks also to Stuart, Tom, Sarah, Beth, Michelle, Luca, Claire and Ed for all the fun times together, particular those who made Finland/Russia so memorable.

Many thanks to my family for all their support through the years. Most importantly, thanks to Libby for all her support and patience.

Hindrances

In no particular order: Kongregate, Xbox 360, Three Goats Heads, Sulkido, teaching, Nespresso. *Curse you all.* I couldn't have done it without you.

List of Publications

"High-Resolution Absorption Studies of the $\tilde{A}^1A_2$ - $\tilde{X}^1A_1$ $2_0^2 4_0^1$ Band of Formaldehyde"

M. B. Crow, A. Gilchrist, G. Hancock, R. Peverall, G. Richmond, G. A. D. Ritchie and S. R. Taylor

J. Phys. Chem. A **113**, 6689 (2009).

"n$\sigma^\star$ and $\pi\sigma^\star$ excited states in aryl halide photochemistry: a comprehensive study of the UV photodissociation dynamics of iodobenzene."

A. G. Sage, T. A. A. Oliver, D. Murdock, M. B. Crow, G. A. D. Ritchie, J. N. Harvey and M. N. R. Ashfold

PCCP **113**, 6689 (2011).

"UV photodissociation dynamics of iodobenzene: effects of fluorination"

D. Murdock, M. B. Crow, G. A. D. Ritchie, and M. N. R. Ashfold

J. Chem. Phys. , (2012).

Contents

List of Figures

List of Tables

Chapter 1

Introduction

In this thesis high resolution absorption spectroscopy is conducted with narrow bandwidth tunable near-infrared diode lasers to measure a selection of spectroscopic and dynamical properties of both stable and transient chemical species, the latter formed by photodissociation. Specifically, in Chapter 2 the quantum yield for forming electronically excited iodine atoms in the ultraviolet photolysis of iodobenzene and its fluorinated analogues is reported. The quantum yield is determined using diode laser gain *versus* absorption spectroscopy on a hyperfine electronic transition of iodine.

Chapter 3 details the development of a tunable continuous-wave ultraviolet radiation source based upon sum frequency generation, which combines the output of tunable near-infrared diode lasers with the output of a high-powered, fixed-frequency source operating at 532 nm. The resulting UV radiation is applied to a study of the $\tilde{A}-\tilde{X}$ electronic system in formaldehyde. The sub-Doppler resolution allows rotational transitions to be probed in the absence of instrumental broadening and the spectrometer is used to determine absolute absorption cross sections on some rotational transitions within the $2_0^2 4_0^1$ and $2_0^2 4_0^3$ vibrational bands in the $\tilde{A}-\tilde{X}$ electronic band, allowing comparison with lower resolution measurements of this atmospherically important species. In addition, the rotational constants of the higher energy $2_0^2 4_0^3$ vibronic level are optimised and predissociation lifetimes of a small selection of excited rovibrational levels reported for the first time.

The UV source developed in Chapter 3 is then applied to OH radical spectroscopy in Chapter 4 using rotationally resolved transitions within the $A\ ^2\Sigma^+ - X\ ^2\Pi$ electronic band to probe an atmospheric pressure static sample of OH using cavity enhanced absorption spectroscopy and wavelength modulation spectroscopy. In addition, pressure induced

broadening parameters are reported for the $Q_1(2)$ rotational transition for He, Ne, Ar and N_2 buffer gases. Following this, the UV source is used to probe the nascent OH fragments produced in the 193 nm photolysis of nitric acid; superthermal nascent OH speed distributions are observed and rate constants for translational relaxation reported.

Finally, Chapter 5 presents the application of near-infrared frequency modulation spectroscopy to probe the angular momentum polarisation of nascent CN fragments, produced by 266 nm photolysis of ICN. Measurements of alignment and orientation of the rotational angular momentum in the ground and first excited vibrational level of the CN product are reported and the information this reveals about the photodissociation of ICN is discussed.

1.1 Photodissociation Dynamics

The detailed dynamics of photodissociation are of fundamental interest to chemists because the photoexcitation and subsequent fragmentation processes may be considered as a half reaction with well defined initial conditions, i.e. dissociation occurs from a small set of energy and momentum states and within a restricted range of nuclear configurations which is equivalent to restricting the range of impact parameters for a bimolecular collision.

$$\mathrm{AB} + h\nu \rightarrow \mathrm{AB}^* \rightarrow \mathrm{A} + \mathrm{B} \tag{1.1}$$

Photodissociations occur *via* electronic excitation, where the electronic structure of a molecule is altered by the absorption of one or more photons and produces an excited state, AB^*. Many questions can be asked at this point: how is the photon absorbed? i.e. what is the transition probability and in which direction in the molecular frame does the transition dipole moment lie? how long does the excited state survive? what symmetry properties does the excited state possess and which internal motions promote fragmentation? Upon dissociation many more questions arise and these include: what is the chemical identity of the fragments that are formed? how do the fragments separate in terms of how their velocity and angular momentum vectors are distributed in space? how is the available energy partitioned i.e. does energy preferentially get channelled into product translational motion or is there a preference for excitation within specific internal (rotational, vibrational and electronic) modes of motion? Answering such questions is the

goal of theoretical and experimental studies of photodissociation dynamics.[1]

The observable properties which can be studied to answer these questions can be broadly defined as either *scalar* or *vector* properties. Scalar properties include such things as quantum yields, state distributions and energy distributions, whereas vector properties concern the spatial distribution of vectors such as the velocity, rotational angular momentum and electronic angular momentum (relative to the transition dipole moment of the parent). These properties are complementary and so a complete understanding of both is necessary to truly understand a photodissociation process. Examples of both scalar (Chapters 2, 3 and 4) and vector (Chapter 5) properties are presented within this thesis but we now briefly consider some examples which illustrate the information provided by measurements of both sets of properties.

1.1.1 Scalar Properties

The most basic scalar property of interest in a photodissociation process is the identity of the products of photodissociation. These are often wavelength dependent, as different pathways become active as different potential energy surfaces (PESs) become accessible at increasing excitation energies. An example of this is the ultraviolet photodissociation of formaldehyde, for which there are two product channels:

$$CH_2O + h\nu \rightarrow H_2 + CO \quad (\lambda < 360\,\text{nm}) \tag{1.2}$$

$$CH_2O + h\nu \rightarrow H + HCO \quad (\lambda < 330\,\text{nm}) \tag{1.3}$$

Both the molecular and radical products are the result of excitation to the S_1 state, internal conversion to an excited vibrational level of the ground state S_0^*, followed by dissociation.[2,3] Similarly, UV photolysis of water can occur either *via* the $\tilde{A}$ state around 157 nm leading to the OH ground state, $^2\Pi$, or *via* the $\tilde{B}$ state around 121.6 nm leading to electronically excited OH in the $^2\Sigma$ state.[1]

This wavelength dependence of the products is investigated in Chapter 2, where the quantum yield of forming electronically excited atomic iodine from photolysis of a parent compound at various wavelengths has been recorded, revealing the fraction of molecules which follow a photodissociation path towards that particular fragment. Since the elec-

tronically excited state of iodine lies $7603\,\mathrm{cm}^{-1}$ above the ground state, this affects the energy available to the cofragment.

Photodissociation processes such as:

$$AB + h\nu \rightarrow A + B \tag{1.4}$$

are subject to the law of conservation of energy:

$$\begin{aligned} E_{\text{total}} =& h\nu + E_{\text{internal}}(AB) \\ E_{\text{total}} =& E_{\text{internal}}(A) + E_{\text{trans}}(A) + E_{\text{internal}}(B) + E_{\text{trans}}(B) - D_0 \end{aligned} \tag{1.5}$$

thus the amount of energy partitioned into the products' modes of freedom comes from a fixed pool.

Measuring the amount of energy partitioned into each of these degrees of freedom aids in understanding the nature of the bond cleaving process. For example, ICN photolysis *via* the A-X transition at 248 nm produces vibrationally cold CN fragments with 95% of the fragments produced in $v = 0$, but with high rotational excitation, despite ICN being a linear molecule.[4,5] This is the result of excitation to PESs which prefer a bent geometry, causing a large amount of bending during the bond fission, resulting in a large amount of rotation in the product. The CN stretch acts like a spectator throughout the excitation, resulting in very little vibrational excitation.[6]

Once the partitioning of energy into the degrees of freedom is known, the next level of detail is the state distributions within these degrees of freedom. As discussed above, ICN photolysis at 248 nm produces rotationally hot CN fragments, but more interestingly it does so with a bimodal distribution, peaking around $N = 45$. The bimodal distribution arises due to the possibility of ground or electronically excited iodine cofragments, where the low rotational states of CN are formed with electronically excited iodine, as the dissociation process has insufficient energy to form high rotational states with excited iodine fragments.[4,5]

Quantum state distributions can reveal interesting facts about the dissociation pathway. For example, in the photolysis of CH_2O to form molecular products the CO rotational distribution peaks at $N = 45$, in agreement with conservation of angular momentum and

energy considerations. However, at higher energies, when the radical channel becomes significant, the CO rotational distribution displays a small shoulder at low rotational energies.[7] This was discovered to be due to low rotational states of CO formed in conjunction with highly vibrationally excited H_2, $v = 6, 7$, resulting in the assignment of a new photodissociation mechanism whereby the H atom formed in the radical pathway travels around the HCO fragment to strip the other H atom, leading to the molecular product by the so called 'roaming' path.[8]

These quantum state distributions help reveal the nature of the PESs involved in the dissociation. For example, H_2O photolysis at 157 nm and 122 nm produces different rotational state distributions, shown in Figure 1.1. Photolysis at 157 nm proceeds *via*

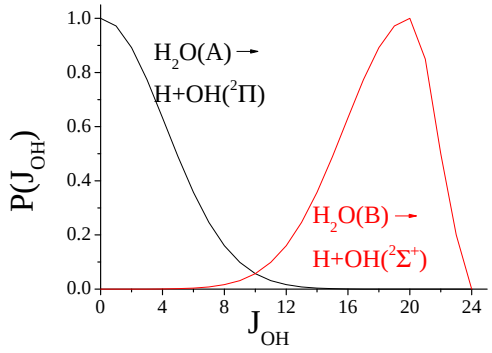

Figure 1.1: Rotational state distributions of OH($^2\Pi$) and OH($^2\Sigma$) fragments following photolysis at 157 nm and 122 nm, respectively. Reproduced from Schinke,[1] based upon the data of Andersen *et al.*[9] and Carrington.[10]

the $\tilde{A}$ state,[9] whereas photolysis at 122 nm proceeds *via* the $\tilde{B}$ state.[10] To understand the difference in the state distribution it is necessary to examine the PESs, shown in Figure 1.2, where the $\tilde{A}$ state is repulsive along the dissociation coordinate (Figure 1.2a) but has a minimum in the bending angle PES at the equilibrium bond angle (Figure 1.2b). Since the force is the negative derivative of the potential, this minimum in the rotational PES imparts very little rotational torque on the OH fragment. However, the $\tilde{B}$ state has a deep potential well along the dissociation coordinate but a highly repulsive bending angle PES, imparting a large rotational torque on the departing OH fragment.

Vector properties can provide further detail on the nature of excited state PESs and

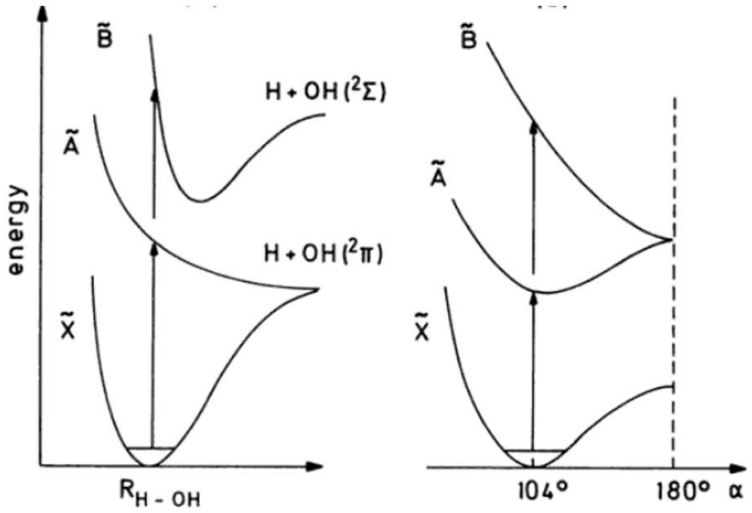

(a) (b)

Figure 1.2: Schematic cuts through the PESs for the ground and first two excited electronic states of H_2O. The dependence on the H-OH distance is given in (a) whereas (b) illustrates the dependence on the bond angle, with the equilibrium bond angle of 104° indicated. Adapted from Schinke[1] and based upon Staemmler and Palmer[11] and Theodorakopoulos *et al.*[12]

the trajectory towards the products.

1.1.2 Vector Properties

Vector properties, as the name suggests, are observables with directionality. Studies of photodissociation dynamics generally focus on three vectors: the parent transition dipole moment, $\boldsymbol{\mu}$; the fragment recoil velocity, $\mathbf{v}$; and the fragment's total angular momenta, $\mathbf{J}$, as well as the angles which relate these vectors to one another. Measurements of the relative angle (or more correctly ensemble averages of functions of these angles) between two or three of these vectors is typically called a *vector correlation*.

These vector correlations provide great insight into the dynamics of photodissociation since the dissociating photon's electric vector, ε, must interact with the dipole moment of the parent molecule. The absorption cross section depends upon the integral $|\langle\psi_f|\boldsymbol{\varepsilon}.\mu|\psi_i\rangle|^2$ where ψ_f and ψ_i are the final and initial states for the absorption process; hence, the transition dipole moment is preferentially aligned parallel to the electric vector during absorption of a photon. Therefore, measurements of the recoil velocity or angular momenta

can be referenced to the electric vector of the dissociating photon which in turn may be related to the dipole moment of the fragment.

When studying vector correlations it is necessary to consider two possible types of vector distribution: *alignment* and *orientation*. These are used to refer to the different types of spatial distribution of the photofragment's angular momentum. Alignment refers to a preferential plane for the vector to occupy, such as parallel or perpendicular to an axis, demonstrated in Figure 1.3a. Orientation refers to a preferential direction for the vector, for example parallel or anti-parallel to an axis, demonstrated in Figure 1.3b.[13]

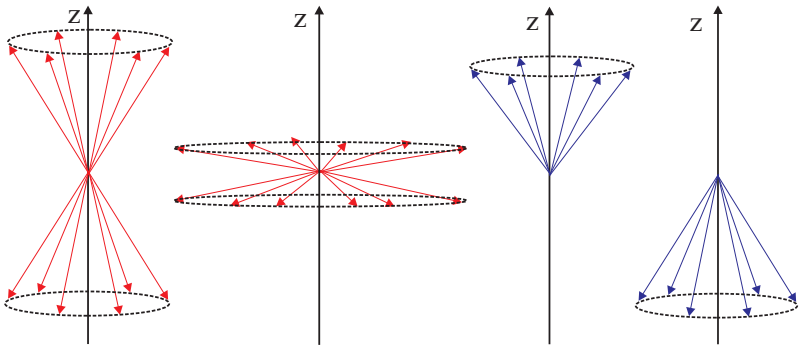

(a) Positive ($J \parallel z$) and negative ($J \perp z$) alignment

(b) Positive ($J \parallel +z$) and negative ($J \parallel -z$) orientation

Figure 1.3: Illustration of Alignment and Orientation of a vector, taken from Orr-Ewing and Zare.[13]

Physically, taking rotational angular momenta as an example, alignment refers to a preferred *plane or axis* of rotation and orientation refers to a preferred *direction* to rotate, either clockwise or counter-clockwise in the plane. Quantum mechanically, for a state of quantum number J this is equivalent to a non-statistical population distribution of the m_J levels, $P(m_J)$, for both cases, but with $P(+m_J) = P(-m_J)$ for alignment and $P(+m_J) \neq P(-m_J)$ for orientation, as illustrated in Figure 1.3.[13]

Alignment and orientation are best visualised in terms of the rotational angular momenta. However, the easiest vector correlation to visualise is the recoil anisotropy, which describes the spatial distribution of the fragment recoil velocity with respect to the electric vector of dissociating photon, and therefore can be related to electric vector of the dissociating photon, which may in turn be related to the parent transition dipole moment. As

discussed above, absorption of a dissociating photon occurs through the interaction of the photon's electric vector and the transition dipole moment of the parent. If the dissociation process is fast on the timescale of rotation, known as the axial recoil limit, [1] then the recoil direction can be related to the transition dipole moment of the parent. Slow dissociations allow the molecule time to rotate, allowing the initially well defined conditions created in the absorption process to be lost. Fast photodissociation leads to two limiting cases: fragments recoiling perpendicular to the parent transition dipole moment, $\boldsymbol{\mu}$, or parallel to it, shown in Figure 1.4. The velocity distribution about $\boldsymbol{\mu}$ for these two limitations is also illustrated in Figure 1.4 and is described by Equation 1.6, where θ is the angle between $\boldsymbol{\mu}$ and the velocity, $\mathbf{v}$, and P_2 is the second order Legendre polynomial[i]. The *translational anisotropy parameter*, β, characterises the velocity distribution according to equation 1.6. [14]

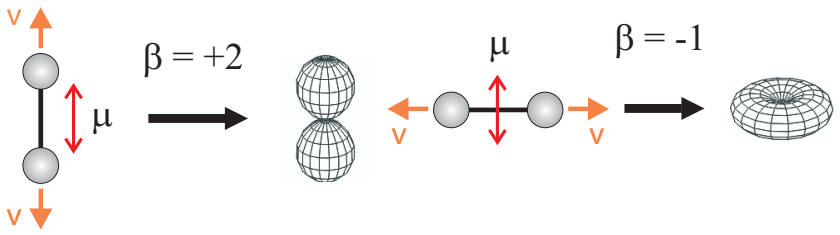

(a) Parallel transition (b) Perpendicular transition

Figure 1.4: Illustration of the limits of the recoil anisotropy of a photodissociation process.

$$\begin{aligned} P(\mathbf{v},\theta) =& \frac{1}{4\pi}\left(1+\beta P_2(\cos\theta)\right) \\ \beta =& 2\langle P_2(\cos\theta)\rangle \end{aligned} \tag{1.6}$$

Therefore, in the limit of parallel recoil $\beta = +2$, which describes a $\cos^2\theta$ distribution of $\mathbf{v}$ about $\boldsymbol{\mu}$ and in the limit of perpendicular recoil $\beta = -1$, describing a $\sin^2\theta$ distribution, summarised in Figure 1.4. These two limiting cases are known as parallel transitions and perpendicular transitions, respectively.

The limiting cases of β are not often seen and there are a number of reasons for this. Firstly, in the case of photodissociation of bent triatomic molecules, such as NO_2 and O_3,

[i] $P_2(x) = \frac{1}{2}\left(3x^2-1\right)$

the transition dipole moment may not be parallel or perpendicular to the bond axis being broken. In this case the bond angle, α, can be taken into account as in equation 1.7 and illustrated in Figure 1.5.

$$\beta = 2\langle P_2\left(\cos\left(\frac{\pi-\alpha}{2}\right)\right)\rangle \tag{1.7}$$

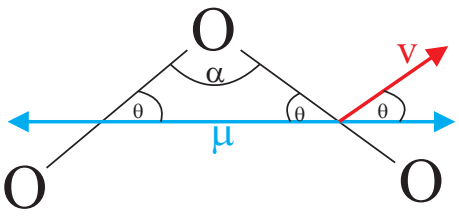

Figure 1.5: Illustration of the relationship of $\boldsymbol{\mu}$ to $\mathbf{v}$ for a bent triatomic.

Secondly, the excited state may undergo a significant amount of rotation during the dissociation. To account for this, Jonah[15,16] related the rotational frequency, ω, and the lifetime of the excited parent molecule, τ, to β according to:

$$\beta = 2\langle P_2(\cos\theta)\rangle\frac{(1+\omega^2\tau^2)}{(1+4\omega^2\tau^2)}. \tag{1.8}$$

This expression is then averaged over a Boltzmann distribution of rotational states for the parent at temperature T to give the β_{eff}:

$$\beta_{\text{eff}} = {}^1\!/_2\langle P_2(\cos\theta)\rangle\left(1+3\gamma e^{\gamma}\int_{\gamma}^{\infty}\frac{e^{-t}}{t}dt\right) \tag{1.9}$$

where

$$\gamma = 1/8kT\tau^2. \tag{1.10}$$

Thirdly, photodissociation often proceeds *via* excitation to multiple surfaces. This is the case for photolysis of ICN, studied in Chapter 5, in which the excitation is a mixture of a parallel transition to the $^3\Pi_{0+}$ and a perpendicular transition to the $^1\Pi_1$ surface.

The recoil anisotropy reveals the type of transition, either parallel or perpendicular, which gives insight into the the nature of the excited state, particularly its symmetry and whether vibrational excitation must be coupled in to make the transition allowed. The rotational anisotropy can reveal the forces and torques between the fragments as they

dissociate, leading to a greater understanding of the excited state potential.[1]

Rotational anisotropy can be discussed relative to two vectors: the parent transition dipole moment, and the recoil velocity. The $v - J$ correlation allows rotational anisotropy to be investigated even if the recoil anisotropy is lost due to long excited state lifetimes. Similar to recoil anisotropy, there exist two limits for rotational anisotropy: the rotational vectors parallel to and perpendicular to the vector it is measured against. Limiting cases of the relationship of rotational angular momentum to the recoil velocity and parent's dipole moment are shown in Figure 1.6 for a triatomic molecule ABC, cleaving the A–B bond.

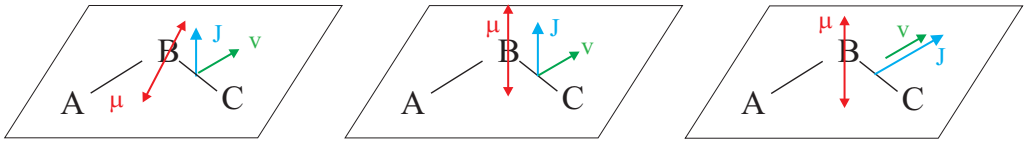

(a) $\mathbf{J} \perp \mathbf{v} \perp \boldsymbol{\mu}$ (b) $\mathbf{J} \parallel \boldsymbol{\mu}$, $\mathbf{J} \perp \mathbf{v}$ (c) $\mathbf{J} \parallel \mathbf{v}$, $\mathbf{J}$ & $\mathbf{v} \perp \boldsymbol{\mu}$

Figure 1.6: Illustration of the some limiting cases of vector coupling between rotational vector, J, the recoil velocity, ν, and the parent dipole moment, μ when cleaving the A-B bond of a bent triatomic ABC molecule. In 1.6a μ lies in the molecular plane whereas μ is perpendicular to the molecular plane in 1.6b & 1.6c.

In Figure 1.6a the dipole moment lies in the molecular plane such that on dissociation the BC fragment rotates in the molecular plane, recoiling parallel to the parent's AB bond, producing a helicopter type motion ($\mathbf{J} \perp \mathbf{v} \perp \boldsymbol{\mu}$). In Figures 1.6b and 1.6c the dipole moment is perpendicular to the molecular plane but the former results in BC rotation in the plane of the molecule ($\mathbf{J} \parallel \boldsymbol{\mu}$, $\mathbf{J} \perp \mathbf{v}$), again helicopter motion, and the latter causes rotation of BC perpendicular to the molecular plane ($\mathbf{J} \parallel \mathbf{v}$, $\mathbf{J}$ & $\mathbf{v} \perp \boldsymbol{\mu}$), producing a propeller like motion of the BC fragment.

These classical considerations of bond fission all relate to incoherent alignment of the photofragment. The orientation of the rotational angular momenta allows more detail of the excited state PESs to be explored.

1.1.3 Incoherent and Coherent Orientation of Rotational Angular Momentum

Orientation can be described as being either incoherent or coherent, with the names referring to whether it is the result of coherence effects between multiple excited state PESs. The previous discussion is limited to incoherent orientation (single state photodissociation).

Photolysis with circularly polarised radiation selectively dissociates those molecules rotating such that the transition dipole moment is aligned with the rotating electric vector of the photon. Once dissociation occurs this often results in a fragment with oriented angular momentum, carried over from the photon's angular momentum; this is known as incoherent orientation. Alternatively, photolysis may proceed *via* excitation to multiple states, such as in the case of ICl shown in Figure 1.7a. There are multiple pathways to dissociation and these can interfere; the interference effect can be accounted for by treating the pathway to the products as de Broglie waves on each surface. Upon excitation, the two waves are initially in phase; however, as they approach the products one wave proceeds through an energy barrier, thus a phase difference between the de Broglie waves is accumulated, shown in Figure 1.7b.[18] The latter origin of orientation occurs from coherence effects between the two de Broglie waves, hence the name coherent orientation.

Since orientation of the angular momentum produces a preferential direction of rotation of the fragment, certain experimental conditions need to be used to measure orientation. Linearly polarised light cannot differentiate between up and down or between left and right, only horizontal and vertical, therefore circularly polarised light must be used to differentiate between orientations. The information available from the products of a photodissociation processes varies between experimental techniques, and so these techniques need to be carefully selected to match the measurements required.

1.1.4 Experimental Techniques

This section describes the techniques that are commonly used in photodissociation studies and their advantages and disadvantages. All the techniques used in photolysis studies

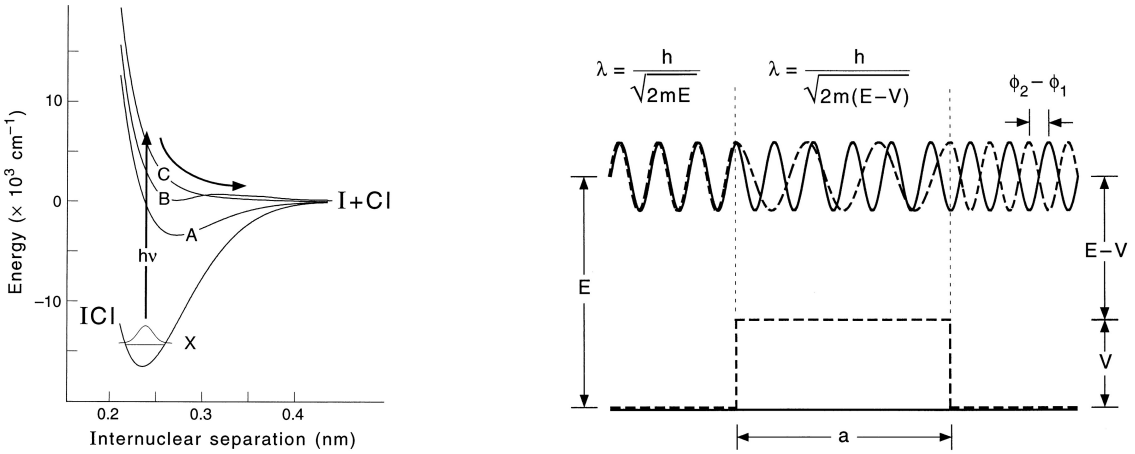

(a) Potential energy surfaces

(b) Phase difference incurred

Figure 1.7: Illustration of the origin of coherent orientation taken from Rakitzis *et al.*. (a) shows the PESs that correlate with ground state I and Cl. (b) illustrates how the phase difference is incurred between two de Broglie waves as one, the dashed line, experiences an energy barrier of height V.[18]

involve high powered, typically pulsed, laser sources which are resonant with a dissociative transition. The next step is the detection of the resulting nascent fragment, which can be performed in a number of ways.

An early method used in photodissociation studies is Photofragment Translational Spectroscopy (PTS) which uses a laser to photolyse a molecular beam and then detect one of the fragments.[19] Detection is usually performed using an electron-bombardment ionizer followed by mass spectrometry. Typically two observables are measured: the time of flight of the fragment, reported as a translational energy distribution, and the angular distribution of the fragment with respect to the electric vector of the photolysis laser. These measurements are typically performed on an atomic fragment such as H or one of the halides.[19,20]

The translational energy distribution of the detected fragment helps to elucidate the properties of the cofragment through conservation of energy and momentum. This is illustrated in Chapter 2, where the I fragment of the photolysis of aryl-iodides displays different distributions in the translational kinetic energy release which correspond to different photodissociation channels; in addition, these distributions are further split into peaks corresponding to vibrational excitation of the fragment.[21,22] Though PTS can measure vibrational distributions, it typically lacks the resolution needed to resolve individual

rotational states. However, PTS can be used to record recoil anisotropy provided the angle between the detector and molecular beam can be varied. Since this technique uses a mass spectrometer, it is generally considered a universal technique.[23]

Resonantly-Enhanced Multi-Photon Ionisation (REMPI) is similar to PTS in that a molecular beam is photolysed by a laser. However, the resulting fragment is detected using multi-photon ionisation (MPI) induced by a second laser to create an ion which is subsequently detected using a time-of-flight mass spectrometer. Typically the detection method is a subset of MPI in which a number of resonant photons cause ionisation. Usually this is performed by first exciting the molecule to a virtual state, then absorption of another photon to further excite the molecule to a resonant state before ionising with a final photon. Since all the stages in this example involve photons, this is ionisation process is known as (2+1) REMPI scheme, i.e. involves two excitation photons and one ionisation photon.

REMPI absorption schemes require excited states that are sufficiently long lived to give appreciable ionization yields, which limits the technique to specific molecular and atomic fragments, although it is still the most popular technique in reaction dynamics experiments. In addition to this, two-photon absorptions are subject to different selection rules to one-photon absorption, thus REMPI can be used where one-photon absorption schemes are forbidden. REMPI also allows access to excited states which would otherwise need vacuum-ultraviolet radiation to reach. One of the key advantages compared with PTS, is that REMPI provides vibrational and rotational state specificity and the time-of-flight profiles generated can be analysed to determine vector correlations.[24]

Time-of-flight profiles provide a one-dimensional projection of the photofragment's velocity distribution. In order to determine two-dimensional projections of the velocity distribution the technique of ion-imaging was introduced by Chandler and Houston,[25] in which a phosphor screen is used to detect the ions at the end of the time-of-flight tube, recording the positions at which the ions collide with a microchannel plate detector (MCP). Velocity Map Ion-imaging (VMI) is a further improvement over ion imaging in which ions with the same initial velocity are mapped onto the same point on the MCPs, achieved by using modified electrostatic lenses.[26] The advantage of VMI is that two-dimensional images of the velocity distribution of the ions can be generated with rotational and vibrational state specificity and the resulting images can be used to determine vector correlations. It has

therefore become the most widely applied technique for reaction dynamics and scattering experiments.[27] In Chapter 2, time-resolved near-infrared laser gain *versus* absorption spectroscopy is used to complement VMI studies of aryl-iodide compounds.

State-specific techniques are often preferable in photodissociation studies due to the greater detail available when studying line profiles of individual transitions. Therefore, a popular technique in photodissociation dynamics is the measurement of the emitted radiation following excitation by absorption, known as Laser-Induced Fluorescence (LIF). This zero background technique can be highly state specific and can be used to determine angular distributions and velocity distributions, however it does require a fluorescent excited state accessible by absorption, limiting the species that may be probed.

LIF has been extensively used in photodissociation dynamics to measure scalar and vector properties, with LIF spectra able to elucidate rotational and vibrational distributions;[28] excited state branching ratios;[29,30] and, with sub-Doppler resolution, vector correlations[31] and Zeeman quantum beats.[32,33] Recent studies utilising Zeeman quantum beat spectroscopy (ZQBS) have illustrated a wide range of uses, such as measuring rotational energy transfer and depolarisation of angular momentum of OH and NO in collisions with Ar.[34–37] Despite the large amount of information available using LIF, and the high sensitivity it affords, the requirement for a fluorescent state limits its application. Some molecules do not posses fluorescent states or, as in the case of OH, may undergo predissociation which competes with the fluorescence in some states.

Absorption spectroscopy is another available technique utilised throughout this thesis. It is an ideal detection technique for photofragments since it is universally applicable to molecules and atoms and can be highly state specific. Unlike LIF or REMPI and its derivatives, absorption spectroscopy only requires an optical transition. However, absorption spectroscopy typically lacks the combination of sensitivity and time resolution necessary to detect truly nascent photofragments. Whereas cavity techniques have the necessary sensitivity, but do not possess the time-resolution; direct absorption has the time-resolution and not the required sensitivity. Thus long path lengths are often used.[38–41]

Recently, techniques such as frequency modulation spectroscopy have been applied to photolysis studies, in particular UV photolysis of ICN.[42–48] Following from these studies frequency modulation spectroscopy has also been applied to measurements of quantum

beats in orientation and alignment of CN fragments[44] as well as depolarisation of the angular momentum and population transfer in CN collisions with Ar,[37,49,50] demonstrating the potential for absorption based techniques to probe photodissociation and collision dynamics.

1.2 Line Shape Broadening

In order to observe chemical species with absorption spectroscopy it is necessary to consider the various sources of line broadening of the spectroscopic transition. Even though these transitions often occur with well defined energy due to the highly quantised energy levels involved, the transition will not be infinitely sharp due to a variety of broadening mechanisms.

The time-energy uncertainty principle:

$$\Delta E \Delta t \geq h \tag{1.11}$$

produces a distribution of energies since the time scales of absorption or emission processes are often so short that the uncertainty in the energy must increase to compensate. This effect can often be seen in emission spectroscopy where the excited state is very short lived, but usually only contributes to the line shape rather than being the dominant broadening mechanism.[51]

The distribution of frequencies produced through this so called natural broadening is described by a Lorentzian profile, $g(x - x_c)$, where x_c is the line centre and w_L is the Lorentzian full width at half maximum (FWHM):[52]

$$g(x - x_c) = \frac{2}{(\pi w_L)} \frac{1}{\left(1 + 4\left(\frac{x - x_c}{w_L}\right)^2\right)}. \tag{1.12}$$

The natural broadening often makes a negligible contribution to line width, since environmental effects dominate. Particularly relevant to this work is Doppler broadening.

The thermal motion of the absorbing or emitting species produces a Doppler effect in the detected radiation, which contributes to the line width. This effect leads to a Gaussian

line profile centred about the spectroscopic transition,

$$g(x - x_c) = \frac{2}{w_G}\sqrt{\frac{\ln 2}{\pi}} \exp\left(-4 \ln 2 \left(\frac{(x - x_c)}{w_G}\right)^2\right), \tag{1.13}$$

using similar notation to the Lorentzian profile above but with the Gaussian FWHM, w_G, given by:

$$w_G = \sqrt{\frac{8kT \ln 2}{mc^2}} w_0, \tag{1.14}$$

where the Gaussian width depends upon the frequency of the absorbed or emitted radiation, w_0, as well as the temperature, T, and mass, m, of the moving species. This is particularly relevant to this work, in Chapters 3 and 4 the spectroscopic transitions used to probe the formaldehyde and hydroxyl radical occur in the UV, which gives a rather large frequency to the absorbed radiation, hence wide, $w_G > 2\,\text{GHz}$, Gaussian profiles are observed. Additionally, in Chapters 4 and 5 photoproducts are observed which are generated with large amounts of translational energy, hence they possess a large 'effective' temperature which leads to large Doppler shifts in the radiation.

In addition to the natural and Doppler broadening a spectral line may be broadened by collisions. These collisions may occur either with or without energy transfer between the colliding species, either *inelastic* or *elastic* collisions, respectively.

In an elastic collision the particles approach one another and the energy levels become perturbed by the particles' interaction with one another. Radiative processes occur much faster than collisions so this interaction leads to uncertainty in the energy levels, broadening the transition. This broadening is also described by a Lorentzian distribution, equation 1.12, discussed above. In addition to broadening, the interaction between the particles may have a net effect upon the transition, shifting the central frequency to higher or lower values, known as pressure-induced shift. These two effects are often known as impact broadening or collisional broadening.[51]

An inelastic collision occurs with one particle donating energy to the other. In this way the translational energy of a particle is decreased or increased from the thermal translational energy, providing an additional broadening effect to the thermal or Doppler broadening. This contribution is also described by a Lorentzian distribution and is known as quasistatic pressure broadening.

Elastic and inelastic collisions present extremes of collisional broadening, both described by Lorentzian distributions. Experimental measurements may often be subject to both, and spectral lines are broadened by a combination of lifetime, Doppler and pressure effects. Some of these broadening effects may be dominant under particular experimental conditions, for example at low pressures it is necessary only to consider Doppler effects. In this case the distribution is described by a convolution of Gaussian and Lorentzian profiles known as a Voigt profile. The area-normalised Voigt distribution centered at x_c with contributions from the Gaussian and Lorentzian FWHM, w_G and w_L respectively, is described by:

$$g(x-x_c) = \frac{(2\ln 2)}{\pi^{3/2}} \frac{w_L}{w_G^2} \int_{-\infty}^{\infty} \frac{\exp(-t^2)}{\left(\left(\sqrt{\ln 2}\left(\frac{w_L}{w_G}\right)\right)^2 + \left(\sqrt{4\ln 2}\left(\frac{(x-x_c)}{w_G}\right) - t\right)^2\right)} dt \qquad (1.15)$$

These line shapes are illustrated in Figure 1.8 where: $w_G = 1$ for the Gaussian profile (equation 1.13); $w_L = 1$ for the Lorentzian profile (equation 1.12); and the Voigt profile is a renormalised convolution of the Gaussian and Lorentzian.

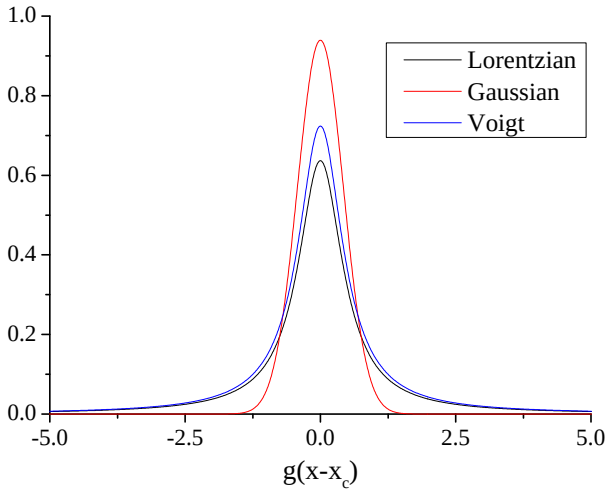

Figure 1.8: Illustration of the Gaussian, Lorentzian and Voigt profiles discussed in the text.

1.3 Nascent Line Profiles

The line shapes recorded for nascent photofragments are Doppler-broadened line profiles which can be described using Dixon's bipolar moment formalism where the correlated distribution of recoil velocity and rotational angular momentum are described in terms of bipolar moments.[53]

1.3.1 Bipolar Moments

Bipolar moments are reformatted values of the expectation values of bipolar harmonics, which themselves describe the relationship between the two spatial coordinate systems of the parent and the fragment.[53] Briefly, the three dimensional distribution of the parent's transition dipole moment, fragment's recoil velocity and fragment's total angular momentum is condensed down onto a one dimensional detection axis with the correlation between two or more vectors described by the bipolar moments. In Dixon's[53] treatment the bipolar moments are referenced to the parent's transition dipole moment, $\boldsymbol{\mu}$, known as the 'molecular frame'. Later treatments referenced the bipolar moments to the 'laboratory frame', wherein the z-axis contains the electric vector of the dissociating laser, ε_p as shown in Figure 1.9 using blue. The laboratory frame is the reference frame used in this work. For the probing radiation, the electric vector of the probe laser, ε_a, is designated the x-axis and the direction of propagation of the radiation is designated the z-axis, as shown in Figure 1.9 using red. The two cases of interest in this work: lasers counter-propagating with polarisations parallel and perpendicular are shown as Figure 1.9a and Figure 1.9b, respectively .[46,53]

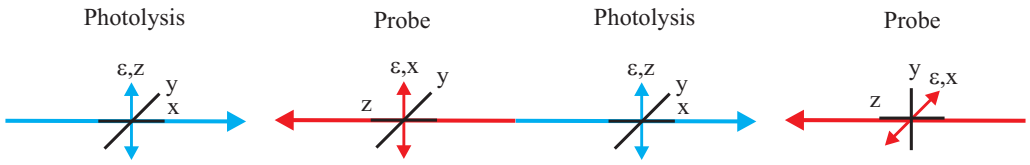

(a) Parallel electric vectors (b) Perpendicular electric vectors

Figure 1.9: The reference frames involved in linearly polarised pump-probe theory.

The bipolar moments each describe a vector correlation and are normalised to the

values given in Table 1.1. The $\mu - v$ correlation in the bipolar moment treatment is half the recoil anisotropy discussed above, $\beta = 2\beta_0^2(20)$.

Table 1.1: Bipolar moments, their range and the vector correlations they represent.

Bipolar Moment	Range	Vector Correlation
$\beta_0^2(02)$	$-\frac{1}{2} \leftrightarrow +1$	$\mu - J$
$\beta_0^2(20)$	$-\frac{1}{2} \leftrightarrow +1$	$\mu - v$
$\beta_0^0(22)$	$-\frac{1}{2} \leftrightarrow +1$	$v - J$
$\beta_0^2(22)$	$-1 \leftrightarrow +\frac{1}{2}$	$\mu - v - J$
$\beta_0^2(42)$	$-\frac{1}{2} \leftrightarrow +1$	$\frac{7}{12}\beta_0^2(02) - \frac{5}{12}\beta_0^2(22)$

1.3.2 Doppler Profiles

In order to describe the detected signal it is necessary to consider the Doppler shift from the centre of the line profile by convolving the line profile with a Gaussian. The line profile, $D(w)$, is described by equation 1.16, where v_0 is the maximum velocity and P_i are Legendre polynomials.[ii] The g_i terms contain the contribution of the bipolar moments to the line profile according to equation 1.17, where the pre-multipliers, the b_i terms given in Appendix A.3, depend upon the angle between the propagation of the two lasers; the angle between the two electric vectors of the lasers used and the type of absorption branch being probed, as given in Appendix A.[53]

$$D(w) = \frac{1}{2v_0}\left[g_0 + g_2 P_2\left(\frac{w}{v_0}\right) + g_4 P_4\left(\frac{w}{v_0}\right)\right] \tag{1.16}$$

$$\begin{aligned} g_0 &= 1 + b_1\beta_0^2(02) \\ g_2 &= b_2\beta_0^2(20) + b_3\beta_0^0(22) + b_4\beta_0^2(22) \\ g_4 &= 1 + b_5\beta_0^2(42) \end{aligned} \tag{1.17}$$

This description applies to linearly polarised radiation but has been adapted by Costen and Hall to account for polarisation properties arising for circularly polarised light, which were not considered in Dixon's formalism. In their treatment of Doppler profiles Costen and Hall normalised their parameters to give the same results as discussed above, allowing

[ii] $P_2(x) = \frac{1}{2}\left(3x^2 - 1\right)$ and $P_4(x) = \frac{1}{8}\left(35x^4 - 30x^2 + 3\right)$

the line shape described above to be used. However, the line profile resulting from circularly polarised photolysis and probe radiation was found to be described by equation 1.18 where the terms $h^{(1)}$, $h^{(2)}$ and $V(J)$ are again given in Appendix A.[46]

$$\begin{aligned} D(w) = 1 &+ 5\beta_0^2(20)P_2\left(\frac{w}{v_0}\right) \\ &+(-1)^{CP}\frac{3}{2}h^{(1)}\left[\beta_0^1(01) + 5\beta_0^1(21)P_2\left(\frac{w}{v_0}\right)\right] \\ &-h^{(2)}V(J)\left[\frac{1}{2}\beta_0^0(22)P_2\left(\frac{w}{v_0}\right) + \frac{1}{2}\beta_0^2(02)\right. \\ &\left. - \frac{5}{7}\beta_0^2(22)P_2\left(\frac{w}{v_0}\right) + \frac{9}{7}\beta_0^2(42)P_4\left(\frac{w}{v_0}\right)\right] \end{aligned} \tag{1.18}$$

From this equation, the only difference between the Doppler profiles of co- and counter-rotating geometries (see Figure 1.10) arises from CP, where $CP = 0$ for co-rotating and $CP = +1$ for counter-rotating.[46]

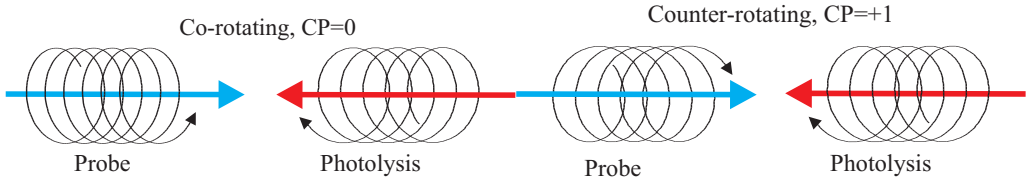

(a) Co-rotating (b) Counter rotating

Figure 1.10: The relative helicities of the pump and probe radiation as described by Costen and Hall.[46]

$D(w)$, suitably convoluted with a Gaussian, has been used to describe the experimental data recorded on the CN fragment in Chapter 5. In that chapter the two bipolar moments introduced by Costen and Hall to describe orientation are measured. These two bipolar moments, $\beta_0^1(01)$ and $\beta_0^1(21)$, refer to the orientation of the total angular momentum relative to the photolysis polarisation, used as the Z direction and illustrated in Figure 1.11. $\beta_0^1(01)$ is independent of the recoil direction and describes orientation of the angular moment parallel or antiparallel to the photolysis polarisation, (Figure 1.11a). $\beta_0^1(21)$ also describes orientation parallel or antiparallel to the recoil direction *if* the fragment is recoiling in the ±Z direction, but $\beta_0^1(21)$ is recoil dependent, thus for fragments recoiling

in the XY plane $\beta_0^1(21)$ will have the opposite sign to $\beta_0^1(01)$, (Figure 1.11b).

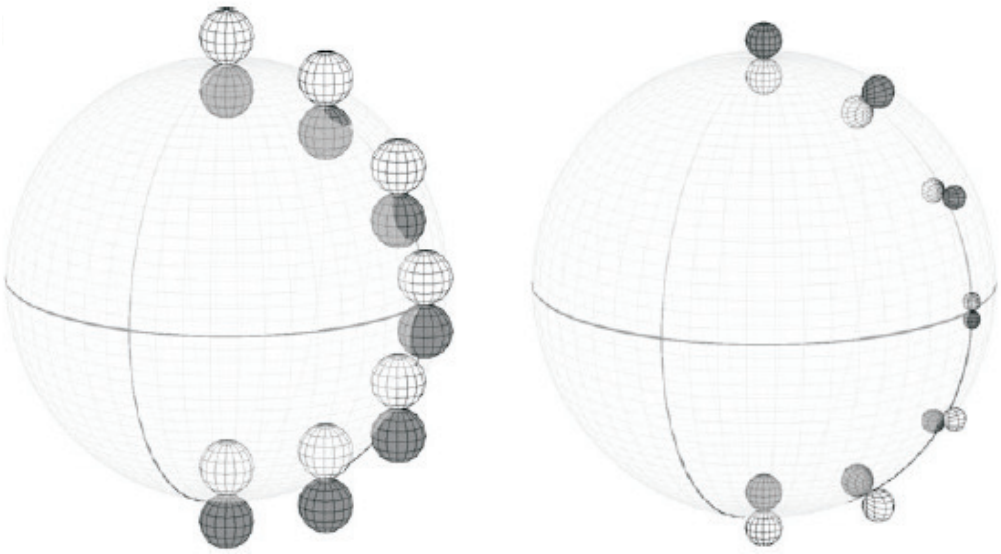

(a) $\beta_0^1(01)$ (b) $\beta_0^1(21)$

Figure 1.11: Illustration of the angular dependence of the two orientation bipolar moments, reproduced from Costen and Hall and discussed in the text. The sphere represents the recoil direction with the Z-axis defined as the polarisation of the photolysis laser. [46]

Determining bipolar moments in the manner described above relies upon a very high polarisation purity of the photolysis and probe radiation. Furthermore, the probe radiation must have a high level of frequency stability and tunability, in which respect diode lasers are an obvious candidate.

1.4 Diode Lasers

Throughout this thesis continuous-wave lasers have been used to probe the chemical species of interest. Diode lasers are one of the most important classes of continuous-wave lasers, delivering tunability and frequency stability due to their construction. Diode lasers are typically formed from III/V semiconductors such as GaAs where there is a direct band gap and, in order to function as a laser, these semiconductors must have a completely filled valence band and a completely empty conduction band. Pumping electrons from the valence band into the conduction band creates electron holes in the valence band, into which the conduction electrons drop, producing spontaneous emission. Large scale

pumping of electrons from the valence band into the conduction band generates a large number of pairs of electrons and electron holes, allowing spontaneous emission to induce electrons in the conduction band to combine with electron holes in the valence band, leading to stimulated emission and therefore laser action. In order to achieve this, pumping is either performed using another laser or by applying a large enough current to the semiconductor.[52]

The energy of the emitted photons will depend upon the band gap, this in turn depends upon the semiconductor material and the temperature of the semiconductor. Thus, different wavelength regions can be accessed by careful selection of the semiconductor material or by altering the temperature of the semiconductor. In addition to these factors, the applied current varies the energy gap between the top of the conduction band and the top of the valence band since increasing the current depletes the valence band and populates the conduction band, Figure 1.12. Therefore, diode lasers can be frequency tuned by varying the applied current or the temperature, but to scan the frequency of a diode laser the current is generally used.[52]

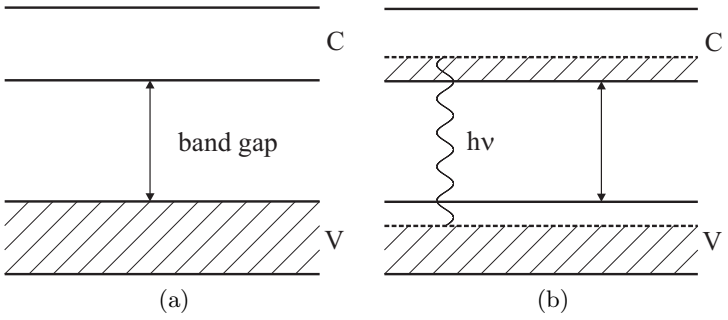

Figure 1.12: Illustration of (a) the semiconductor band gap between the conduction band, C, and the valence band, V, and (b) the energy gap when a current is applied.[52]

Tunable external-cavity diode lasers (ECDLs) are excellent spectroscopic tools. In these lasers the laser diode is arranged in an optical cavity with a diffraction grating to provide wavelength selection, either by tuning the angle of the grating relative to the laser diode or by tuning the length of the cavity. The two common configurations are the Littrow and Littman-Metcalf, shown in Figure 1.13.

The Littrow configuration involves tuning the grating by means of a piezoelectric

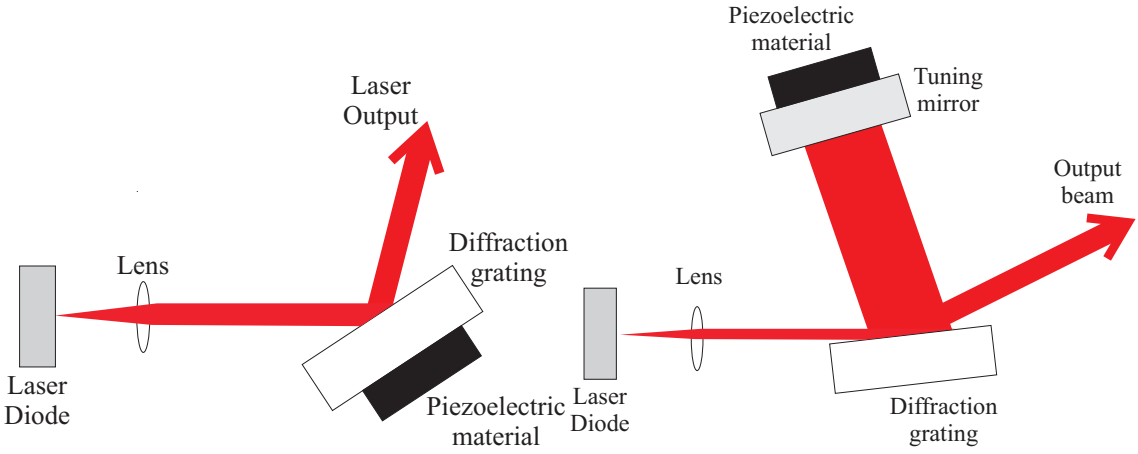

(a) Littrow configuration (b) Littman-Metcalf configuration

Figure 1.13: The two cavity arrangements used in the ECDLs in this work

material with the first-order diffraction providing optical feedback to the diode. The Littman-Metcalf configuration fixes the grating with a movable mirror, again controlled by a piezoelectric transducer, reflecting the first-order reflection back to the laser diode. The beam displacement inherent in the Littrow configuration due to the movable grating is inconvenient, particularly as ECDLs are often tuned over spectroscopic transitions by means of the grating. However, the loss of the zeroth-order diffraction in the Littman-Metcalf configuration results in lower power output than the Littrow, while the fixed grating does avoid beam displacement.[54,55]

Throughout this work diode lasers have been used to probe the chemical species of interest. In Chapter 2 a diode laser arranged without a cavity has been used but all other measurements have utilised one of the two types of ECDL.

1.5 Thesis Overview

This chapter has introduced the interest in studying photodissociation dynamics through scalar and vector properties and the favourable properties of diode lasers. In the next chapter we utilise diode laser gain *versus* absorption spectroscopy to probe the quantum yield of I^* formation following 248 nm and 266 nm photolysis of iodobenzene and its fluorinated analogues.

Chapter 3 and Chapter 4 detail the development of a tunable continuous-wave ultra-

violet radiation source. This source allows the narrow bandwidth of near-infrared diode lasers to be extended to electronic spectroscopy of formaldehyde and the OH radical.

Finally, Chapter 5 presents the study of the UV photolysis of ICN through frequency modulation studies of the CN fragments. Orientation and alignment bipolar moments are determined for a number of high rotational states in the ground and first excited vibrational levels.

References

[1] R. Schinke, *Photodissociation Dynamics: Spectroscopy and Fragmentation of Small Polyatomic Molecules*, Cambridge Monographs on Atomic, Molecular and Chemical Physics, Cambridge University Press, 1995.

[2] C. B. Moore and J. C. Weisshaar, Annual Review of Physical Chemistry **34**, 525 (1983).

[3] H. M. Yin, S. H. Kable, X. Zhang, and J. M. Bowman, Science (New York, N.Y.) **311**, 1443 (2006).

[4] W. Fisher, Chemical Physics **89**, 457 (1984).

[5] M. A. OHalloran, H. Joswig, and R. N. Zare, The Journal of Chemical Physics **87**, 303 (1987).

[6] Y. Amatatsu, S. Yabushita, and K. Morokuma, The Journal of Chemical Physics **100**, 4894 (1994).

[7] R. D. van Zee, M. F. Foltz, and C. B. Moore, The Journal of Chemical Physics **99**, 1664 (1993).

[8] D. Townsend et al., Science (New York, N.Y.) **306**, 1158 (2004).

[9] P. Andresen, G. S. Ondrey, B. Titze, and E. W. Rothe, The Journal of Chemical Physics **80**, 2548 (1984).

[10] T. Carrington, The Journal of Chemical Physics **41**, 2012 (1964).

[11] V. Staemmler and A. Palma, Chemical Physics **93**, 63 (1985).

[12] G. Theodorakopoulos, I. D. Petsalakis, and R. J. Buenker, Chemical Physics **96**, 217 (1985).

[13] A. J. Orr-Ewing and R. N. Zare, Annual Review of Physical Chemistry **45**, 315 (1994).

[14] R. Zare and D. Herschbach, Proceedings of the IEEE **51**, 173 (1963).

[15] C. Jonah, The Journal of Chemical Physics **55**, 1915 (1971).

[16] G. E. Busch, The Journal of Chemical Physics **56**, 3626 (1972).

[17] S.-C. Yang, The Journal of Chemical Physics **61**, 4400 (1974).

[18] T. P. Rakitzis, Science **281**, 1346 (1998).

[19] L. J. Butler and D. M. Neumark, The Journal of Physical Chemistry **100**, 12801 (1996).

[20] M. N. R. Ashfold et al., Physical chemistry chemical physics : PCCP **12**, 1218 (2010).

[21] A. G. Sage et al., Physical chemistry chemical physics : PCCP (2011).

[22] D. Murdock, M. B. Crow, G. A. D. Ritchie, and M. N. R. Ashfold, The Journal of Chemical Physics **136**, 124313 (2012).

[23] N. R. Ashfold, J. E. Baggott, and R. S. of Chemistry (Great Britain), *Molecular photodissociation dynamics*, Advances in gas-phase photochemistry and kinetics, Royal Society of Chemistry, 1987.

[24] M. N. R. Ashfold and J. D. Howe, Annual Review of Physical Chemistry **45**, 57 (1994).

[25] D. W. Chandler and P. L. Houston, The Journal of Chemical Physics **87**, 1445 (1987).

[26] A. T. J. B. Eppink and D. H. Parker, Review of Scientific Instruments **68**, 3477 (1997).

[27] M. N. R. Ashfold et al., Physical chemistry chemical physics : PCCP **8**, 26 (2006).

[28] I. Nadler, D. Mahgerefteh, H. Reisler, and C. Wittig, The Journal of Chemical Physics **82**, 3885 (1985).

[29] P. Brewer, P. Das, G. S. Ondrey, and R. Bersohn, The Journal of Chemical Physics **79**, 720 (1983).

[30] K. Kavita and P. K. Das, The Journal of Chemical Physics **117**, 2038 (2002).

[31] G. E. Hall and P. L. Houston, Annual Review of Physical Chemistry **40**, 375 (1989).

[32] J. Kos, M. H. Alexander, M. Brouard, C. J. Eyles, and F. J. Aoiz, The Journal of chemical physics **129**, 054301 (2008).

[33] Y.-P. Chang, M. Brouard, R. Cireasa, T. Perkins, and S. A. Seamons, Physical chemistry chemical physics : PCCP **13**, 8213 (2011).

[34] M. Brouard et al., Molecular Physics **103**, 1693 (2005).

[35] M. Brouard, H. Chadwick, Y.-P. Chang, R. Cireasa, and C. J. Eyles, Physica Scripta **80**, 048120 (2009).

[36] M. L. Costen et al., The journal of physical chemistry. A **113**, 15156 (2009).

[37] G. Paterson, M. L. Costen, and K. G. McKendrick, International Reviews in Physical Chemistry **31**, 69 (2012).

[38] H. Petek, D. J. Nesbitt, D. C. Darwin, and C. B. Moore, The Journal of Chemical Physics **86**, 1172 (1987).

[39] J. I. Cline, C. A. Taatjes, and S. R. Leone, The Journal of Chemical Physics **93**, 6543 (1990).

[40] T. Suzuki, H. Kanamori, and E. Hirota, The Journal of Chemical Physics **94**, 6607 (1991).

[41] G. E. Hall and M. Wu, The Journal of Physical Chemistry **97**, 10911 (1993).

[42] M. L. Costen, S. W. North, and G. E. Hall, The Journal of Chemical Physics **111**, 6735 (1999).

[43] G. E. Hall and S. W. North, Annual review of physical chemistry **51**, 243 (2000).

[44] M. L. Costen and G. E. Hall, Physical Chemistry Chemical Physics **7**, 1408 (2005).

[45] A. Alagappan, M. L. Costen, and K. G. McKendrick, Spectrochimica acta. Part A, Molecular and biomolecular spectroscopy **63**, 910 (2006).

[46] M. L. Costen and G. E. Hall, Physical chemistry chemical physics : PCCP **9**, 272 (2007).

[47] A. Alagappan, I. Ballingall, M. L. Costen, K. G. McKendrick, and G. Paterson, Physical chemistry chemical physics : PCCP **9**, 747 (2007).

[48] A. Alagappan, I. Ballingall, M. L. Costen, and K. G. McKendrick, The Journal of chemical physics **126**, 041103 (2007).

[49] I. Ballingall, M. F. Rutherford, K. G. McKendrick, and M. L. Costen, Molecular Physics **108**, 847 (2010).

[50] S. J. McGurk et al., The Journal of chemical physics **136**, 164306 (2012).

[51] W. Demtröder, *Laser spectroscopy: basic concepts and instrumentation*, Number v. 2 in Springer series in chemical physics ; v. 5, Springer, 1996.

[52] O. Svelto and D. C. Hanna, *Principles of Lasers*, Plenum Press, 1998.

[53] R. N. Dixon, The Journal of Chemical Physics **85**, 1866 (1986).

[54] M. G. Littman and H. J. Metcalf, Applied optics **17**, 2224 (1978).

[55] K. Liu and M. G. Littman, Optics letters **6**, 117 (1981).

Chapter 2

The UV Photodissociation of Aryl Iodides: I^* Quantum Yields

A key measurement in photodissociation dynamics, especially for large polyatomic systems, is the determination of both reaction channels and their selective quantum yields. Answers to this question clearly give insight into the pathways that lead to bond fission. In particular, the work presented here focuses upon the aryl iodides and we present quantum yields for forming electronically excited iodine atoms as part of a wider-ranging study conducted in collaboration with the research group of Mike Ashfold in Bristol. The quantum yield of electronically excited iodine following photolysis of iodobenzene has been measured using time-resolved near-infrared diode laser gain *vs.* absorption, and the effect of fluorination on the quantum yield has been investigated. Selective fluorination has been used to lower the symmetry of the iodobenzene, in addition to influencing the excited-state potential energy surfaces involved in the dissociation. While fluorination of these aryl iodides results in only minor differences in the quantum yield, complementary studies of the recoil direction and vibrational energy partitioning performed using velocity map ion imaging (VMI) find that fluorination alters the dynamics.[1,2]

2.1 Introduction

Photodissociation studies seek to understand the nature of the bond breaking process. Initial studies focused on simple atomic photofragments, particularly the translational energy released into hydrogen atoms.[3] Since hydrogen can only use the energy available to it for

translation (assuming it is formed in its electronic ground state), the interpretation of the translational kinetic energy release (TKER) is simplified relative to molecular fragments. Recent studies have investigated the importance of $n \rightarrow \sigma^*$ and $\pi \rightarrow \sigma^*$ transitions in HX molecules, such as X=OH, CH_3O, C_6H_5O, C_6D_5O and C_6H_5S;[4–11] as well as in heteroaromatics such as pyrrole, indole and imidazole;[12–17] in these molecules the σ^* orbital may be populated directly by absorption, or indirectly by transfer from another surface.[3] These pathways reveal details about the excited-state potential energy surfaces such as their associative or dissociative nature or conical intersections between them. Therefore, photofragment translation spectroscopy is now being applied to halide fragments to develop the understanding of these molecules, in which, unlike H atoms, the partitioning of energy into electronic excitation of the halide atom provides additional surfaces.[1–3,18] For example, photodissociation of CH_3I has been extensively studied, both theoretically[19–28] and experimentally[25–34] with initial studies aiming to extend the understanding of photodissociation dynamics beyond simple diatomics.[33] However, CH_3I photodissociation was also the prototype system for velocity map ion imaging (VMI).[29] As discussed in Chapter 1, VMI is regularly used to probe photodissociation and collision dynamics due to its ability to determine quantum-state-resolved energy distributions, angular distributions and vector correlations.[35] The large amount of past success in applying VMI to CH_3I photolysis and considerable interest in understanding the complex dynamics of aromatic compounds have inspired the Ashfold group to study C_6H_5I and investigate the effects of fluorination on the photodissociation dynamics using PTS and VMI. To illustrate the complexity of these systems the excited-state PESs are shown in Figure 2.1 for iodobenzene.

The orbital configuration of atomic iodine is $[\mathrm{Kr}]4d^{10}5s^25p^5$, with a total orbital angular momentum quantum number of $L = 1$ and total spin angular momentum quantum number of $S = 1/2$, giving rise to a ^2P ground state. Spin orbit coupling gives rise to levels with total angular momentum quantum numbers of $J = L + S, |L + S - 1|, \ldots |L - S|$, and the resulting $^2P_{3/2}$ ground state and $^2P_{1/2}$ excited-state, hereafter denoted as I and I* respectively, are separated by $7603\,\mathrm{cm}^{-1}$.

Initial investigation of the wavelength dependence of the TKER of the ground and excited state iodine products by Sage *et al.*[1] showed a number of possible channels in the TKER spectrum and a near limiting β for both I and I* products at most wavelengths.

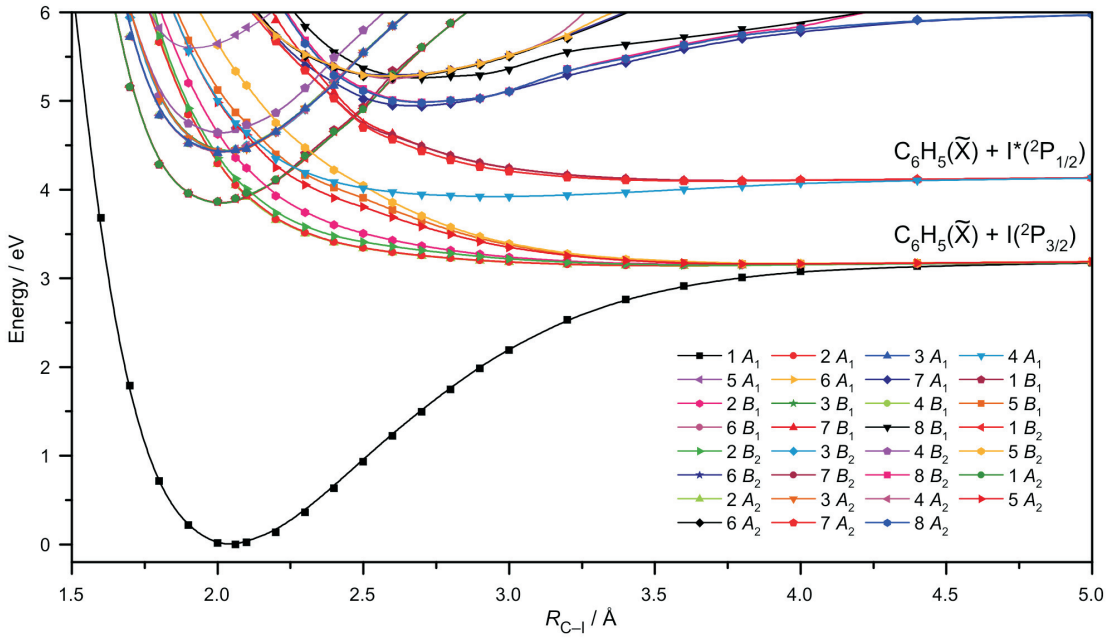

Figure 2.1: C_6H_5I ground and excited-state potential energy curves, reproduced from Sage *et al.*[1]

Example velocity map images and TKER distributions are shown in Figure 2.2 for the I* fragment following 266 nm photolysis. The positive β helped to determine which states were accessed during the photodissociation, excluding states of the wrong symmetry from the analysis. The relative I and I* populations would indicate the initial transition probabilities and the extent of coupling between excited-states; unfortunately, VMI can not observe both the I and I* products simultaneously since the REMPI schemes required to detect each fragment access different intermediate states and occur at significantly different wavelengths. It is therefore difficult to accurately measure the relative amounts of I and I* using this technique. Thus, independent measurement of the quantum yield was required. In addition to this, there is some dispute about the values for the quantum yield of I* formation in the literature, with Pence *et al.* reporting 0.25 ± 0.01 at 248 nm and < 0.004 at 308 nm, whereas Kavita and Das report 0.59 ± 0.01, 0.51 ± 0.01 and 0.24 ± 0.01 at 236 nm, 266 nm and 305 nm, respectively.[36,37] The factor of two difference between these yields is especially odd since both studies report comparable I* quantum yields for CH_3I photolysis, where Pence *et al.* found 0.81 ± 0.03 at 248 nm and Kavita and Das

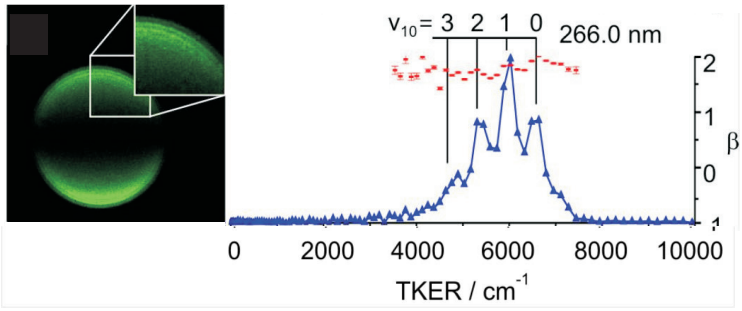

Figure 2.2: An example VMI data set and corresponding translational kinetic energy release (TKER) of I* following 266 nm photolysis of C_6H_5I, reproduced from Figure 5 of Sage *et al.*[1] The left panel shows the ion image, the electric vector of the laser is vertical in the plane of the image/detector. The right panel shows the vibrational fine structure seen in the TKER with the red dots corresponding to the recoil anisotropy parameter β.

found 0.69 ± 0.03 at 236 nm and 0.75 ± 0.03 at 266 nm.

The dispute over the relative yield of I and I* is the focus of this chapter, and the method used to determine the quantum yield is based upon the pioneering work of Hess *et al.*,[38] in which a diode laser resonant with the electronic excitation energy of iodine ($7603\,\mathrm{cm}^{-1}$) was used to measure a gain in laser signal produced by the electronically excited iodine at early times (if the quantum yield is high enough), which was then related to an absorption signal at late times. Once this gain *vs* absorption technique has been demonstrated to successfully reproduce literature values of the I* quantum yield from photolysis of iodomethane at 248 nm and 266 nm, it will be used to evaluate the I* quantum yield for iodobenzene. This I* quantum yield then allows the complementary VMI studies to be interpreted using high level, spin-orbit-resolved *ab initio* calculations. These calculations indicate that photolysis is dominated by excitation to the $2A_1$ surface to give I and excitation to the $4A_1$ surface to give predominantly I*, with some curve crossing to produce I. An extensive discussion of the dynamics of iodobenzene photodissociation is contained in Sage *et al*[1] along with a comparison of the photolysis of HI and CH_3I, which is beyond the scope of this thesis. However, that work inspired further study of aryl iodides, reported by Murdock *et al.*[2]. In the aryl halides, the symmetry of iodobenzene is reduced through fluorination, in addition to using selective fluorination to alter the molecular energy levels. By measuring the dynamics of 2,4-difluorophenyliodide (2,4-dFPhI) the effect of lowering the symmetry from C_{2v} to C_s was investigated. The effect of selective fluorination

was explored using 4-fluorophenyliodide (4-FPhI), 3,5-difluorophenyliodide (3,5-dFPhI), 2,4-difluorophenyliodide (2,4-dFPhI) and pentafluorophenyliodide (C_6F_5I). The PESs for these compounds are illustrated in Figure 2.3 to allow comparison between the four fluorinated aryl iodides. These potential energy cuts were calculated using the MOLPRO computational package,[?] using Møller-Plesset second order perturbation theory (MP2) and complete active space self-consistent field (CASSCF) methods. The potential energy cuts were taken along the C-I coordinate with all other nuclear degrees of freedom fixed at their ground state MP2 equilibrium values.[2] I* quantum yields for these four fluorinated

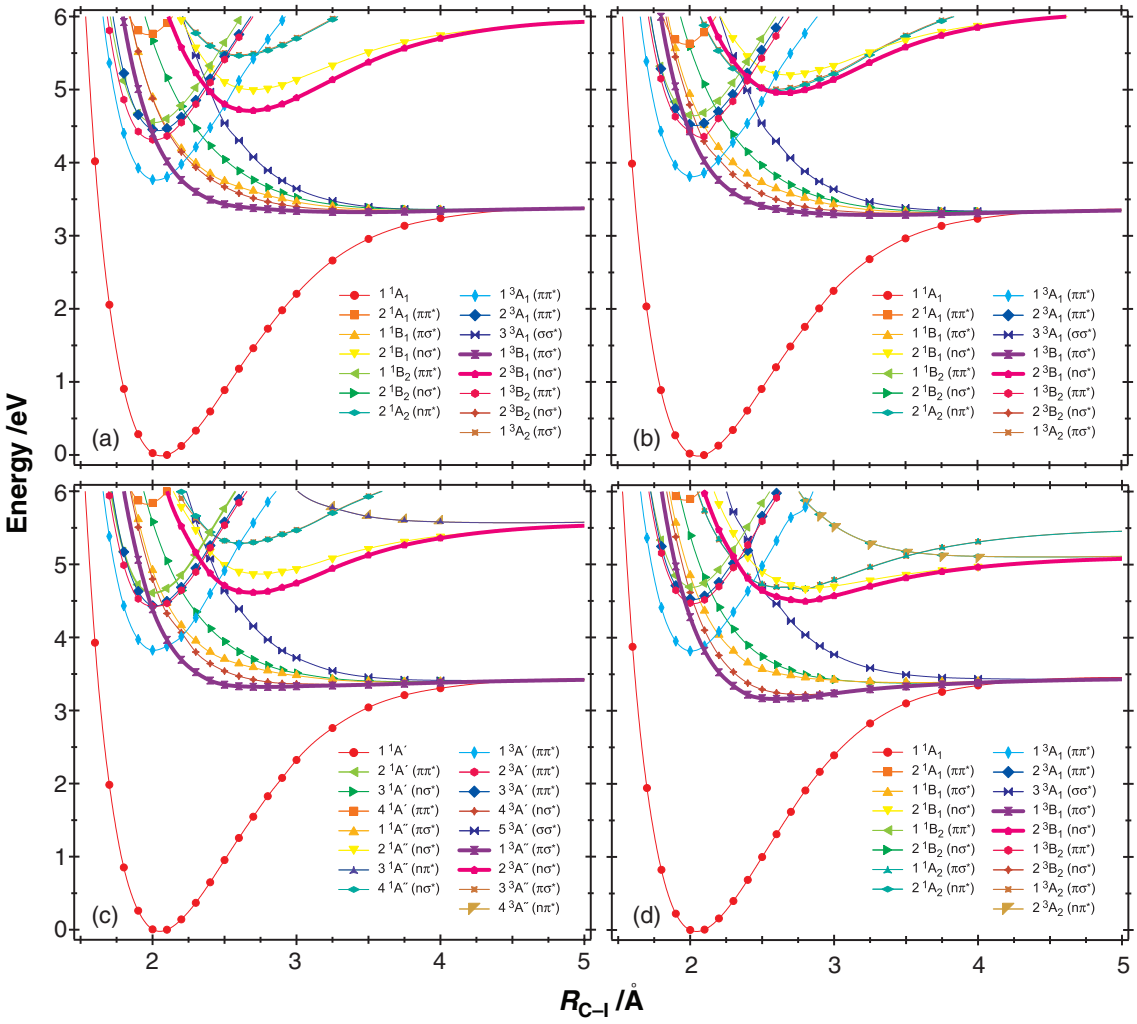

Figure 2.3: Ground and excited-state potential energy cuts along the C-I coordinate for (a) 4-fluorophenyliodide, (b) 3,5-difluorophenyliodide, (c) 2,4-difluorophenyliodide and (d) pentafluorophenyliodide, calculated with all other nuclear degrees of freedom fixed at the group state MP2 equilibrium values. Reproduced from Murdock *et al.*[2]

aryl iodides are required in order to interpret the VMI results in terms of the PESs accessed during the dissociation process. The I* quantum yield for pentafluorophenyliodide has been reported in the literature. However, there is some dispute about the accuracy of this value since it is reported by Kavita and Das, along with the iodobenzene quantum yield which is twice the previous measurements, as discussed above.[37] Therefore, the gain *vs* absorption technique will also be used to measure the I* quantum yields for all four fluorinated iodo-compounds following photolysis at 248 nm and 266 nm.

2.2 Iodine Atom Spectroscopy

The iodine nucleus is a fermion with nuclear spin quantum number of $I = 5/2$, which couples to the total electronic angular momentum to give levels with total angular momentum quantum number of $F = I + J, |I + J - 1|, \ldots |I - J|$; these are the hyperfine states in the atom. These energy levels are shown in Figure 2.4 with the spectroscopic transitions between them illustrated.

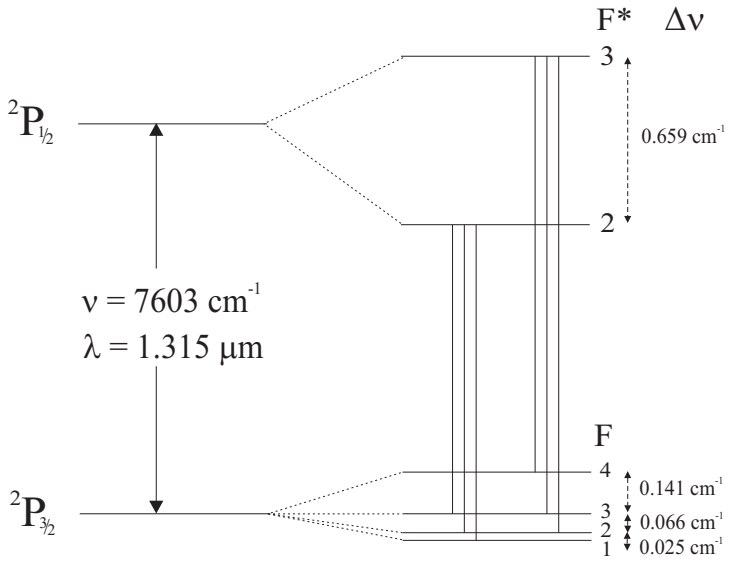

Figure 2.4: Iodine atom energy levels and hyperfine splitting.

Electric dipole transitions between the $^2P_{3/2}$ and $^2P_{1/2}$ levels are $\Delta l = 0$ transitions and therefore formally forbidden. However, the weaker magnetic dipole and electric quadrupole transitions are allowed, and it is magnetic dipole transitions that have been used in this

work. The selection rules governing these transitions are $\Delta F = 0, \pm 1$ but $0 \not\leftrightarrow 0$, and these transitions are shown in Figure 2.4. In particular, the $F^* = 3 \leftarrow F = 4$ hyperfine transition, which occurs at $7603.1379\,\mathrm{cm}^{-1}$, has been used for this work because it is the most isolated and strongest transition, $\sigma_{peak} = 5.86 \times 10^{-19}\,\mathrm{cm}^2\mathrm{molecule}^{-1}$.[39]

Laser absorption spectroscopy is most frequently conducted for a transition terminating in an excited-state with no population prior to the transition. Nascent iodine atoms produced from photolysis may however have population in the $^2P_{1/2}$ level, thus the $F^* = 3$ level may have population and must be considered. Since the laser is resonant with the absorption it is also resonant with the emission; therefore, any I* will cause stimulated emission. This manifests itself as a gain in the number of photons detected at the earliest time after photolysis, with the laser depleting the excited-state population over time. It is therefore possible to determine the I* quantum yield following photolysis by comparing the gain immediately following photolysis to the absorption once all the I* has been quenched to ground state iodine, i.e the gain at time $t = 0$ versus the absorption at time $t = \infty$.

2.3 Laser Gain *vs* Absorption

The quantum yield of I*, $\Phi(I^*)$, can be related to the initial concentrations of I and I*, donated $[I]_0$ and $[I^*]_0$, respectively, by:

$$\Phi(I^*) = \frac{[I^*]_0}{[I^*]_0 + [I]_0}. \tag{2.1}$$

For an individual hyperfine transition, the ratio of the initial to final signal amplitude, S_i/S_F, depends upon the populations of ground and excited-state hyperfine levels, $N(^2P_{3/2})$ and $N(^2P_{1/2})$ respectively, in addition to the absorption cross section, σ_{F^*-F}, and emission cross section, σ_{F-F^*}, according to:[38]

$$\frac{S_i}{S_f} = \frac{\left(\frac{2F^*+1}{\sum_{F^*}(2F^*+1)}\right)\sigma_{F^*-F}N(^2P_{1/2}) - \left(\frac{2F+1}{\sum_{F}(2F+1)}\right)\sigma_{F-F^*}N(^2P_{3/2})}{\left(\frac{2F+1}{\sum_{F}(2F+1)}\right)\sigma_{F-F^*}[N(^2P_{1/2}) + N(^2P_{1/2})]}, \tag{2.2}$$

where the cross sections depend upon the Einstein A factor, A_{F^*-F}, and the line shape,

$f(\nu)$, according to:

$$\begin{aligned} \sigma_{F^*-F} &= A_{F^*-F}\frac{\lambda}{8\pi}f(\nu) \\ \sigma_{F-F^*} &= \left(\frac{2F^*+1}{2F+1}\right)\sigma_{F^*-F}. \end{aligned} \tag{2.3}$$

Substituting equations 2.2 and 2.3 into equation 2.1 gives:

$$\Phi(I^*) = \frac{1}{3}\left(\frac{S_i}{S_f}+1\right), \tag{2.4}$$

in which the experimentally determined initial and final signals are related to the quantum yield.

A diode laser gain versus absorption profile is shown in Figure 2.5, with the gain, S_i, and absorption, S_f, indicated. From equation 2.4 and Figure 2.5 it is apparent that any *positive* gain signal at t=0 ($S_i > 0$ in Figure 2.5) corresponds to $\Phi(I^*) > 1/3$.

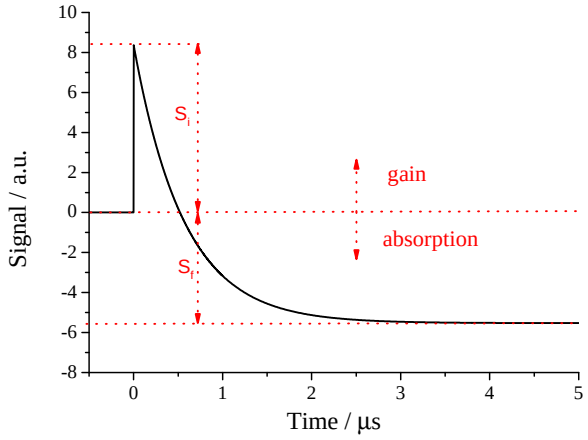

Figure 2.5: Example gain *vs* absorption signal illustrating gain, absorption, S_i and S_f.

In order to ensure that there is no contribution to the measurements from the recoil anisotropy, i.e. to ensure that the line shape, $f(v)$, is the same for I and I*, argon is added to translationally relax both and I and I*. In addition to this, the technique relies upon all of the I* products being converted into I at later time and, to ensure this, molecular oxygen is added. Molecular oxygen is an efficient quencher of I* due to a near resonant

transition,

$$O_2(^3\Sigma_g^-) + I^*(^2P_{1/2}) \rightarrow O_2(^1\Delta_g) + I(^2P_{3/2}), \tag{2.5}$$

with a quenching rate constant $k_{O_2} = 3 \times 10^{-11}\,\mathrm{cm^3 molecule^{-1} s^{-1}}$.[38] This quenching rate constant is much larger than the rate constants for any of the other decay processes available:[40,41]

$$Ar + I^* \rightarrow Ar + I \quad k = 8 \times 10^{-15}\,\mathrm{cm^3 molecule^{-1} s^{-1}} \tag{2.6}$$

$$CH_3I + I^* \rightarrow CH_3I + I \quad k = 2.8 \times 10^{-13}\,\mathrm{cm^3 molecule^{-1} s^{-1}}. \tag{2.7}$$

2.4 Experimental

The experimental setup used to measure the I^* quantum yield is summarised in Figure 2.6. A distributed feedback (DFB) InGaAsP diode laser (Mitsubishi ML776H11F) is locked to a fixed Fabry-Perot etalon (the locking spectrum analyser) *via* a feedback circuit; this feedback circuit stabilises the diode laser's lasing frequency and allows the diode laser to be scanned by scanning the etalon. The laser is current and temperature tuned to be resonant with the $I^*(F^* = 3) \leftarrow I(F = 4)$ transition with the feedback circuit providing long term wavelength stability. The DFB radiation propagates through a 1.5 m long reaction cell and first passes through a 1315 nm filter (Thorlabs) with a bandwidth of 2 nm before being focussed onto a photoreceiver (Thorlabs PDA255). Two sources of photolysis light were used: a KrF excimer laser (Lamda Physik COMPex 205) to generate 248 nm and the frequency quadrupled output of a Nd:YAG (Continuum Powerlight 9020) to generate 266 nm. In both cases the photolysis beam co-propagates through the reaction cell with the probe beam. The scattered radiation from the first mirror is monitored by a detector and used as the trigger for the experiment's timescale.

As discussed earlier, measurements were made on flowing gas samples consisting of the relevant iodo-compound in addition to the two quenching species, O_2 and Ar. In order to account for experimental artifacts, such as scattered radiation or thermal lensing, a background signal was recorded off resonance with the transition and subtracted from the resonant signal. Diffusion of I and I* out of the probe beam diminish the absorption signal over time. This effect was observed as a decrease in absorption at times $t > 50\,\mu s$ and does

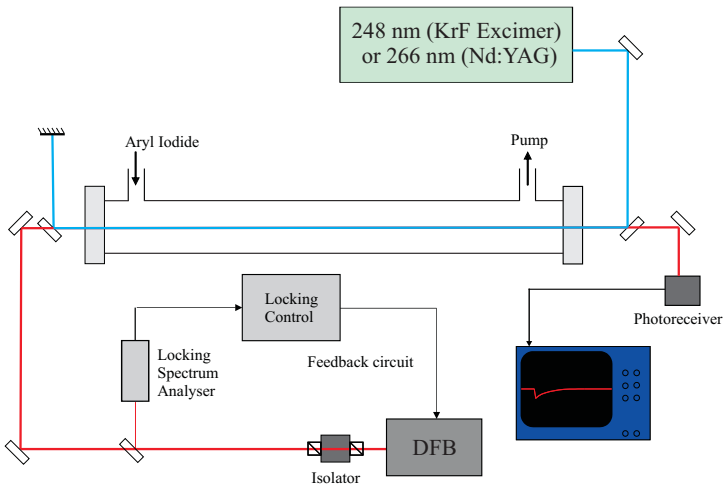

Figure 2.6: Experimental setup used to record laser gain *vs* absorption signals.

not affect these measurements due to the relatively short timescale of the experiment.

2.5 Results

2.5.1 Iodomethane

Initially, the experimental method was confirmed using iodomethane, for which there are several measurements of the quantum yield.[36,37,42] An example laser gain *vs* absorption profile for iodomethane following 248 nm photolysis is shown in Figure 2.7 and the measured quantum yield $\Phi(I^*, 248\,\text{nm}) = 0.71 \pm 0.04$, was in fair agreement with literature results of 0.81 ± 0.03 using laser gain *vs* absorption[36] and 0.71 ± 0.02 using mass spectrometry,[42] both at this photolysis wavelength.

Photolysis of CH_3I at 266 nm produced a quantum yield of $\Phi(I^*, 266\,\text{nm}) = 0.71 \pm 0.05$, again in good agreement with literature values of 0.73 ± 0.04 using the laser gain *vs* absorption technique[38] and 0.75 ± 0.03 using two photon LIF (TPLIF).[37] Recently there has been some dispute in the literature regarding the iodomethane quantum yield following 193 nm photolysis.[43] This has been suggested to be the result of photolysis of I_2 formed by recombination following photolysis, with supporting evidence being drawn from a time and pressure dependent quantum yield.[44] This effect does not contribute to this work since I_2 absorbs very strongly below 200 nm but very weakly between 200 nm and 300 nm, the

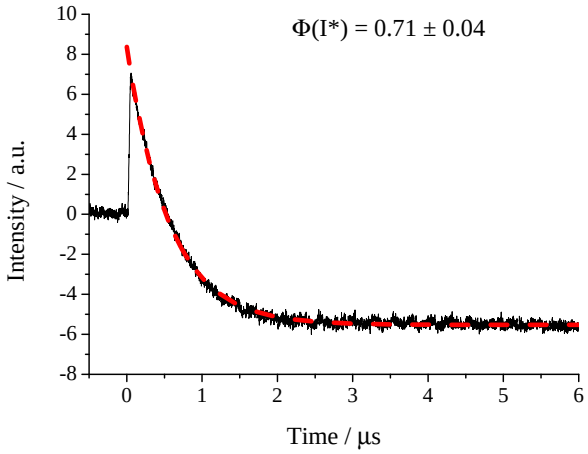

Figure 2.7: Example iodomethane gain *vs* absorption signal from 248 nm photolysis, taken with 2 Torr of CH_3I, 2 Torr of O_2 and 40 Torr of Ar. The fitted exponential decay is shown as a dashed line.

region these studies focus on. The agreement of the measured $\Phi(I^*)$ with the literature values for CH_3I gives confidence in this experimental method, therefore allowing it to be applied to the aryl iodides of interest.

2.5.2 Iodobenzene

The laser gain *vs* absorption profiles for iodobenzene following photolysis at 248 nm and 266 nm are shown in Figure 2.8. There is noticeably less gain at both wavelengths than for iodomethane, indicating a much lower value of $\Phi(I^*)$. The quantum yields for iodobenzene and pentafluoroiodobenzene have been reported in the literature; however, as discussed above in section 2.1, recent literature values are twice that of previous values, with Pence *et al.*[36] reporting $\Phi(I^*, C_6H_5I) = 0.25$ using gain *vs* absorption, whereas Kavita and Das[37] report values of $\Phi(I^*, C_6H_5I, 236\,\text{nm}) = 0.59$ and $\Phi(I^*, C_6H_5I, 266\,\text{nm}) = 0.51$ using TPLIF. It is worth noting that a quantum yield of $\Phi(I^*) > \frac{1}{3}$ would be apparent as gain at time $t = 0$ according to equation 2.4, therefore the values of Kavita and Das would exhibit significant gain, which is not seen in these experiments and is illustrated in Figure 2.9 for their value of $\Phi(I^*, C_6H_5I, 266\,\text{nm}) = 0.51$. The measured values are in much better agreement with the previous value of Pence *et al.*.[36]

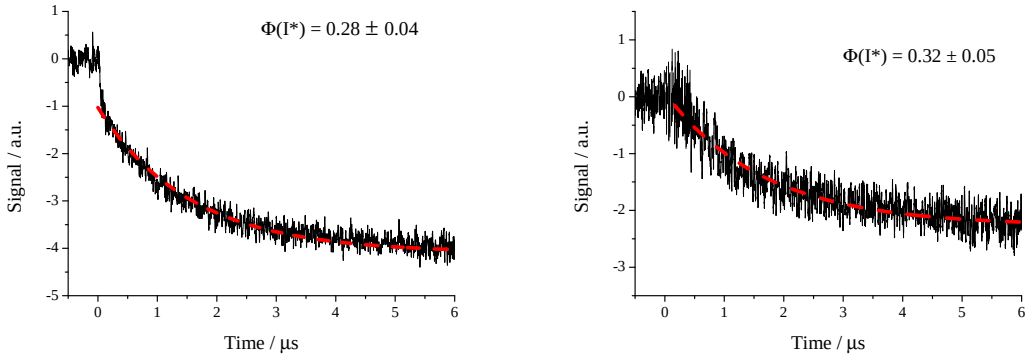

(a) 248 nm (b) 266 nm

Figure 2.8: An example gain *vs* absorption signal following (a) 248 nm and (b) 266 nm photolysis of C_6H_5I with the fitted exponential decay shown as a dashed line. These data were taken with 1 Torr of C_6H_5I, 1.5 Torr of O_2 and 40 Torr of Ar.

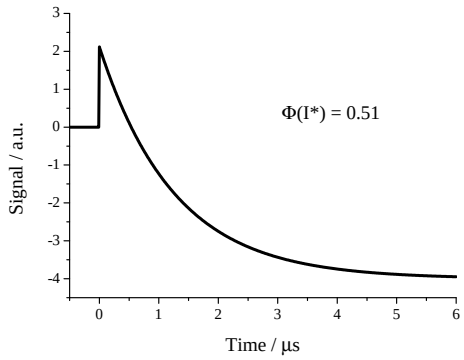

Figure 2.9: An illustration of the gain *vs* absorption signal for $\Phi(I^*) = 0.51$.

Since the values measured using the gain *vs* absorption technique did not show gain and were not found to deviate significantly with the pressure of either buffer gas or between a static or flowing sample, it can be assumed that there is some significant error in the TPLIF method used by Kavita and Das. Their method measures the vacuum ultraviolet emission spectrum from I and I* following two photon absorption of ultraviolet radiation (ca. 305 nm), and infrared emission to the fluorescent states ($^2P_{1/2}$ and $^2P_{3/2}$), shown in Figure 2.10. The quantum yield is determined by taking the ratio of the I* fluorescence, $S(I^*)$, to the I fluorescence, $S(I)$ as in equation 2.8.[45]

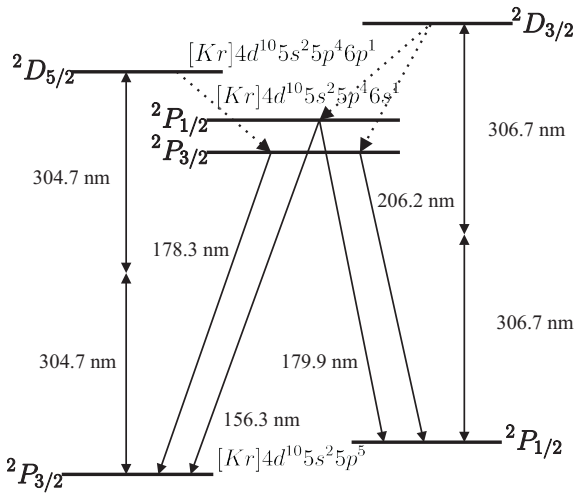

Figure 2.10: TPLIF scheme used by Kavita and Das to determine $\Phi(I^*)$.[45]

$$\frac{S(I^*)}{S(I)} = k\frac{[I^*]}{[I]} \tag{2.8}$$

The TPLIF experiment requires standardisation to determine the experimental constant k in equation 2.8, for which Kavita and Das used their experimentally determined value of $\Phi(I^*, CH_3I, 266\,nm) = 0.75 \pm 0.03$, returning $k = 1$. This quantum yield is in good agreement with other literature values (0.73 ± 0.04,[38] 0.73[33] and 0.76[46]) and so the discrepancies between the TPLIF values and the laser gain *vs* absorption values are unlikely to be due to standardisation. Unfortunately, Kavita and Das do not present emission spectra or unprocessed values for the recorded signals in their work. It is therefore difficult to determine if there are experimental artifacts introduced for some of these molecules or if an error has occurred in the data analysis. The experimental signal intensities, $S(I)$ and $S(I^*)$, used in the TPLIF measurements are ambiguous, it is not stated if these signals refer to integrated areas of the signal or maximum signal intensities. Integrated signals raise questions about the quantum efficiency of the PMT, which varies with wavelength, whereas maximum signal intensities do not account for the nascent line shapes. The absorption cross sections of iodomethane and iodobenzene at 266 nm are comparable ($\approx 1 \times 10^{-18}\,cm^2molecule^{-1}$ and $\approx 2 \times 10^{-18}\,cm^2molecule^{-1}$, respectively) which should allow many of the experimental features to be constant between compounds. However, these molecules display complex spectral features below 200 nm which may absorb the fluorescence photons and the 50-70 mTorr samples used are sufficient to allow substantial

absorption. Therefore, without more details about their experiment than is provided in their publications,[37,47–49] it is difficult to draw conclusions from their reported quantum yields. Similar studies have also noted this discrepancy, where Kavita and Das measure twice the quantum yield of other literature values, despite measuring comparable quantum yields for methyl iodide.[18]

As discussed above, the $\Phi(I^*)$ values measured here allowed the VMI studies to be analysed using spin-orbit-resolved *ab initio* calculations. These calculations revealed that the photodissociation is dominated by excitation to the $2A_1$ and $4A_1$ surfaces, adiabatically coupled to I and I* respectively. The TKER of the I fragment revealed that multiple channels are involved in the dissociation, resulting from excitation to the $4A_1$ surfaces followed by various curve crossings. The effects of these channels are indicated in Figure 2.11, reproduced from Sage *et al.*[1] where there is a comprehensive discussion of the dynamics.

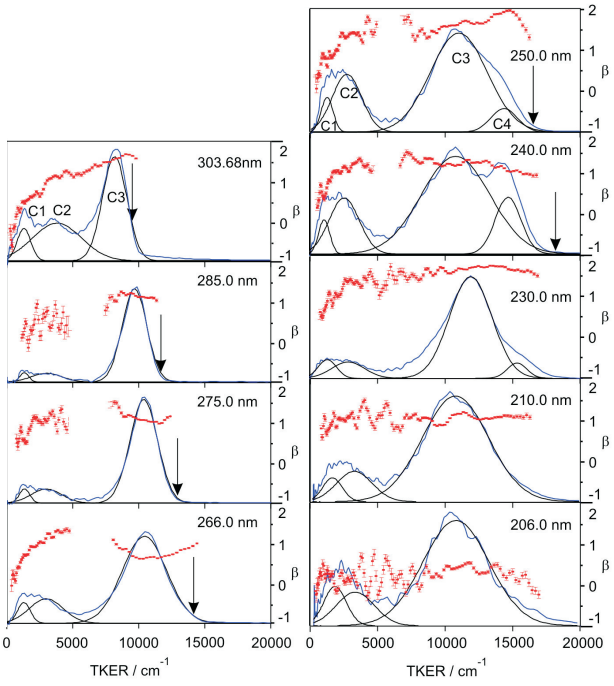

Figure 2.11: TKER distributions of the I product formed by photolysis of iodobenzene at the wavelengths indicated. The black arrows indicate the maximum possible TKER at each wavelength and the black lines are Gaussians fitted to show the different channels forming I fragments, reproduced from Sage *et al.*[1]

The population of I fragments produced *via* excitation to the $4A_1$ surfaces followed by curve crossing shows a wavelength dependence since the extent to which diabatic coupling occurs depends upon the initial transition probabilities, i.e. the amount of population initially created on the $4A_1$ surfaces upon absorption.

2.5.3 Effects of Fluorine Substitution

To further investigate the nature of the PESs involved, Murdock *et al.* selectively fluorinated the aromatic ring, altering the energies of the PESs, thereby altering the nature of the diabatic coupling of surfaces. The effects of fluorination on the TKER for the four fluorinated aryl-iodide compounds are shown in Figure 2.12, reproduced from Murdock *et al.*.[2] These TKERs show that the different channels leading to the I product are wavelength dependent and, by analogy with iodobenzene, must depend upon the initial transition probabilities. Hence, it is necessary to know the I* quantum yields, which have not been reported for these compounds, with the exception of C_6F_5I, as discussed earlier.

Two gain *vs* absorption measurements for C_6F_5I following photolysis at 248 nm and 266 nm are shown in Figure 2.13; the average $\Phi(I^*)$ recorded for these two wavelengths were the same. Figure 2.13a shows a spectrum recorded following 248 nm photolysis of C_6F_5I in which a quantum yield of $\Phi(I^*) = 0.29$ was measured. Figure 2.13b was recorded following 266 nm photolysis of C_6F_5I in which a quantum yield of $\Phi(I^*) = 0.37$ was measured. These two spectra illustrate that there is no evidence to support the I* quantum yields reported by Kavita and Das, $\Phi(I^*, 236\text{ nm}) = 0.63 \pm 0.015$ and $\Phi(I^*, 266\text{ nm}) = 0.58 \pm 0.03$ since this would show a much greater net gain at early times than either of the spectra in Figure 2.13 can support, as indicated in Figure 2.9.

The quantum yields for the other fluorinated aryl-iodides are given in Table 2.1 for both photolysis wavelengths, where it is interesting to see that there is very little variation between these iodo-compounds, despite the variation in the dynamics.

The relative insensitivity of the quantum yield to fluorination is an interesting result, and though the absolute values measured here do not compare well with Kavita and Das, given in Table 2.2, the quantum yield reported by them also appears relatively wavelength independent. This is particularly striking considering the effect fluorination

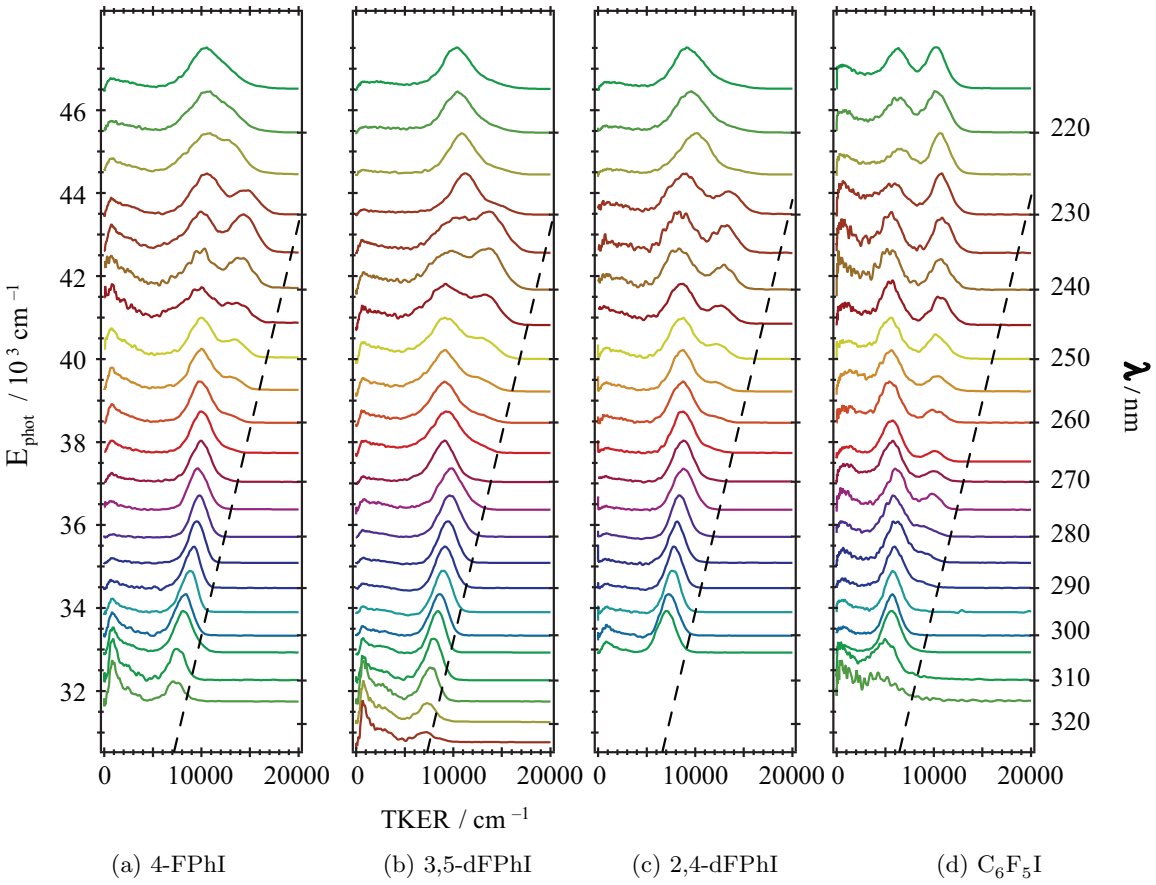

(a) 4-FPhI (b) 3,5-dFPhI (c) 2,4-dFPhI (d) C_6F_5I

Figure 2.12: TKER distributions of the I product formed following photolysis of (a) 4-fluoroiodobenzene, (b) 2,4-difluoroiodobenzene, (c) 3,5-difluoroiodobenzene and (d) pentafluoroiodobenzene over the 215 to 325 nm range, reproduced from Murdock at al.[2] The diagonal dashed line illustrates the maximum possible TKER.

Table 2.1: I* quantum yields for photodissociation of all species at 248 nm and 266 nm.

Iodo compound	$\Phi(I^*, 248\,\text{nm})$	$\Phi(I^*, 266\,\text{nm})$
Iodomethane	0.71 ± 0.04	0.71 ± 0.05
Iodobenzene	0.28 ± 0.04	0.32 ± 0.05
4-Fluoroiodobenzene	0.29 ± 0.03	0.31 ± 0.04
2,4-Difluoroiodobenzene	0.30 ± 0.05	0.36 ± 0.05
3,5-Difluoroiodobenzene	0.34 ± 0.03	0.33 ± 0.05
Pentafluoroiodobenzene	0.34 ± 0.05	0.34 ± 0.04

should have on the ring electron density and also the descent in symmetry in the case of 2,4-difluoroiodobenzene, in addition to the variation in the dynamics shown in Figure 2.12.

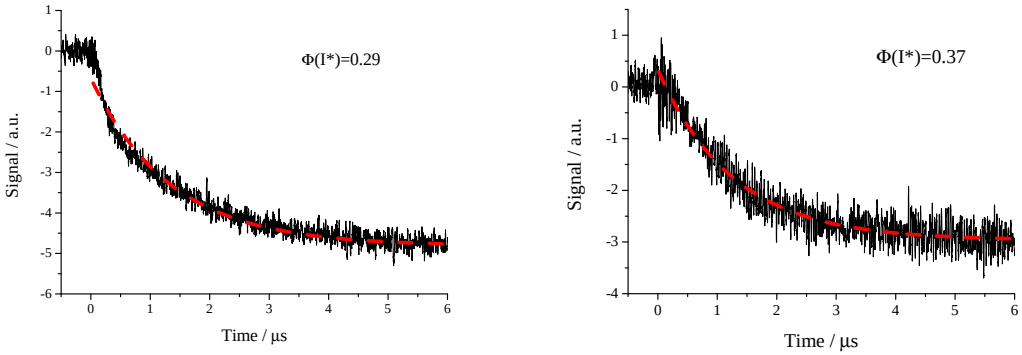

(a) 248 nm (b) 266 nm

Figure 2.13: An example gain *vs* absorption signal following (a) 248 nm and (b) 266 nm photolysis of C_6F_5I with the fitted exponential decay shown as a dashed line.

Table 2.2: I* quantum yields across a range of wavelengths as reported by Kavita & Das.[37]

Compound	222 nm	236 nm	266 nm	280 nm	305 nm
CH_3I	0.63 ± 0.02	0.69 ± 0.03	0.75 ± 0.003	0.69 ± 0.02	0.43 ± 0.01
C_6H_5I	0.62 ± 0.02	0.59 ± 0.01	0.51 ± 0.01	0.58 ± 0.01	0.24 ± 0.01
C_6F_5I	0.64 ± 0.03	0.63 ± 0.015	0.58 ± 0.03	0.59 ± 0.04	0.49 ± 0.03

As discussed for iodobenzene, the VMI and the I* quantum yields experiments complement spin-orbit resolved *ab initio* calculations on these fluorinated aryl-iodides, and a comprehensive discussion of the dynamics may be found in Sage *et al.*[1] Briefly, from Figure 2.11 and Figure 2.12, it can be seen that the I product is formed predominantly *via* channel 3 at all wavelengths and for all compounds. However, the fluorinated compounds show increasing contribution of channel 4 (C4) to formation of I products compared with iodobenzene, especially at shorter wavelengths. This behaviour can be seen by comparing the TKER distributions at 266 nm and 250 nm, where the latter shows the greater amount of I products formed in C4. The contribution C4 makes also varies between the fluorinated compounds. It is perhaps surprising that the varying contribution from the C4 channel between the compounds and across photolysis wavelength is *not* reflected in the I* quantum yields.

2.6 Conclusion

This chapter has reported the quantum yield of I* formation following photolysis of iodobenzene and its fluorine substituted analogues at two photolysis wavelengths, 248 nm and 266 nm. In contrast to the translational energy and recoil anisotropy of the I fragment, the quantum yield varies little between compounds or photolysis wavelength, remaining around $\Phi(I^*) = 0.3$. This work complements studies investigating the energy released into translation as a function of photolysis wavelength, where the PTS technique and VMI are incapable of measuring the quantum yield. Since it is necessary to know the quantum yield to account for the proportion of products sampling the various PESs, these quantum yield measurements form an important part of the understanding of the photodissociation dynamics of aryl iodides.

The signals used to determine the quantum yield of the aryl iodides consistently showed no gain. This is in direct contradiction to previous studies by Kavita and Das, but consistent with Pence *et al.*, and it was concluded there is a significant source of error in the work of Kavita and Das.

References

[1] A. G. Sage et al., Physical chemistry chemical physics : PCCP (2011).

[2] D. Murdock, M. B. Crow, G. A. D. Ritchie, and M. N. R. Ashfold, The Journal of Chemical Physics **136**, 124313 (2012).

[3] M. N. R. Ashfold et al., Physical chemistry chemical physics : PCCP **12**, 1218 (2010).

[4] Y. Wen, J. Segall, M. Dulligan, and C. Wittig, The Journal of Chemical Physics **101**, 5665 (1994).

[5] S. Satyapal, J. Park, R. Bersohn, and B. Katz, The Journal of Chemical Physics **91**, 6873 (1989).

[6] S.-H. Lee, H.-I. Lee, and Y. T. Lee, The Journal of chemical physics **121**, 11053 (2004).

[7] S. Harich, J. J. Lin, Y. T. Lee, and X. Yang, The Journal of Physical Chemistry A **103**, 10324 (1999).

[8] M. G. D. Nix, A. L. Devine, B. Cronin, R. N. Dixon, and M. N. R. Ashfold, The Journal of chemical physics **125**, 133318 (2006).

[9] M. N. R. Ashfold, B. Cronin, a. L. Devine, R. N. Dixon, and M. G. D. Nix, Science (New York, N.Y.) **312**, 1637 (2006).

[10] C. Ratzer, J. Küpper, D. Spangenberg, and M. Schmitt, Chemical Physics **283**, 153 (2002).

[11] M. N. R. Ashfold et al., Proceedings of the National Academy of Sciences of the United States of America **105**, 12701 (2008).

[12] B. Cronin, M. G. D. Nix, R. H. Qadiri, and M. N. R. Ashfold, Physical Chemistry Chemical Physics **6**, 5031 (2004).

[13] J. Wei, a. Kuczmann, J. Riedel, F. Renth, and F. Temps, Physical Chemistry Chemical Physics **5**, 315 (2003).

[14] M. Barbatti, M. Vazdar, A. J. a. Aquino, M. Eckert-Maksić, and H. Lischka, The Journal of chemical physics **125**, 164323 (2006).

[15] A. L. Devine, B. Cronin, M. G. D. Nix, and M. N. R. Ashfold, The Journal of chemical physics **125**, 184302 (2006).

[16] M. Vazdar, M. Eckert-Maksić, M. Barbatti, and H. Lischka, Molecular Physics **107**, 845 (2009).

[17] B. O. Roos, P.-k. Malmqvist, V. Molina, L. Serrano-Andres, and M. Merchan, The Journal of Chemical Physics **116**, 7526 (2002).

[18] D. K. Zaouris et al., The Journal of Chemical Physics **135**, 094312 (2011).

[19] S. Yabushita and K. Morokuma, Chemical Physics Letters **153**, 517 (1988).

[20] A. B. Alekseyev, H.-P. Liebermann, and R. J. Buenker, The Journal of Chemical Physics **134**, 044303 (2011).

[21] Y. Amatatsu, K. Morokuma, and S. Yabushita, The Journal of Chemical Physics **94**, 4858 (1991).

[22] Y. Amatatsu, S. Yabushita, and K. Morokuma, The Journal of Chemical Physics **104**, 9783 (1996).

[23] C. R. Evenhuis and U. Manthe, The journal of physical chemistry. A **115**, 5992 (2011).

[24] A. García-Vela and L. Bañares, Physical chemistry chemical physics : PCCP **13**, 2228 (2011).

[25] G. Gitzinger et al., The Journal of Chemical Physics **132**, 234313 (2010).

[26] L. Rubio-Lago, A. García-Vela, A. Arregui, G. A. Amaral, and L. Bañares, The Journal of Chemical Physics **131**, 174309 (2009).

[27] L. Rubio-Lago et al., Physical chemistry chemical physics : PCCP **13**, 8186 (2011).

[28] M. G. González, J. D. Rodríguez, L. Rubio-Lago, a. García-Vela, and L. Bañares, Physical chemistry chemical physics : PCCP **13**, 16404 (2011).

[29] D. W. Chandler and P. L. Houston, The Journal of Chemical Physics **87**, 1445 (1987).

[30] J. Black, Chemical Physics **125**, 375 (1988).

[31] M. Shapiro and R. Bersohn, The Journal of Chemical Physics **73**, 3810 (1980).

[32] H. Guo and G. C. Schatz, The Journal of Chemical Physics **93**, 393 (1990).

[33] A. T. J. B. Eppink and D. H. Parker, The Journal of Chemical Physics **109**, 4758 (1998).

[34] A. Eppink and D. H. Parker, The Journal of Chemical Physics **110**, 832 (1999).

[35] M. N. R. Ashfold et al., Physical chemistry chemical physics : PCCP **8**, 26 (2006).

[36] W. H. Pence, S. L. Baughcum, and S. R. Leone, The Journal of Physical Chemistry **85**, 3844 (1981).

[37] K. Kavita and P. K. Das, The Journal of Chemical Physics **117**, 2038 (2002).

[38] W. P. Hess, S. J. Kohler, H. K. Haugen, and S. R. Leone, The Journal of Chemical Physics **84**, 2143 (1986).

[39] S. R. Taylor, *Diode Laser Based Studies of Transient Species*, PhD thesis, University of Oxford, 2009.

[40] A. B. Callear and J. F. Wilson, Transactions of the Faraday Society **63**, 1358 (1967).

[41] Z.-N. Gu, A. T. Young, and P. L. Houston, International Journal of Chemical Kinetics **16**, 669 (1984).

[42] G. Van Veen, T. Baller, A. De Vries, and N. Van Veen, Chemical Physics **87**, 405 (1984).

[43] A. Gilchrist et al., The Journal of Physical Chemistry. A **112**, 4531 (2008).

[44] G. Hancock, G. Richmond, G. A. D. Ritchie, and S. Taylor, Physical chemistry chemical physics : PCCP **11**, 6415 (2009).

[45] P. Brewer, P. Das, G. S. Ondrey, and R. Bersohn, The Journal of Chemical Physics **79**, 720 (1983).

[46] S. J. Riley and K. R. Wilson, Faraday Discussions of the Chemical Society **53**, 132 (1972).

[47] S. Uma and P. K. Das, Canadian Journal of Chemistry **72**, 865 (1994).

[48] S. Uma and P. K. Das, The Journal of Chemical Physics **104**, 4470 (1996).

[49] K. Kavita and P. K. Das, The Journal of Chemical Physics **112**, 8426 (2000).

Chapter 3

Development of an Ultraviolet Continuous-wave Source: Determination of Absolute Absorption cross sections for the $A - X$ $2_0^2 4_0^1$ & $2_0^2 4_0^3$ bands of Formaldehyde

In this chapter the extension of narrow bandwidth tunable near-infrared diode lasers to the ultraviolet is explored. A UV spectrometer based upon sum frequency generation with a continuous-wave 532 nm source and a selection of near-infrared diode lasers is characterised and implemented in studies of the atmospherically important formaldehyde molecule. In particular, the sub-Doppler resolution of the spectrometer is utilised to measure absolute absorption cross sections, Doppler limited rotational lines and predissociation of the excited state.

3.1 Introduction

Formaldehyde is present in the atmosphere both as a by-product of industry and due to the oxidation of many volatile organic compounds (VOCs) such as methane, acetone and isoprene.[1–4] Hence, formaldehyde is arguably the most important carbonyl compound in the atmosphere, with concentrations of 50 pptv (parts per trillion, 10^{12}, by volume) in clean tropospheric air in the Antarctic[5] and urban concentrations of up to 70 ppbv (parts per billion, 10^9, by volume).[6,7] In addition, the World Health Organisation's recommended exposure limit is 80 ppbv, averaged over 30 minutes.[8]

The dominant loss processes for atmospheric formaldehyde are ultraviolet photolysis and oxidation by the hydroxyl radical.[9] UV photolysis occurs *via* the $n \rightarrow \pi^*$ electronic transition, discussed in depth below, with the resulting electronically excited state undergoing two dissociation pathways leading to either molecular products or radical products, shown in equations 3.1 and 3.2 respectively. The threshold energies for each process are shown in parentheses.[10–12]

$$\mathrm{HCHO}(S_0) + h\nu \rightarrow \mathrm{HCHO}(S_1) \rightarrow \mathrm{H_2} + \mathrm{CO} \quad (27\,720\,\mathrm{cm^{-1}}) \tag{3.1}$$

$$\mathrm{HCHO}(S_0) + h\nu \rightarrow \mathrm{HCHO}(S_1) \rightarrow \mathrm{HCO} + \mathrm{H} \quad (30\,328.5\,\mathrm{cm^{-1}}) \tag{3.2}$$

The quantum yield of photolysis of HCHO is therefore wavelength dependent, with approximately equal contributions from both channels under atmospheric conditions.[13] The products of both pathways play significant roles in atmospheric chemistry. The radicals react with atmospheric O_2 to form the hydroperoxy radical HO_2,[14] which in turn takes part in atmospheric cycles, reacting with NO to produce NO_2 and OH; and the CO product is oxidised to give CO_2, which must be accounted for due to its environmental impact.[15]

With such a diverse participation in atmospheric chemistry and large global fluctuations in concentrations there is great interest in modelling formaldehyde's atmospheric chemistry. This requires precise atmospheric concentrations to be determined from both satellite and ground based spectrometers, both of which require knowledge of high-resolution absorption cross sections and pressure-induced broadening parameters.[16–20] Numerous studies of the $\tilde{A}\ ^1A_1 - \tilde{X}\ ^1A_1$ band exist in the literature,[9,21–33] dating as far back as 1934.[34] However, most recently Smith *et al.*[9] and Tatum Ernest *et al.*[35] have recorded absorption cross sections across the entire band, from 304 nm to 330 nm, with instrument resolutions of $0.35\,\mathrm{cm^{-1}}$ and $0.09\,\mathrm{cm^{-1}}$, respectively; both higher than the thermal Doppler width of $0.069\,\mathrm{cm^{-1}}$. Both studies used pulsed laser absorption spectroscopy to record spectra, hence the relatively broad bandwidths, with Smith *et al.* double passing the radiation through the absorption cell to achieve a path length of 66.5 cm whereas Tatum Ernest *et al.* triple passed the radiation through a longer cell to achieve a total path length of 375 cm. Recently, Motsch *et al.*[32] have used the frequency-doubled output

of a continuous-wave ring dye laser to generate tunable UV radiation, with an instrument resolution of $1.67 \times 10^{-5}\,\mathrm{cm}^{-1}$. The instrument was used to investigate the $2_0^1 4_0^1$ and $2_0^2 4_0^1$ vibrational bands within the $\tilde{A}\,^1A_1 - \tilde{X}\,^1A_1$ band using multi-pass absorption spectroscopy with a path length of 315 cm. Similarly, the work discussed in this chapter uses frequency mixing of a near-infrared diode laser and a cw 532 nm laser source to probe the rotational structure of three vibronic bands within the $\tilde{A}\,^1A_1 - \tilde{X}\,^1A_1$ band at a resolution of $3.3 \times 10^{-4}\,\mathrm{cm}^{-1}$. the data were taken partly in collaboration with Taylor[36] and published in Crow *et al.*.[33] The 325 nm radiation was generated using a 532 nm fixed-frequency high-powered laser and a tunable 825 nm diode laser, arranged in an external cavity to enhance tunability. Once the output of the 532 nm and 825 nm lasers were combined, our spectrometer was used to study the $2_0^2 4_0^1$ and $2_0^2 4_0^3$ bands to determine absolute absorption cross sections in both bands as well as the lifetimes of the excited states in the $2_0^2 4_0^3$ band.

3.2 Nonlinear Optical Phenomena

An electromagnetic wave propagating through a medium induces a polarisation, $P(t)$, which depends upon the electric field strength of the radiation, $E_a(t)$. In linear optics this polarisation varies linearly with the field strength according to $P(t) = \varepsilon_0 \chi E_a(t)$, where χ is the first order (or linear) susceptibility. However, in nonlinear optics the presence of the high electric field strength associated with laser light induces higher order contributions to the polarisation, shown in equation 3.3. The coefficients χ_n are the nth order optical susceptibilities.[37]

$$P(t) = \varepsilon_0 \chi E_a(t) + \varepsilon_0 \chi_2 E_a^2(t) + \varepsilon_0 \chi_3 E_a^3(t) + \ldots \tag{3.3}$$

Of particular interest for this work is the second order contribution to the polarisation, the term responsible for the processes of sum frequency generation, difference frequency generation and second harmonic generation, discussed below. The second order optical susceptibility is zero in centrosymmetric crystals, therefore an appropriate medium needs to be chosen in order to observe these second order optical phenomena. For reasons discussed below, beta barium borate (β-BaB_2O_4 or BBO) has been chosen in this work.

In the presence of two laser beams of frequency ω_1 and ω_2, the total electric field

strength in the medium may be described as the sum of the two individual electric fields:

$$E = (E_1 e^{-i\omega_1 t} + E_1^\star e^{i\omega_1 t}) + (E_2 e^{-i\omega_2 t} + E_2^\star e^{i\omega_2 t}). \tag{3.4}$$

The second order polarisation, P_2, induced in the material can be described as shown in equation 3.5, and contains terms at the sum and difference of the frequencies, $\omega_2 + \omega_1$ and $\omega_2 - \omega_1$, in addition to frequency doubling, $2\omega_1$ & $2\omega_2$.

$$\begin{aligned} P_2 &= \varepsilon_0 \chi_2 E^2 \\ &= \varepsilon_0 \chi_2 \big[E_1^2 e^{-i2\omega_1 t} + (E_1^\star)^2 e^{i2\omega_1 t} \\ &\qquad + E_2^2 e^{-i2\omega_2 t} + (E_2^\star)^2 e^{i2\omega_2 t} \\ &\qquad + 2E_1 E_1^\star + 2E_2 E_2^\star \\ &\qquad + 2E_1 E_2^\star e^{i(\omega_2 - \omega_1)t} + 2E_1^\star E_2 e^{-i(\omega_2 - \omega_1)t} \\ &\qquad + 2E_1 E_2 e^{-i(\omega_2 + \omega_1)t} + 2E_1^\star E_2^\star e^{i(\omega_2 + \omega_1)t} \big] \end{aligned} \tag{3.5}$$

The sum frequency terms, $\omega_2 + \omega_1$, are of particular interest here as they refer to radiation generated at shorter wavelengths. The frequency doubling terms, $2\omega_1$ & $2\omega_2$, are particularly useful when working with high-power sources, such as dye lasers and some solid state lasers, for which doubling the frequency of light in the visible region of the spectrum allows access to the ultraviolet region. In contrast to these, the difference frequency terms, $\omega_2 - \omega_1$, allow access to the mid-infrared region, where it is difficult to manufacture diode lasers; however, the invention of quantum cascade lasers which operate in the mid infrared is starting to replace this method with much more manageable sources.[38] A schematic in Figure 3.1 demonstrates the photons involved.[37]

3.3 Sum Frequency Generation

From equation 3.5, the frequency of the resulting beam from sum frequency generation should be $\omega_3 = \omega_1 + \omega_2$, where the subscripts are chosen in order of increasing frequency, $\omega_1 < \omega_2 < \omega_3$. The three beams may be described in terms of their wavevectors, k_ω, which lie parallel to the direction of beam propagation through the medium. The magnitude of

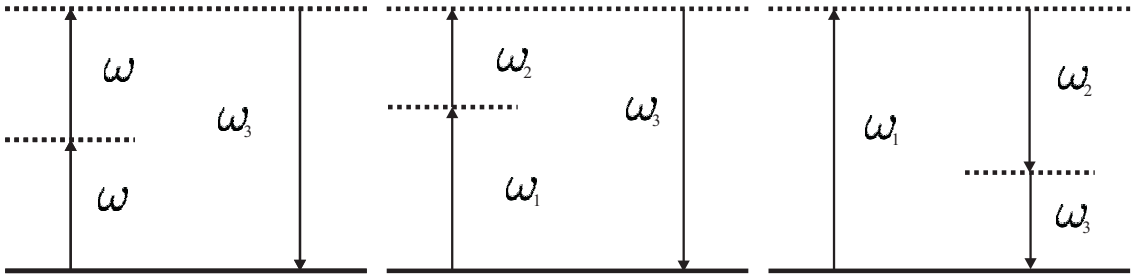

(a) Second Harmonic Generation (b) Sum Frequency Generation (c) Difference Frequency Generation

Figure 3.1: Illustration of some selected nonlinear optical mixing schemes.

k_ω is given by:

$$k_\omega = \frac{\eta\omega}{c} = \frac{2\pi\eta}{\lambda}, \tag{3.6}$$

where η is the refractive index of the medium.

In order to most efficiently combine two laser beams and hence obtain maximum ultraviolet power, equation 3.7 must be satisfied. This is known as the phase matching criterion and ensures that the radiation generated throughout the medium is produced in a coherent manner, namely that each generated wave constructively adds to the whole by ensuring that each oscillating dipole in the crystal lattice is oscillating in phase.[37]

$$\boldsymbol{k_3 = k_1 + k_2} \tag{3.7}$$

Phase matching within BBO is made possible by virtue of its birefringence, i.e. it displays different refractive indices for light polarised perpendicular or parallel to the plane containing the optical axis, z, and the direction of propagation, k. Light polarised perpendicular to this plane is deemed to be in the ordinary plane and experiences a refractive index, η_o, which is independent of the angle between the optical axis and the direction of propagation, θ; this is often called an ordinary beam. Conversely, light polarised parallel to this plane is said to be in the extraordinary plane and experiences a refractive index, η_e, which is dependent upon the angle θ, and is often called an extraordinary beam. The wavevector, optical axis and ordinary and extraordinary beams are illustrated in Figure 3.2.[37]

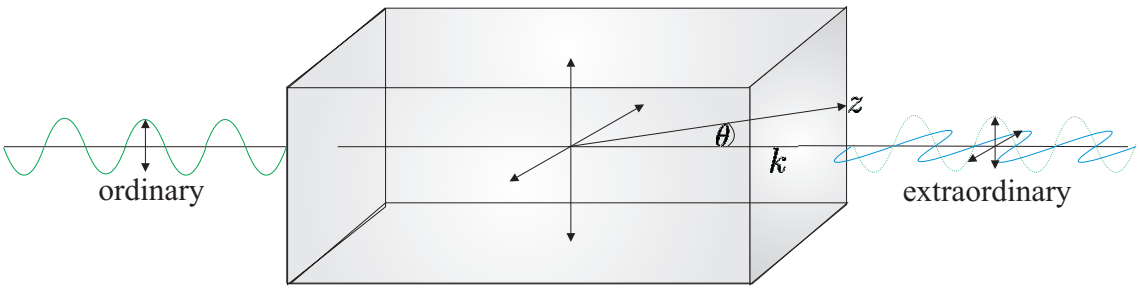

Figure 3.2: Illustration of the angle, θ, between the optical axis, z, and direction of propagation, k, with the generated sum frequency beam (blue) polarised in the extraordinary plane.

BBO is a negative uniaxial crystal, $\eta_e < \eta_o$, and phase matching is achieved by generating an extraordinary beam. Experimentally, it is easiest to do this by combining two ordinary beams to produce the third extraordinary beam, a process known as Type I or <ooe> frequency mixing. It is also possible to phase match by combining an extraordinary beam with an ordinary beam, known as Type II or <eoe> frequency mixing.[37]

The wavelength dependent refractive indices for BBO are given by the Sellmeier equations (equations 3.8 and 3.9), where the wavelength, λ, is in μm.[39]

$$\eta_o^2(\lambda) = 2.7359 + \frac{0.01878}{\lambda^2 - 0.01822} - 0.01354\lambda^2 \tag{3.8}$$

$$\eta_e^2(\lambda) = 2.3753 + \frac{0.01224}{\lambda^2 - 0.01667} - 0.01516\lambda^2 \tag{3.9}$$

Table 3.1: Values of the refractive indices in the BBO crystal for wavelengths relevant to 325 nm generation.

λ/nm	η_o	η_e
835	1.544	1.670
532	1.555	1.674
325	1.585	1.717

Using these equations in addition to an adjusted form of equation 3.7, given as equation 3.10, it is possible to determine the optimum value of $\eta_e(\theta)$.

$$\frac{\eta_{o,1}}{\lambda_1} + \frac{\eta_{o,2}}{\lambda_2} = \frac{\eta_{e,3}(\theta_m)}{\lambda_3} \tag{3.10}$$

Since the refractive index for the extraordinary beam is dependent upon the angle θ, θ must be optimised. By using the equation of an ellipse and the fact that $\eta_e(\theta = 0) = \eta_o$, illustrated in Figure 3.3, the phase angle, θ_m, may be calculated, according to:

$$\sin^2 \theta_m = \frac{\eta_{e,3}^{-2}(\theta_m) - \eta_{o,3}^{-2}}{\eta_{e,3}^{-2}(\frac{\pi}{2}) - \eta_{o,3}^{-2}}. \tag{3.11}$$

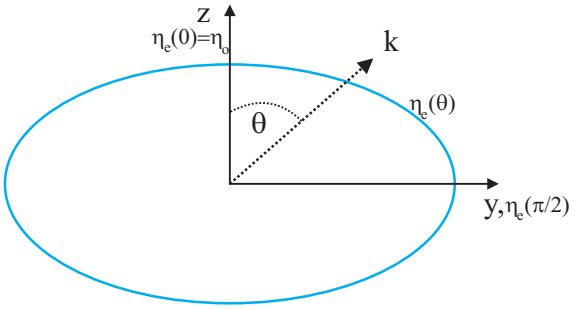

Figure 3.3: Illustration of the variation of $\eta_e(\theta)$ with the angle between the optical axis, z, and direction of beam propagation, $\mathbf{k}$.

This returns a value of $\theta_m = 35.8°$. As discussed above, θ is the angle between the optical axis, z, and the direction of propagation of all of the beams, $\mathbf{k}$. It is therefore easiest to perform phase matching by having the crystal cut such that the direction of propagation through the crystal is parallel to its long edge and is already at angle θ_m to the optical axis. This allows for most efficient phase matching. In addition to satisfying the phase matching condition, the two lasers incident on the BBO crystal must be focussed to produce significant UV intensities through the crystal. Assuming Gaussian input beams, it is possible to predict a theoretical maximum for the mixing process.[40] The power of the third beam, P_3, is dependent on the power of the input beams, P_1 and P_2, with the constant of proportionality, γ, accounting for properties of the beams within the BBO crystal.

$$P_3 = \gamma P_1 P_2 \tag{3.12}$$

Within the medium, γ accounts for the frequencies of the input radiation, ω_n, the focussing parameter of the beam, h, the nonlinearity of the medium, d_{eff}, the length of the

crystal, l, and the refractive index of the generated beam, $\eta_{e,3}$, as in equation 3.13.[40]

$$\gamma = \frac{4\omega_1\omega_2\omega_3}{\pi\varepsilon_0 c^4}\frac{h}{\eta_{e,3}^2}d_{\text{eff}}^2 l \tag{3.13}$$

The effective nonlinearity of the crystal, d_{eff}, is given by equation 3.14, where $\theta = \theta_m$. For Type I phase matching, $\phi = \frac{\pi}{2}$ and d_{ij} are tensors experimentally determined for a material. For BBO, $d_{15} = 0.12$ pmV^{-1} and $d_{22} = 1.78$ pmV^{-1}.[41]

$$d_{\text{eff}} = d_{15}\sin\theta - d_{22}\cos\theta\sin 3\phi \tag{3.14}$$

When dealing with highly focussed beams, account must be taken of the walk-off angle, ρ, given in equation 3.15, which is in turn related to the double refraction parameter, B, as in equation 3.16. The walk-off angle represents the difference between the wavevector in the extraordinary plane (k_3) and the Poynting vector, the direction of energy transfer, which an extraordinary polarised beam experiences due to the angle dependent refractive index in the extraordinary plane. Since $B > 1.5$, the theory of Boyd and Kleinman allows h to be calculated through equation 3.17.[40]

$$\rho = \tan^{-1}\left[\left(\frac{\eta_o}{\eta_e}\right)^2\tan\theta_m\right] - \theta_m \tag{3.15}$$

$$B = \frac{\rho(lk_3)^{\frac{1}{2}}}{2} \tag{3.16}$$

$$h = \frac{0.714}{B} \tag{3.17}$$

The values determined from the above discussion are summarised in Table 3.2 and the theoretical conversion efficiency, γ, was calculated to be 3.07×10^{-4} W^{-1}.

Table 3.2: The values used in the calculation of γ.

d_{eff}/pmV^{-1}	$\eta_{e,3}$	θ_m/rad	ρ/rad	B	h	γ/W^{-1}
1.51	1.551	0.625	0.0779	15.7	0.046	3.07×10^{-4}

3.4 Experimental Set Up

The two lasers incident on the BBO crystal were a frequency-doubled, diode pumped Nd:YVO_4 laser (Coherent VERDI V5) operating at a fixed wavelength of 532.19 nm; and an external cavity diode laser (Sacher Lasertechnik, Littrow TEC-100) operating between 825 nm and 875 nm. The near-infrared diode laser was exchanged for other lasers in order to allow access to a range of UV wavelengths studied throughout this chapter, and these will be highlighted as appropriate later in this chapter. In order to prevent back reflections into the diode, which interfere with its single-mode operation, the output of the near-infrared laser is first passed through an optical isolator (Isowave I-7090-CM). The polarisations of the two beams are then matched using half waveplates. A partial reflection, $\approx 4\%$, of the near-infrared laser is monitored with a Fabry-Perot interferometer (Thorlabs SA200-6A, 2 GHz free spectral range), which provides a frequency scale for measurements.

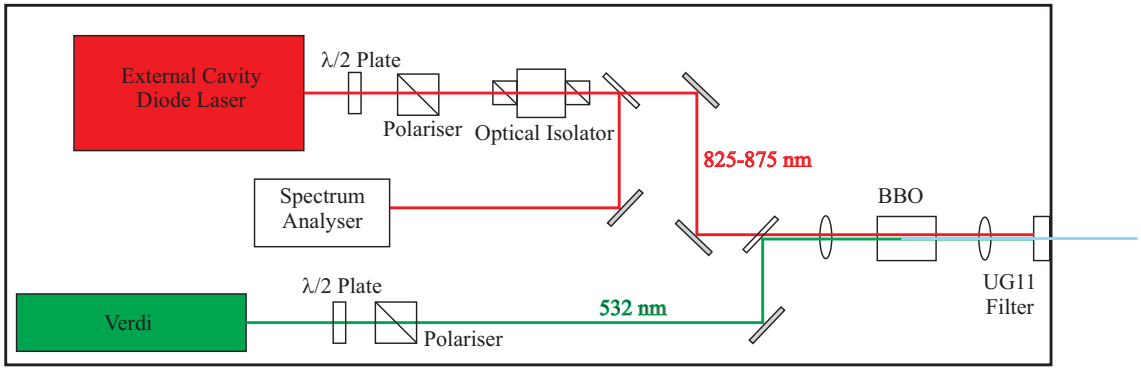

Figure 3.4: Experimental set up used to produce UV radiation.

The two beams are aligned to overlap in space, propagating in the same direction, by a dichroic mirror and then focused by a 10 cm focal length lens through the centre of a 4 mm × 4 mm × 10 mm BBO crystal. The radiation is then re-collimated and the UV radiation is separated from the two incident beams by a UV transmission filter (UG11, $\approx$ 90% transmission around 300 nm). The equipment used to produce the tunable UV radiation is then enclosed, as shown in Figure 3.4, with the UV radiation exiting through the filter. The UV light is used as a standard diode laser source for the experiments with changes in the frequency of the near-infrared laser causing the same frequency change in

the UV.

The laser powers incident on the BBO crystal throughout this work were typically $P_1 = 30\,\text{mW}$ and $P_2 = 2\,\text{W}$. This generated up to $10.5\,\mu\text{W}$ of UV light, which corresponds to 57% of the theoretical maximum. Previous experiments of this nature with diode laser sources have achieved 59%,[42] 20%,[43] and 34%;[44] thus this experiment exhibits frequency mixing efficiency at the high end of the range achieved experimentally, probably due to the high quality Gaussian beam outputs of the two lasers in this set up. Previous studies typically generated low UV powers (sub-microwatt, often $\approx$ 20 nW) since the incident beams are usually milliwatt diode lasers. In this study, the high-power 532 nm source ($>$ 2 W) allows microwatts of UV radiation to be generated, thereby producing significantly more UV radiation than in these previous studies.

The resulting UV radiation, produced between 323.5 nm and 331 nm, was passed through a 50 cm long absorption cell containing samples of formaldehyde and then detected using a photodiode (Thorlabs PDA 25K). Background measurements were made by redirecting the UV radiation with a flip mirror placed before the absorption cell, and detecting the radiation with a second photodiode (Thorlabs PDA25K), so as to avoid the need to evacuate the absorption cell.

Monomeric formaldehyde samples were prepared in the manner described by Spence and Wild involving cracking paraformaldehyde (Aldridge, $>$ 95%) by heating to over 383 K in a vacuum.[45] The resulting vapour was purified by passing through a dry ice/acetone trap, removing the acetone and acetaldehyde by-products of the pyrolysis of paraformaldehyde, and collecting the formaldehyde in a liquid nitrogen trap. Continuous pumping of the collected formaldehyde removed excess oxygen, which is necessary since the presence of oxygen catalyzes polymerization.[45] The formaldehyde samples were then pumped through PTFE tubing to the absorption cell, with measurements taken on static samples and fresh samples used for each measurement. Fourier transform infrared absorption spectroscopy (FTIR) measurements on the monomeric formaldehyde samples produced by this method showed no signs of infrared active impurities, such as H_2O, CO_2 or acetone.

3.5 Formaldehyde Spectroscopy: $\tilde{A}\ ^1A_2 - \tilde{X}\ ^1A_1$

Formaldehyde is a planar molecular with C_{2v} symmetry and an electronic ground state of symmetry $^1A_1$. Absorption *via* the $\tilde{A}\ ^1A_2 - \tilde{X}\ ^1A_1$ transition, between 300 nm and 340 nm, involves excitation of an electron from a non-bonding orbital on the oxygen to the antibonding π^* orbital. This excited electronic configuration gives rise to both a singlet and a triplet state, with the transition to the triplet state from the ground state spectroscopically forbidden (by the selection rule $\Delta S = 0$). Both excited states are preferentially bent into a pyramidal shape, in which the CH_2 group is bent out of the parent molecular plane by 38°. The $\tilde{A}\ ^1A_2 - \tilde{X}\ ^1A_1$ transition is formally forbidden by symmetry considerations, but coupling to the out of plane bending vibration makes the transition vibronically allowed.[46,47]

Formaldehyde has six vibrational modes, illustrated in Appendix B, which are all infrared and Raman active. The $\tilde{A}\ ^1A_2 - \tilde{X}\ ^1A_1$ transition primarily involves two of these modes, the C–O stretch, ν_2 and the out of plane bend, ν_4.[12] The C–O stretch has a strong transition dipole moment, lending strength to the absorption, whereas the bending motion makes the transition vibronically allowed. Weaker vibrational features utilise the CH_2 group 'wiggle', ν_5, to make the transitions vibronically accessible.

Prior to the work of Tatum Ernest *et al.*,[35] the highest resolution spectra of the complete $\tilde{A}\ ^1A_2 - \tilde{X}\ ^1A_1$ band had been recorded by Smith *et al.*[9] using the frequency-doubled output of a tunable dye laser pumped by the frequency-doubled output of a Nd:YAG laser, with an instrument resolution of $0.35\,\mathrm{cm}^{-1}$, determined by comparison between simulated and recorded spectra. The instrument resolution contributed significantly to the observed linewidth;[9] however, Smith *et al.* were able to refine the spectral constants of the various vibronic transitions using the spectral simulation program PGOPHER,[48] starting with the constants of Clouthier and Ramsay.[47] These constants have been further refined, though only very slightly from the values of Smith *et al.*, by Motsche *et al.*[32] for the $2_0^1 4_0^3$ and $2_0^2 4_0^1$ bands, the latter of which has also been studied in this work.[33] The values determined by Smith *et al.* and Motsch *et al.* were also used in the work of Tatum Ernest *et al.*.[35]

Since the studies described in this thesis were undertaken, Tatum Ernest *et al.*[35] have recorded a relatively high resolution spectrum of the whole $\tilde{A}\ ^1A_2 - \tilde{X}\ ^1A_1$ band with a quoted laser bandwidth of $0.09\,\mathrm{cm}^{-1}$. The bandwidth of Tatum Ernest *et al.* is signifi-

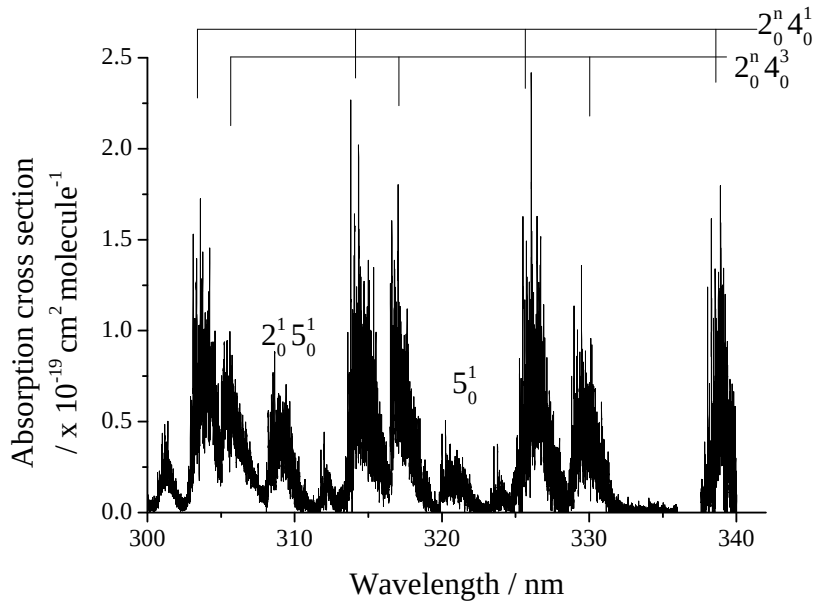

Figure 3.5: The $\tilde{A}\ ^1A_2 - \tilde{X}\ ^1A_1$ band with the vibronic transitions labelled, reproduced from Smith *et al.*[9]

cantly broader than the Doppler width of HCHO at room temperature, $0.069\,\mathrm{cm}^{-1}$, and significantly broader than the $3.3 \times 10^{-4}\,\mathrm{cm}^{-1}$ resolution of the spectrometer developed in this work. In their study they combine the fundamental output of an injection seeded Nd:YAG (1064 nm) with the output from a frequency-doubled dye laser, pumped by the third harmonic (355 nm) of the same Nd:YAG laser, using a KDP crystal. The bandwidth of the resulting UV radiation was quoted as being determined using a wavemeter. The results discussed in this chapter will be compared with the work of Tatum Ernest *et al.* to illustrate the strengths of this spectrometer.[35]

The $\tilde{A}\ ^1A_2 - \tilde{X}\ ^1A_1$ transition is shown in Figure 3.5, reproduced from Smith *et al.* The vibrational structure is assigned using the notation M^a_b for a transition involving vibration M with a quanta in the excited state and b quanta in the ground state. The rotational structure across the vibronic bands is evident in this spectrum, and by fitting to the whole spectrum the rotational constants were optimised.[9,47]

Formaldehyde has three different moments of inertia ($I = \sum m_i r_i^2$), defined about the three perpendicular rotational axes of the molecule. These moments of inertia are in the

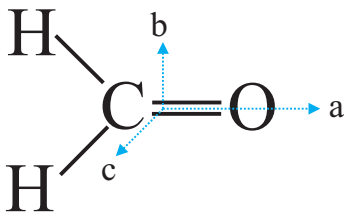

Figure 3.6: Illustration of the rotational axis of formaldehyde, labelled according to the moments of inertia in the text.[46,47]

order $I_c > I_b > I_a$, hence the labeling of the rotational axes in Figure 3.6. Formaldehyde is a prolate near-symmetric rotor with $I_c \approx I_b > I_a$, and rotational energy levels, $F(J, K)$, described by equation 3.18, where $\bar{B} = 1/2(B + C)$ and the quantum number K describes the projection of the rotational quantum number J on to the principal (a) axis, taking values $K = 0, \pm 1, \pm 2 \ldots \pm J$.[46]

$$F(J, K) \approx \bar{B}J(J + 1) + (A - \bar{B})K^2 \tag{3.18}$$

The rotational constants A, B and C are given by equations 3.19, 3.20 and 3.21, respectively. Since $I_c \approx I_b$, $B \approx C$ hence $\bar{B} \approx B$ and equation 3.18 reduces approximately to that for a prolate symmetric rotor[i].[46]

$$A = \frac{h}{8\pi^2 I_a} \tag{3.19}$$

$$B = \frac{h}{8\pi^2 I_b} \tag{3.20}$$

$$C = \frac{h}{8\pi^2 I_c} \tag{3.21}$$

The rotational energy levels are described by the quantum numbers J, K_a and K_c, where K_a and K_c are the projection of J onto the a and c axes, respectively. Transitions between these energy levels are subject to the selection rules: $\Delta J = \pm 1$, $\Delta K_a = 0$ and $\Delta K_c = \pm 1$, with the transitions labelled as ${}^{\Delta K}\Delta J_{K''_a, K''_c}(J'')$, i.e. ${}^{p}Q_{2,12}(13)$.[46,47] PGOPHER uses the rotational lines to simulate the vibronic bands studied by Smith *et al.* and allowed Smith *et al.* to optimise the rotational constants in order to fit their measurements, despite the instrumental broadening in their measurements. It will be

[i] for which: $F(J, K) = BJ(J + 1) + (A - B)K^2$

shown below that these optimised rotational constants are in good agreement with our high-resolution data.

3.6 $\tilde{A}\ ^1A_2 - \tilde{X}\ ^1A_1\ 2_0^2 4_0^1$ Band

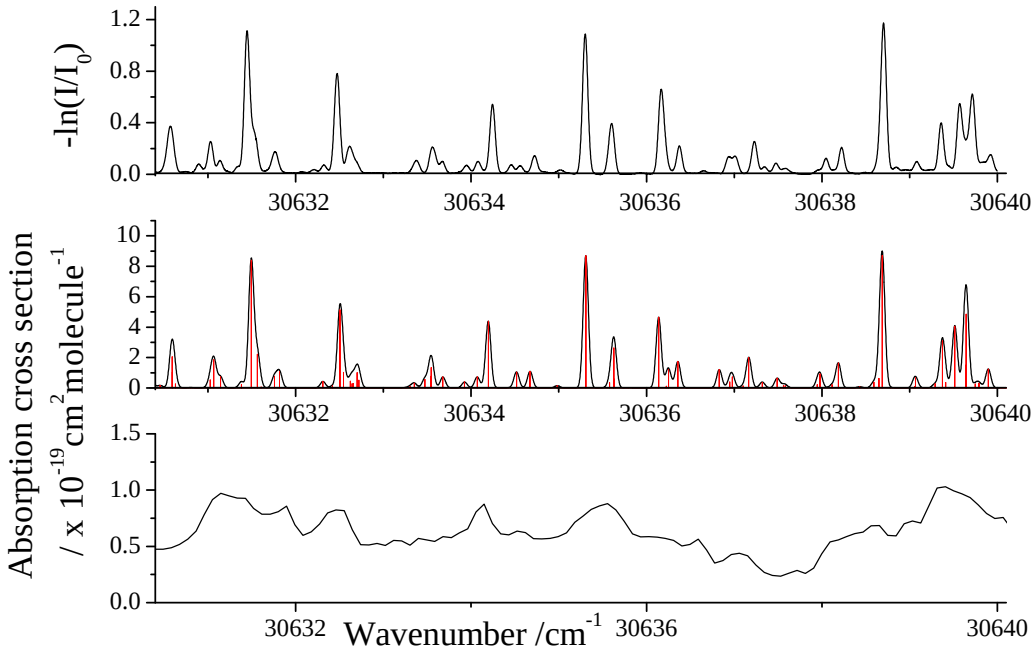

Figure 3.7: Region scan from 30630 – 30640 cm^{-1}. Top: recorded with 700 mTorr of formaldehyde. Middle: PGOPHER simulation of this region, red lines indicate the rotational line and the black is a simulation with the expected thermal linewidth, $0.07\,cm^{-1}$.[48] Bottom: corresponding lower resolution scan measured by Smith *et al.*,[9] adapted from Taylor[36] and Crow *et al.*.[33]

Initial measurements using our UV spectrometer focussed on the unperturbed $2_0^2 4_0^1$ band, previously studied by Motsche *et al.*.[32] A number of spectra were recorded, each acquired in $\approx 30\,GHz$ samples due to the scanning range of the near-infrared diode laser. The spectra were all recorded at pressures of 700 mTorr of formaldehyde and pieced together by overlapping spectral features or using the absolute line position, measured using a wavemeter. Figure 3.7 shows a sample spectrum (top). Another region spanning the range of ($30\,708\,cm^{-1}$ to $30\,716\,cm^{-1}$) is published in Crow *et al.*[33] Also shown in Figure 3.7 is a PGOPHER simulation of the same spectral region (middle panel), and the

data of Smith *et al.* (bottom panel). The PGOPHER simulation shows the unbroadened rotational lines in red and the same lines convoluted with a Gaussian function with the thermal Doppler width in black.[9,33,48] There is a very high level of agreement between the simulation and the results recorded here, especially remarkable in light of the instrument bandwidth used by Smith *et al.* to determine the rotational constants. Motsch *et al.*[32] also found good agreement with the work of Smith *et al.*, slightly refining the rotational constants to generate a better fit. Tatum Ernest *et al.*[35] produced a similar figure, reproduced in Figure 3.8, to compare their work with Smith *et al.*, Motsch *et al.* and the other spectral region published by Crow *et al.*, using the spectrometer described in this thesis. This figure further highlights the agreement between the work of Smith *et al.* and the true Doppler-limited lines recorded with our spectrometer and the instrument of Motsch *et al.*[9,32,33,35] It should be noted that simulations of this spectral region using PGOPHER and the rotational constants of Smith *et al.* required convolution with Doppler widths much broader than the sum of the thermal and quoted instrumental bandwidth ($0.16\,\mathrm{cm}^{-1}$) to achieve qualitative agreement between the results of Tatum Ernest *et al.* and PGOPHER. This suggests that their quoted bandwidth is overly optimistic, probably as a result of how the bandwidth has been determined. Tatum Ernest *et al.* state that the bandwidth was determined from a wavemeter, however the type of wavemeter is not discussed, it is therefore difficult to determine exactly how the wavemeter has been used to record a bandwidth and thus the reliability of the quoted value of their instrument.

The narrow bandwidth of this spectrometer, ≈ 10 MHz, allows sub-Doppler resolution of the rotational lines. To illustrate this, a single rotational transition, the isolated line at $\approx 30\,635\,\mathrm{cm}^{-1}$, is shown in Figure 3.9. This line is the ${}^{p}Q_{1,7}(8)$ transition. The data was fitted to a Gaussian using OriginPro; the returned full width half maximum of 2.05 ± 0.01 GHz is in excellent agreement with the predicted thermal Gaussian width of 2.06 GHz at room temperature, thereby confirming there is negligible instrumental broadening with this spectrometer.

Measurements of other spectral regions within the $2_0^2 4_0^1$ band were in very good agreement with the simulations from PGOPHER; in addition to this, absolute absorption cross sections were determined for a number of isolated rotational lines. These were determined

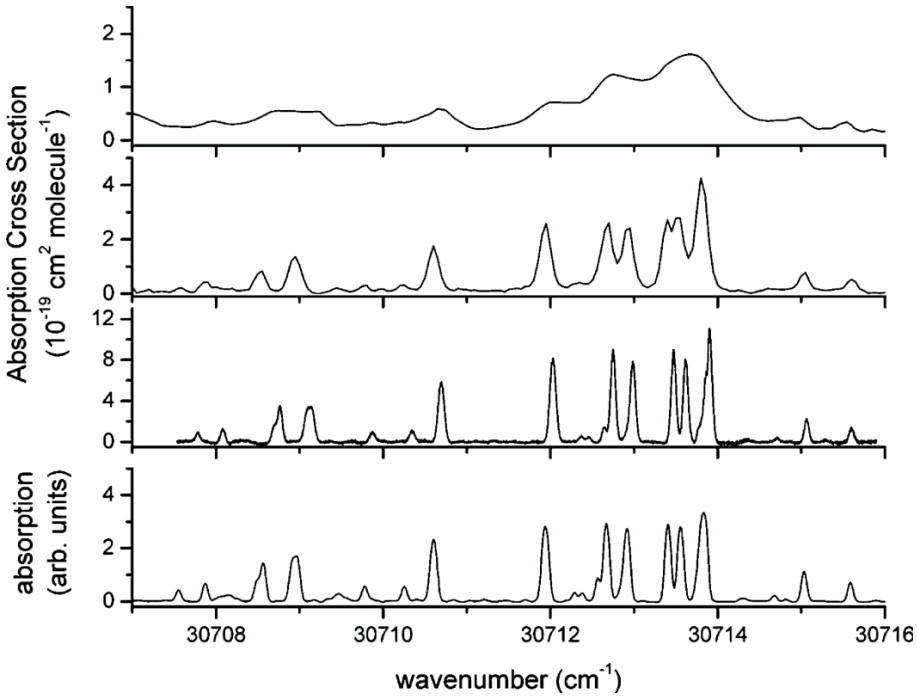

Figure 3.8: Comparison of the four most recent high-resolution UV spectra recorded on the $\tilde{A} - \tilde{X}\ 2_0^2 4_0^1$ transition, reproduced from Tatum Ernest *et al.*,[35] showing (from top to bottom) the results of Smith *et al.*,[9] Tatum Ernest, this spectrometer (published in Crow *et al.*),[33] and Motsch *et al.*[32].

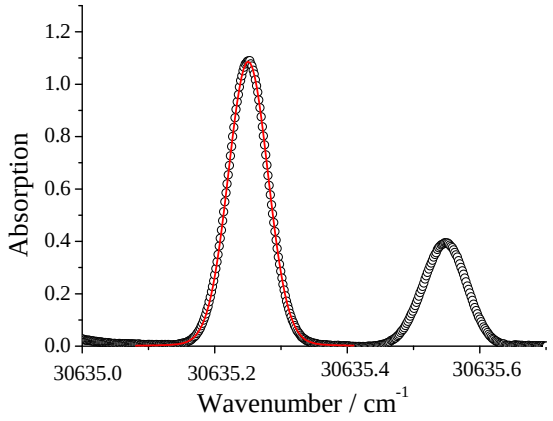

Figure 3.9: Example spectra showing Gaussian fitted to the ${}^pQ_{1,7}(8)$ transition at $30\,635.3\,\mathrm{cm}^{-1}$ with a FWHM $= 2.05 \pm 0.01$ GHz.

using the Beer-Lambert Law:

$$I_t = I_0 \exp(-\sigma_p[\mathrm{CH_2O}]l), \tag{3.22}$$

The light intensity transmitted through a sample, I_t, depends upon the incident light intensity, I_0; the concentration of the absorbing species, [CH_2O]; the sample length, l; and the probability of absorbing a photon, i.e. the absorption cross section, σ_p. The absorption cross sections have been measured using data such as that shown in Figure 3.10. In this data set, the ${}^{P}Q_{2,12}(13)$ transition was recorded at a number of pressures, and the absorption cross section was determined from a linear plot of absorbance *versus* number density using a rearranged form of the Beer-Lambert Law:

$$absorbance = -\ln\left(\frac{I}{I_0}\right) = \sigma_p[\mathrm{CH_2O}]l. \tag{3.23}$$

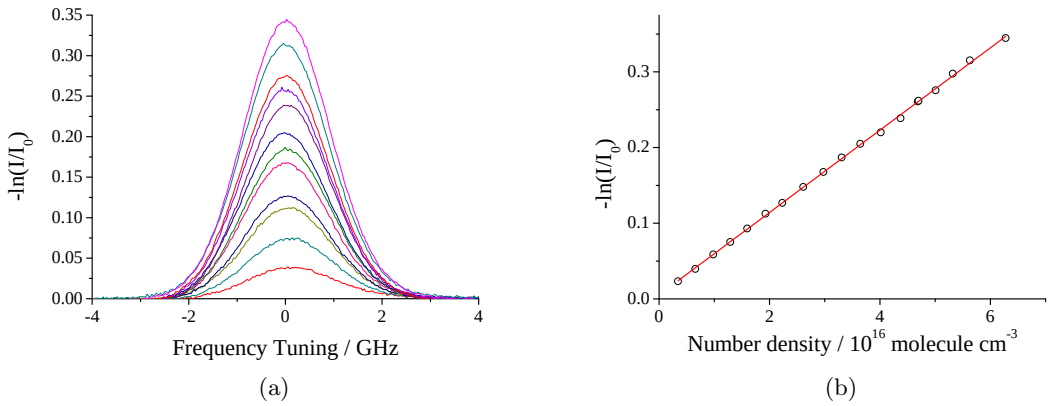

Figure 3.10: Example data used to determine the absorption cross section for the ${}^{P}Q_{2,12}(13)$ transition. (a) ${}^{P}Q_{2,12}(13)$ transition recorded over a range of pressures from 0.1 to 2 Torr. (b) The variation of absorption with number density, used to determine the absorption cross section.

The line positions, line strengths and the absorption cross sections determined for a number of transitions are given in Table 3.5 along with their simulated values from PGOPHER. It should be noted that the absorption cross sections determined with our spectrometer are all within 13% of the PGOPHER simulation, suggesting that the transition dipole moment obtained in this work agrees with that returned from the measurements of Smith *et al.*, 0.032 D. Conversely, Tatum Ernest *et al.* suggest a remarkably large change to the transition dipole moment, to give 0.026 D, to better fit their data.

Table 3.3: Measured and predicted peak absorption cross sections for a range of rotational lines in the $\tilde{A}\ ^1A_2 - \tilde{X}\ ^1A_1\ 2_0^2 4_0^1$ band. Taken in collaboration with Taylor[36] and published by Crow *et al.*.[33]

		$\sigma / \times 10^{-19}$ cm^{2}molecule^{-1}	
Transition	Wavenumber / cm^{-1}	Measured	PGOPHER[48]
$^pQ_{5,9}(14)/^pQ_{5,10}(14)$	30540.28	3.15 ± 0.17	2.81
$^pQ_{2,12}(13)$	30598.20	1.09 ± 0.06	1.07
$^rR_{3,23}(26)$	30634.98	0.18 ± 0.01	0.16
$^pQ_{1,7}(8)$	30635.31	10.1 ± 0.51	8.87
$^pR_{1,20}(20)/^pR_{2,13}(14)/^pR_{2,7}(9)$	30635.58	3.65 ± 0.18	3.39
$^rQ_{1,12}(13)$	30644.82	5.46 ± 0.29	5.36
$^rQ_{5,4}(8)/^rQ_{5,3}(8)$	30715.06	2.29 ± 0.12	2.32
$^rR_{5,11}(16)/^rR_{5,12}(16)$	30716.44	2.10 ± 0.11	2.07

Further work by Taylor and published by Crow *et al.* on the $2_0^2 4_0^1$ vibrational band utilised the high-resolution of the spectrometer described in this thesis to record the effects of pressure broadening of He, Ne, Ar and Kr and the diatomics O_2 and N_2 and quadrupolar molecule CO_2. In those studies, pressure broadening parameters of the order of MHz Torr^{-1} were measured and agree well with other studies, giving confidence to the values determined for the frequency scale and bandwidth.[33,36]

Since there is negligible instrumental broadening associated with our source, it is possible to measure more significant contributions to the lineshape arising from pressure effects, and it should also be possible to measure the effect of the finite excited state lifetime on the linewidth. Whilst the latter effect is not observable on the current vibronic band, rotational transitions in vibronic bands occurring at higher energies are expected to exhibit broadening due to predissociation, for reasons now discussed.

3.7 $\tilde{A}\ ^1A_2 - \tilde{X}\ ^1A_1\ 2_0^2 4_0^3$ Band

The $\tilde{A} - \tilde{X}$ transition involves excitation to the $S_1(^1A_2)$ state which may decay *via* two channels, given by equations 3.1 and 3.2.[49] In addition, immediately following excitation the molecule may fluoresce back to the ground state, undergo internal conversion to a vibrationally excited level of the $S_0(^1A_1)$ ground state, or undergo intersystem crossing to the $T_1(^3A_2)$ state. The latter pathway, intersystem crossing to T_1, exclusively produces the radical products, H + HCO, whereas internal conversion to S_0 produces either the

radical or molecular products, provided that there is sufficient energy to produce both products, $E_{\text{photon}} > 30328.5$ cm^{-1} or $\lambda < 329.7$ nm.[11] The potential energy surfaces, along with the $2_0^2 4_0^3$ vibrational level, are illustrated in Figure 3.11.[12] There is a barrier to photodissociation on the T_1 surface which is 1920 cm^{-1} above the H + HCO product asymptote,[50] and below this barrier the dissociation process proceeds predominantly *via* internal conversion to S_0. At energies close to or just above this barrier, such as for the $2_0^2 4_0^3$ and $2_0^3 4_0^3$ levels accessed in this work, intersystem crossing and internal conversion will both contribute, though internal conversion is still the most significant. At energies greater than the barrier, intersystem crossing becomes greater and dissociation *via* the T_1 state begins to dominate.[51]

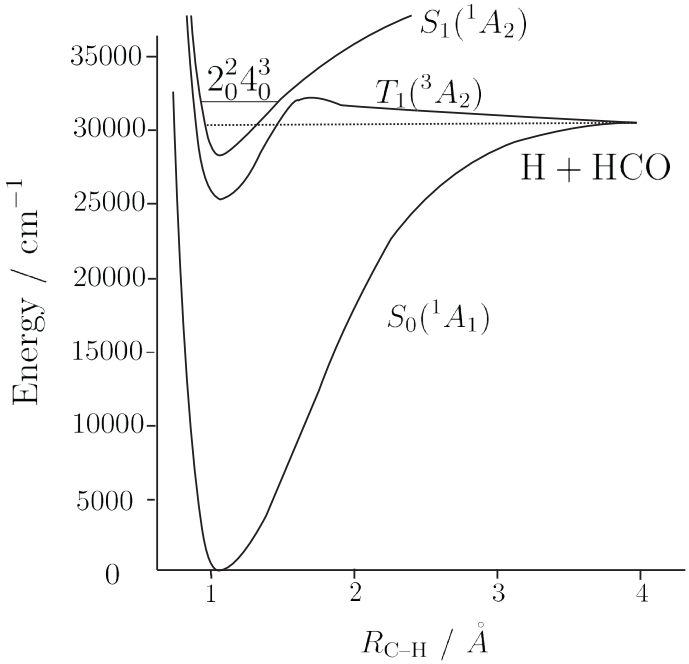

Figure 3.11: The potential energy curves for formaldehyde with the $2_0^2 4_0^3$ vibronic level indicated, reproduced from Terentis *et al.*[12]

The Franck-Condon factors which govern internal conversion from S_1 to S_0 are much larger for S_1 energy levels which involve the C–O stretch, ν_2, and out of plane bend, ν_4, than energy levels involving other vibrational modes since the large displacement from the equilibrium position which occurs with these vibrational modes enhances the overlap.[52] Hence, internal conversion for the $2_0^n 4_0^1$ and $2_0^n 4_0^3$ vibronic bands is expected to be much

faster than for other vibronic bands accessing states of comparable energy, resulting in shorter excited state lifetimes and potentially an observable lifetime broadening of the spectral linewidth.

Within error, the $2_0^2 4_0^1$ vibronic band displays no lifetime broadening. A Gaussian width equivalent to the calculated Doppler width is measured (see Figure 3.8). Lamb-dip spectroscopy would give a better measurement of the excited state lifetime, but would require high laser powers in order to saturate the transition, which are not achievable with our spectrometer.[53] However, by accessing shorter wavelengths it should be possible to probe pre-dissociated states in the $2_0^2 4_0^3$ band and to use the sub-Doppler resolution of our spectrometer to determine the lifetimes of excited states. This is a particularly interesting application as absorption of an ultraviolet photon typically occurs to an electronic state possessing a fast decay process that can compete with fluorescence, making it difficult to probe *via* some states by laser-induced fluorescence.

In order to access the shorter wavelength regions and measure spectra for the $2_0^2 4_0^3$ band, the near-infrared ECDL was replaced with a 785 nm diode laser (Sanyo DL-7140-001S) which, combined with the fixed-frequency 532 nm laser, produced 316 nm radiation. This new spectrometer produced 2.8 μW of tunable UV radiation, which corresponds to 46% of the theoretical maximum, calculated as discussed above. Initial measurements focused on the 31548–31562 cm^{-1} region, where the individual spectra (over a $1\,\mathrm{cm}^{-1}$ range) were pieced together in the manner described above for $2_0^2 4_0^1$ band. The spectra recorded in this way are shown in Figure 3.12 along with the PGOPHER simulation based on the constants of Smith *et al.*.[9] In contrast to the $2_0^2 4_0^1$ band data, the simulation is not a very good match, as might be expected for a pre-dissociated excited state, though the simulation and the recorded spectrum share some common features, such as the strong absorption peak at $31\,554\,\mathrm{cm}^{-1}$. In order to compare with the measurements of Smith *et al.* the same wavelength region was convoluted with a Voigt function with a Gaussian width of $0.2\,\mathrm{cm}^{-1}$ and a Lorentzian width of $0.5\,\mathrm{cm}^{-1}$, the widths quoted by Smith *et al.* to best account for Doppler broadening and instrumental broadening in their study. The resulting spectrum and the data of Smith *et al.* are both shown in Figure 3.13; comparison of this small spectral region suggests that this spectrum agrees qualitatively

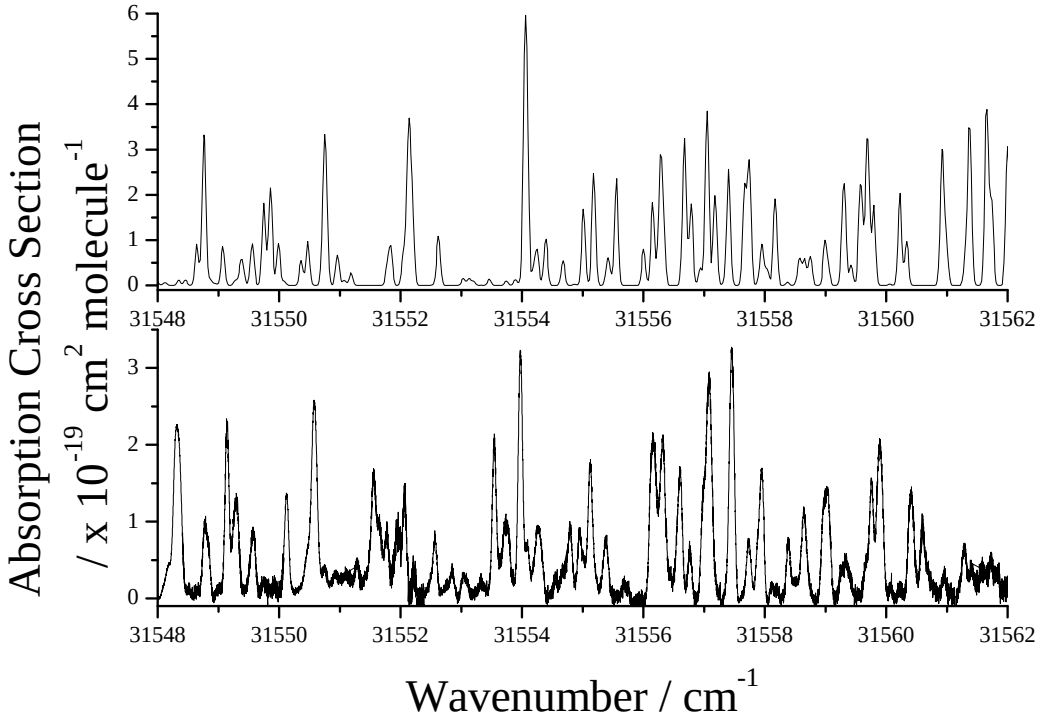

Figure 3.12: Comparison between the real and simulated spectra showing: Top, the PGOPHER simulation using the rotational constants of Smith *et al.* and Bottom, the spectrum recorded using this spectrometer.[9,48]

with the results of Smith *et al.*.[9]

3.7.1 Refining the Rotational Constants

The advantage of a spectrometer based upon a tunable dye laser, such as that used by Smith *et al.* and Tatum Ernest *et al.* is the broad spectral region over which it is possible to scan, even if dye lasers do not possess the sub-Doppler resolution of our spectrometer. Scanning over the entire vibronic band allows the entire band to be fitted to return the rotational constants, whereas our spectrometer is limited by the relatively small range of operating frequencies of the near-infrared diode laser. Therefore, in order to assign rotational transitions, approximately 50 small region scans were overlapped to produce a continuous spectrum over a range of $25\,\mathrm{cm}^{-1}$, as shown in Figure 3.14; which was then used to optimise the rotational constants in PGOPHER. The refined rotational constants

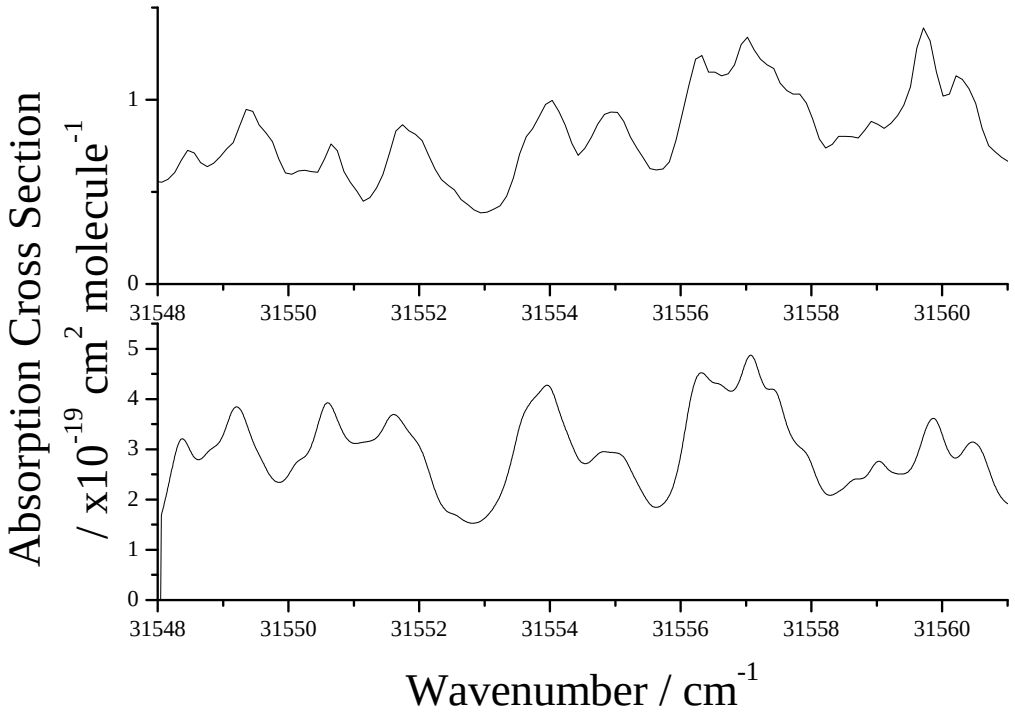

Figure 3.13: Comparison between Top: Smith *et al.* and Bottom: the data recorded with this spectrometer and convolved with a Voigt function with a Gaussian width of $0.2\,\mathrm{cm}^{-1}$ and a Lorentzian width of $0.5\,\mathrm{cm}^{-1}$ to match the quoted spectral bandwidth of Smith *et al.*.[9]

are given in Table 3.4 along with the values of Smith *et al.*[9]

Table 3.4: Rotational constants from the literature and determined in this work from the $2_0^2 4_0^3$ band in Figure 3.14.

Rotational Constants / cm^{-1}	Literature[9]	This work
A	7.9559	7.9863
B	1.10015	1.09875
C	1.00458	1.00318

Using the rotational constants in Table 3.4, an improved simulation of the rotational structure of the $2_0^2 4_0^3$ band was obtained, and is shown in Figure 3.15. These new rotational constants produce a markedly improved spectrum when compared with the Smith *et al.* constants, though could be optimised further. As discussed above, ideally the entire $2_0^2 4_0^3$

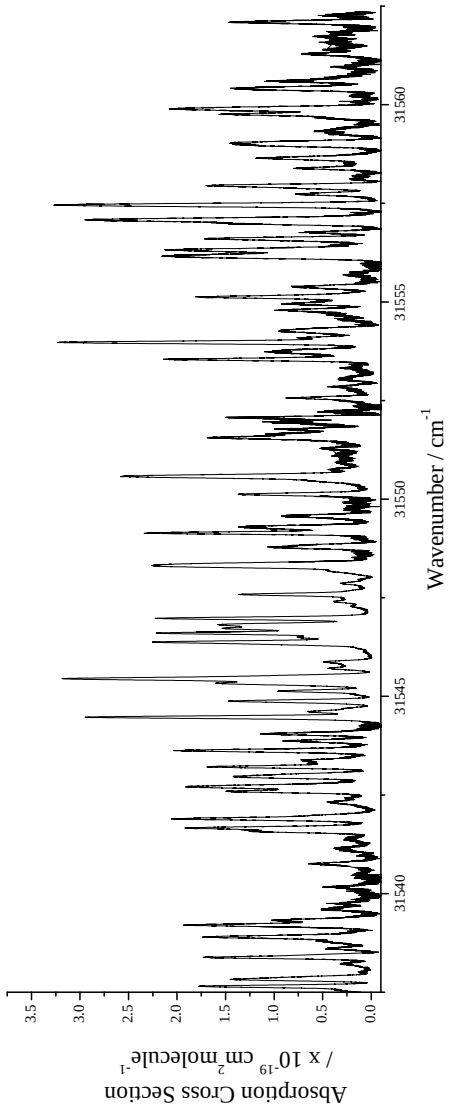

Figure 3.14: Recorded spectrum of the $2_0^2 4_0^3$ band used to refine the rotational constants. The spectrum is pieced together by overlapping multiple scans.

band would be measured, but the mode-hop-free scanning range available and wavelengths accessible to the near-infrared diode laser make this task challenging, and was not the goal when building our spectrometer. However, the improved spectrum is sufficient to allow confident assignment of some rotational transitions, especially the stronger transitions. Tatum Ernest *et al.* attempted to refine the spectrum of the $2_0^2 4_0^3$ band, by varying the transition dipole moment, and found that even after revision this band demonstrated the worst agreement between the simulated and recorded spectrum of all bands studied.[35] As before with the $2_0^2 4_0^1$ band, absorption cross sections were determine for some isolated rotational lines in the $2_0^2 4_0^3$ band, and are given in Table 3.5 along with the peak absorption cross sections predicted by PGOPHER. Similar to the $2_0^2 4_0^1$ band, the absorption cross sections determined with our spectrometer are all within 10% of those predicted by the PGOPHER simulation, indicating that this work agrees with the transition dipole moment returned from the measurements of Smith *et al.*, contrary to the studies of Tatum Ernest *et al.*.[9,35]

Table 3.5: Measured and predicted peak absorption cross sections for a range of rotational lines in the $\tilde{A}\ ^1A_2 - \tilde{X}\ ^1A_1\ 2_0^2 4_0^3$ band.

	Wavenumber	$\sigma / \times 10^{-19}$ cm^{2}molecule^{-1}	
Transition	/ cm^{-1}	Measured	PGOPHER[48]
$^rR_{1,8}(9)/^rR_{2,15}(16)$	31553.7	2.89 ± 0.02	2.74
$^rQ_{1,7}(7)$	31544.1	2.92 ± 0.05	2.79
$^rR_{0,3}(3)$	31544.33	1.06 ± 0.04	0.97
$^rQ_{1,5}(6)/^rR_{0,9}(9)/^rR_{3,18}(20)/^rR_{2,15}(17)$	31542.51	3.12 ± 0.01	3.04

Once the spectrum had been assigned, it was possible to use some of the isolated absorption features to determine linewidths. As discussed in Chapter 1, the lifetime of the excited state should contribute a Lorentzian component to the lineshape, hence the line profile should be described by a Voigt profile with a Gaussian FWHM fixed at the thermal value of 2.12 GHz. It is especially important to keep the pressures low in these measurements since formaldehyde has a rather large self broadening parameter, $\approx 20 \pm 0.5$ MHz Torr^{-1} in the $2_0^2 4_0^1$ band.[33]

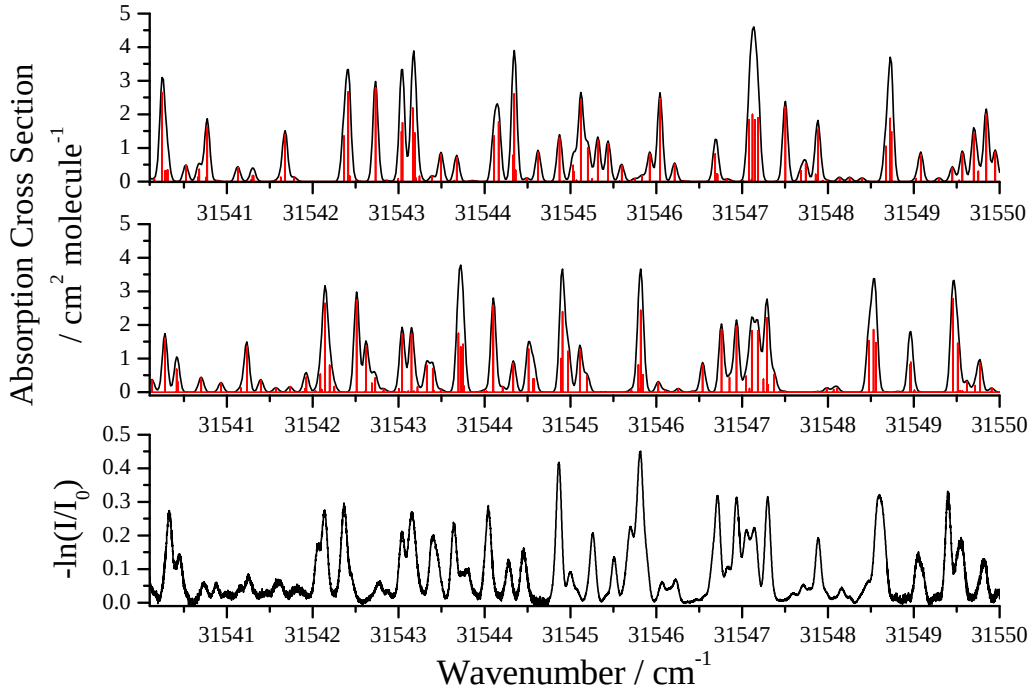

Figure 3.15: Comparison of PGOPHER simulation of the region shown in Figure 3.12 using: Top, the rotational constants of Smith *et al.*; Middle, rotational constants determined from Figure 3.14 and given in Table 3.4; and Bottom, the data recorded with this UV spectrometer.

3.7.2 Effects of Predissociation

An example spectrum recorded at a pressure of 387 mTorr is shown in Figure 3.16, alongside the PGOPHER simulation and the rotational assignment. The rotational lines were fitted using OrginPro and the returned Lorentzian FWHM for the $^rR_{0,3}(3)$ line shown in Figure 3.16 is 0.139±0.029 GHz. The stated error was determined from twice the standard deviation between 25 repeat measurements recorded on the rotational line over a series of days and on different formaldehyde samples. The $^rQ_{1,7}(7)$ has not been used since there is a small transition at the base of the absorption and the Lorentzian profiles differ from Gaussian profiles predominantly at the edges of the profile, as the profile approaches the base line (illustrated in Figure 1.8 in Chapter 1), thus the FWHM of this transition could not be confidently determined.

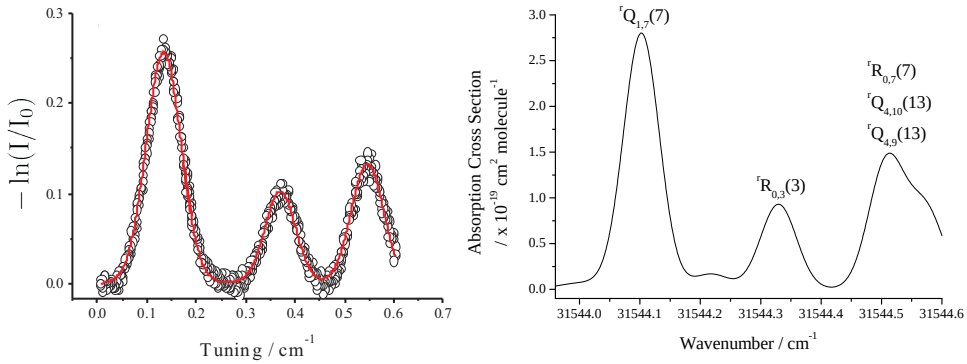

(a) Example spectra (b) PGOPHER simulation

Figure 3.16: Comparison of (a) the spectra recorded at a pressure of 390 mTorr and (b) the PGOPHER simulation using the refined rotational constants. In (a) the red line illustrates the fitted Voigt and the line assignments are given in (b).

A number of isolated lines were recorded in the same manner as for the ${}^{r}R_{0,3}(3)$ transition. The returned Lorentzian linewidths are given in Table 3.6, along with the corresponding lifetime of the excited state. The notation for the excited state is $J(K'_a, K'_c)$, where, the ${}^{r}R_{0,3}(3)$ transition, for example, involves excitation to the $J' = 4$, $K'_a = 1$, $K'_c = 4$ excited state rotational level. The lifetime, τ, was determined from the Lorentzian width, $\delta\tilde{\nu}$, using:[54]

$$\tau = \frac{1}{2\pi c \delta\tilde{\nu}}. \tag{3.24}$$

Table 3.6: Transitions measured and the calculated lifetime for excited state.

Transition ${}^{\Delta K}\Delta J_{K''_a,K''_c}(J'')$	Upper State $J'(K'_a, K'_c)$	Upper State Energy / cm^{-1}	Lorentzian FWHM / GHz	Upper State Lifetime/ ns
${}^{r}R_{0,3}(3)$	4(1,4)	31544.4	0.139 ± 0.029	1.14 ± 0.20
${}^{p}Q_{1,5}(6)$	6(0,6)	31575.5	0.109 ± 0.023	1.46 ± 0.25
${}^{p}Q_{1,9}(10)$	10(0,10)	31646.5	0.141 ± 0.030	1.13 ± 0.20
${}^{p}Q_{1,10}(11)$	11(0,11)	31669.4	0.207 ± 0.043	0.77 ± 0.13
${}^{r}Q_{1,12}(12)$	12(2,11)	31722.8	0.210 ± 0.044	0.76 ± 0.13
${}^{r}Q_{3,9}(12)$	12(4,8)	31806.5	0.210 ± 0.044	0.76 ± 0.13
${}^{r}Q_{2,12}(13)$	13(3,11)	31785.1	0.166 ± 0.035	0.96 ± 0.17
${}^{r}R_{3,13}(15)$	16(4,12)	31928.3	0.216 ± 0.045	0.74 ± 0.13

There appears to be only a very modest decrease in the upper-state lifetime with in-

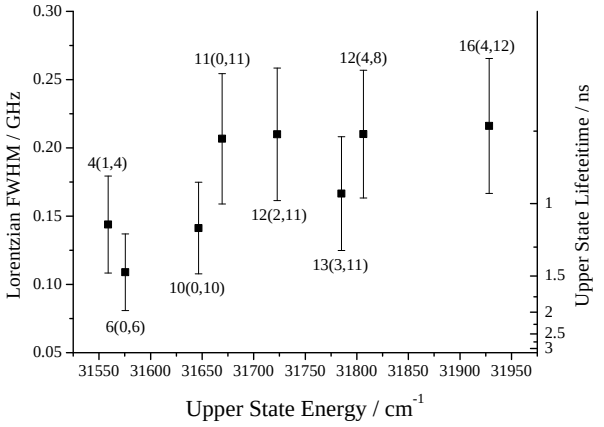

Figure 3.17: The variation in the Lorentzian FWHM with the upper state energy.

creasing rotational energy, illustrated in Figure 3.17, which is in agreement with studies in the literature on the $2_0^2 4_0^1$ band,[55–58] though there is not enough data to discern a dependence of the lifetime upon J, K_a or K_c in this work. Henke *et al.*[57] suggest that the shorter lifetimes observed for increasing rotation is the result of a widening difference between the moments of inertia of the two electronic states, which leads to an increased Franck-Condon factor, leading to faster internal conversion. The range of lifetimes observed with this spectrometer are all below the lifetime of 5.8 ns determined for the $2_0^2 4_0^3$ band by Miller *et al.*,[59] though the value of Miller *et al.* is averaged over the whole vibrational band and we would require a large number of rotational states to be measured with our spectrometer before a definitive comparison could be drawn. Miller *et al.* reported fluorescence measurements using a D_2 flash lamp to excite 4 Torr samples of formaldehyde and recording the entire band and thus would require a large number of rotational states to be measured before a definitive comparison could be drawn. In conclusion: the $2_0^2 4_0^3$ band does exhibit predissociation effects, but not to a very large degree, though measurements of the associated spectral line broadening are observable using our spectrometer due to its narrow instrumental bandwidth.

3.8 $\tilde{A}\ ^1A_2 - \tilde{X}\ ^1A_1\ 2_0^3 4_0^3$ Band

The $\tilde{A}\ ^1A_2 - \tilde{X}\ ^1A_1\ 2_0^3 4_0^3$ band is predicted to be more strongly predissociated than the $2_0^2 4_0^3$ band due to an increased amount of vibrational energy aiding in the coupling of the surfaces. In addition to this, the $\tilde{A}\ ^1A_2 - \tilde{X}\ ^1A_1\ 2_0^3 4_0^3$ band occurs very close to the $\tilde{A} - \tilde{X}$ electronic transition of OH, one of the most important atmospheric molecules and the focus of many photodissociation and collision dynamics studies, as will be discussed in the next chapter. UV absorption by OH occurs *via* a strong electronic transition around 308 nm. From the CH_2O data shown in Figure 3.5 and enlarged in Figure 3.19, this should occur near the tail end of the $2_0^3 4_0^3$ vibronic band of formaldehyde. The incorporation of a new near-infrared laser into our spectrometer to produce tunable 308 nm radiation may therefore be optimised using formaldehyde before being applied to OH spectroscopy.

In order to generate 308 nm radiation, the near-infrared laser diode was replaced with a 730 nm diode (Opnext, HL7301MG), which generated 2.8 μW of UV radiation using the same experimental set up as described above. Unfortunately, laser diodes are difficult to manufacture at 730 nm since it is difficult to manufacture semiconductors with the correct band-gap; therefore the wavelengths and the mode-hop-free tuning range available to this laser diode were limited. However, some regions of the $2_0^3 4_0^3$ transition displaying reasonably strong absorption features (1 - 9×10^{-20} $cm^2 molecule^{-1}$), were accessible. As before with the $2_0^2 4_0^3$ band, it was expected that predissociation of the excited state would have resulted in a poor simulation of $2_0^3 4_0^3$ band. Thus, the rotational constants for the $2_0^3 4_0^3$ band would require optimization in order to improved the simulation. Similar to the method employed above, a selection of spectra were recorded and compared with the results of Smith *et al.* and PGOPHER, one such region is shown in Figure 3.18.

Unfortunately, the spectrometer operated in the tail region of the $2_0^3 4_0^3$ vibronic band, illustrated in Figure 3.19, since the infrared diode was chosen to allow access to the strong OH electronic absorptions. Being limited to measuring the transitions of the tail of the vibronic band, there were very few strong or isolated absorption features to assign and, as can be seen in Figure 3.18c, the spectrum is quite congested. Attempts at fitting Voigt profiles to possible isolated lines did not produce meaningful results. In addition to this, the wavelengths accessible using the laser diode did not allow a large spectral region to be

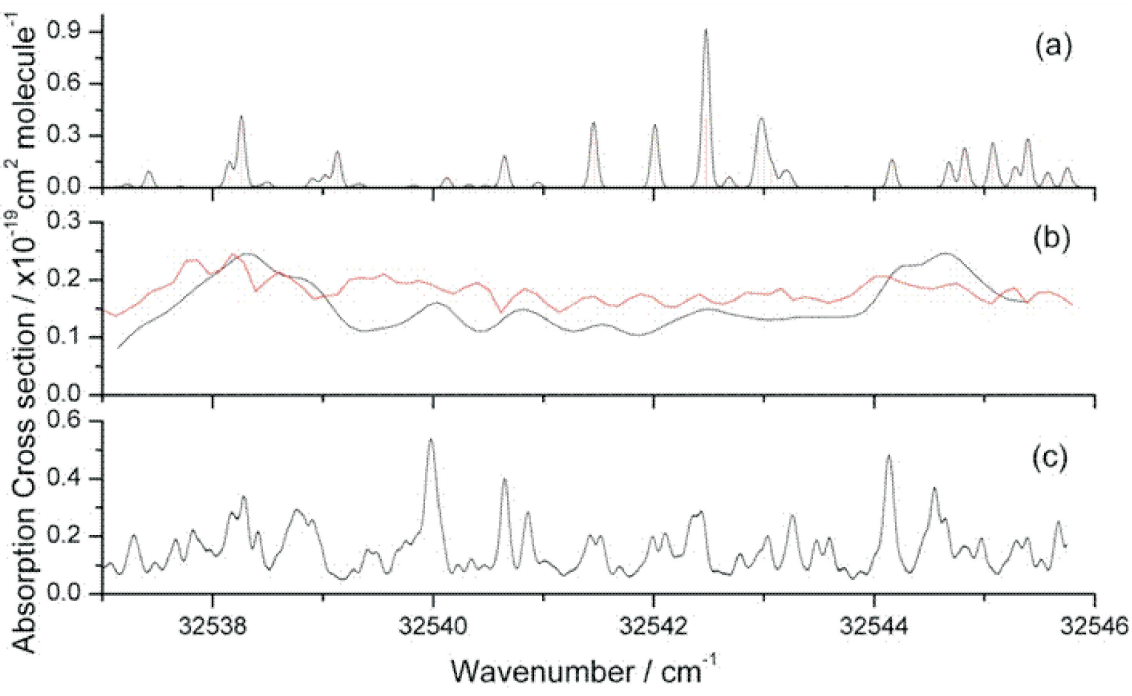

Figure 3.18: Example spectrum of the $2_0^3 4_0^3$ vibrational band showing: (a) PGOPHER simulation of the band using the constants of Smith *et al.* and showing the thermal Doppler broadening; (b) The data of Smith *et al.* (in black) and the PGOPHER simulation (in red) using their experimental broadening parameters; (c) spectrum recorded with the UV spectrometer in this work.[9]

acquired, unlike for the $2_0^2 4_0^3$ band. The work of Tatum Ernest *et al.* could not optimise the rotational constants of this vibronic band sufficiently to allow confident assignment of any rotational features, even with the entire band at their disposal.[35] However, absorption features in this band were used in the calibration of the OH spectrometer developed in the next chapter, as will be discussed therein.

3.9 Conclusion

This chapter has detailed the development of an ultraviolet spectrometer using sum-frequency generation to mix two continuous-wave lasers. The application of the spectrometer to absorption spectroscopy on the $\tilde{A} - \tilde{X}$ electronic transition of formaldehyde has been studied on three vibronic bands, $2_0^2 4_0^1$, $2_0^2 4_0^3$ and $2_0^3 4_0^3$. For the $2_0^2 4_0^1$ band the sub-Doppler resolution of this spectrometer recorded true thermal line shapes and allowed

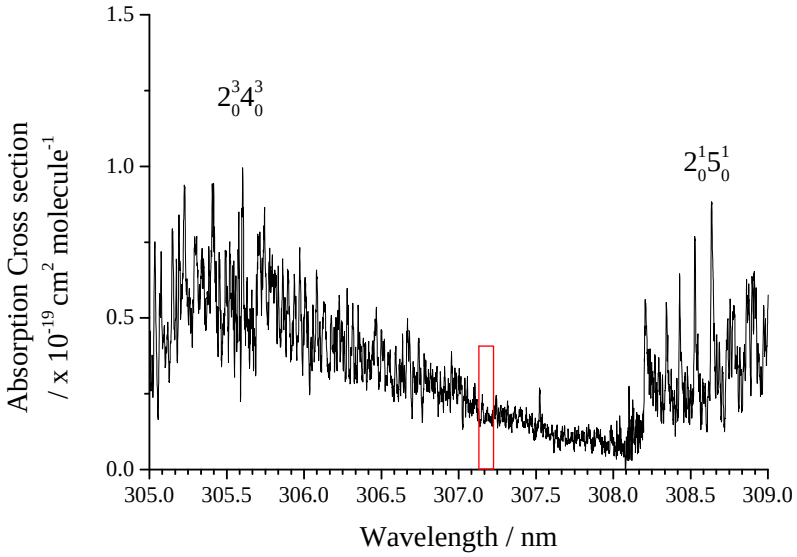

Figure 3.19: The $2_0^3 4_0^3$ vibrational band, reproduced from Smith *et al.* with the spectral region of Figure 3.18 indicated.[9]

determination of absolute absorption cross sections, which compared very favourably with literature results.[9,32] For the $2_0^2 4_0^3$ band the rotational constants were optimised and absolute absorption cross sections were determined. In addition, the lifetimes of a small selection of excited states were measured, and all were determined to be in the 0.7 – 1.5 ns range, in reasonable agreement with the literature. The $2_0^3 4_0^3$ band was not assignable and recent work by Tatum Ernest *et al.* did not allow rotational constants to be fitted either.[35] However, regions of the spectra will be used in the next chapter.

It is emphasised that for the two major bands studied in this work, we consistently measure absorption cross sections that are within 13% of simulations based upon the work of Smith *et al.*. This is contrary to the more recent studies by Tatum Ernest *et al.*, but it is noted that there are several questions regarding the analysis of their data. Hence, we are confident in our experimental method and in the spectrometer we have developed. The spectrometer will allow further studies of OH spectroscopy by utilising the mode-hop-free tuning range available to an external cavity diode laser, the details of which are the focus of the next chapter.

References

[1] D. Wuebbles, Earth-Science Reviews **57**, 177 (2002).

[2] C. Hak et al., Atmospheric Chemistry and Physics **5**, 2881 (2005).

[3] L. G. Anderson et al., Atmospheric Environment **30**, 2113 (1996).

[4] P. Carlier, H. Hannachi, and G. Mouvier, Atmospheric Environment (1967) **20**, 2079 (1986).

[5] K. Riedel, R. Weller, and O. Schrems, Physical Chemistry Chemical Physics **1**, 5523 (1999).

[6] D. Grosjean, R. D. Swanson, and C. Ellis, Science of The Total Environment **29**, 65 (1983).

[7] I. Williams, D. Revitt, and R. Hamilton, Science of The Total Environment **189-190**, 475 (1996).

[8] W. H. O. R. O. for Europe, *Air Quality Guidelines for Europe*, WHO Regional Publications: European series, World Health Organization, Regional Office for Europe, 2000.

[9] C. A. Smith, F. D. Pope, B. Cronin, C. B. Parkes, and A. J. Orr-Ewing, The Journal of Physical Chemistry A **110**, 11645 (2006).

[10] M. Dulligan, M. Tuchler, J. Zhang, A. Kolessov, and C. Wittig, Chemical Physics Letters **276**, 84 (1997).

[11] A. Terentis, Chemical Physics Letters **258**, 626 (1996).

[12] A. C. Terentis, S. E. Waugh, G. F. Metha, and S. H. Kable, The Journal of Chemical Physics **108**, 3187 (1998).

[13] G. D. Smith, L. T. Molina, and M. J. Molina, The Journal of Physical Chemistry A **106**, 1233 (2002).

[14] A. M. Holloway and R. P. Wayne, *Atmospheric Chemistry*, Royal Society of Chemistry, 2010.

[15] D. Jacob, *Introduction to Atmospheric Chemistry*, Princeton University Press, 2011.

[16] K. Chance et al., Geophysical Research Letters **27**, 3461 (2000).

[17] D. Grossmann, Journal of Geophysical Research **108** (2003).

[18] M. Hausmann, U. Brandenburger, T. Brauers, and H.-P. Dorn, Journal of Geophysical Research **102**, 16011 (1997).

[19] R. Sinreich, U. Frieß, T. Wagner, and U. Platt, Faraday Discussions **130**, 153 (2005).

[20] F. Wittrock et al., Geophysical Research Letters **33**, 1 (2006).

[21] R. D. McQuigg and J. G. Calvert, Journal of the American Chemical Society **91**, 1590 (1969).

[22] J. G. Calvert, J. A. Kerr, K. L. Demerjian, and R. D. McQuigg, Science (New York, N.Y.) **175**, 751 (1972).

[23] A. Bass, L. Glasgow, C. Miller, J. Jesson, and D. Filkin, Planetary and Space Science **28**, 675 (1980).

[24] P. W. Fairchild, N. L. Garland, W. E. Howard, and E. K. C. Lee, The Journal of Chemical Physics **73**, 3046 (1980).

[25] C. A. Cantrell, J. A. Davidson, A. H. McDaniel, R. E. Shetter, and J. G. Calvert, The Journal of Physical Chemistry **94**, 3902 (1990).

[26] J. D. Rogers, The Journal of Physical Chemistry **94**, 4011 (1990).

[27] R. Meller and G. K. Moortgat, Journal of Geophysical Research **105**, 7089 (2000).

[28] F. D. Pope et al., Faraday Discussions **130**, 59 (2005).

[29] F. D. Pope, C. A. Smith, M. N. R. Ashfold, and A. J. Orr-Ewing, Physical Chemistry Chemical Physics **7**, 79 (2005).

[30] D. T. Co, T. F. Hanisco, J. G. Anderson, and F. N. Keutsch, The Journal of Physical Chemistry A **109**, 10675 (2005).

[31] A. Gratien et al., The Journal of Physical Chemistry A **111**, 11506 (2007).

[32] M. Motsch et al., Journal of Molecular Spectroscopy **252**, 25 (2008).

[33] M. B. Crow et al., The Journal of Physical Chemistry A **113**, 6689 (2009).

[34] G. Dieke and G. Kistiakowsky, Physical Review **45**, 4 (1934).

[35] C. Tatum Ernest, D. Bauer, and A. J. Hynes, The Journal of Physical Chemistry A **116**, 5910 (2012).

[36] S. R. Taylor, *Diode Laser Based Studies of Transient Species*, PhD thesis, University of Oxford, 2009.

[37] R. W. Boyd, *Nonlinear Optics*, Elsevier, second edition, 2003.

[38] A. Hugi, R. Maulini, and J. Faist, Semiconductor Science and Technology **25**, 083001 (2010).

[39] D. Zhang, Optics Communications **184**, 485 (2000).

[40] G. D. Boyd, Journal of Applied Physics **39**, 3597 (1968).

[41] D. N. Nikogosyan, Applied Physics A Solids and Surfaces **52**, 359 (1991).

[42] V. L. Kasyutich, The European Physical Journal D **33**, 29 (2005).

[43] D. B. Oh, Optics Letters **20**, 100 (1995).

[44] G. Hancock and V. Kasyutich, Applied Physics B **79**, 383 (2004).

[45] R. Spence and W. Wild, Journal of the Chemical Society (Resumed) , 338 (1935).

[46] J. M. Hollas, *Modern Spectroscopy*, J. Wiley, 2004.

[47] D. J. Clouthier and D. a. Ramsay, Annual Review of Physical Chemistry **34**, 31 (1983).

[48] C. M. Western, PGOPHER, a Program for Simulating Rotational Structure.

[49] C. B. Moore and J. C. Weisshaar, Annual Review of Physical Chemistry **34**, 525 (1983).

[50] Y. Yamaguchi, S. S. Wesolowski, T. J. Van Huis, and H. F. Schaefer, The Journal of Chemical Physics **108**, 5281 (1998).

[51] E. S. Yeung, The Journal of Chemical Physics **60**, 2139 (1974).

[52] E. C. Apel and E. K. C. Lee, The Journal of Chemical Physics **84**, 1039 (1986).

[53] J. M. Brown and A. Carrington, *Rotational Spectroscopy of Diatomic Molecules*, Cambridge Molecular Science Series, Cambridge University Press, 2003.

[54] P. W. Atkins, *Physical Chemistry*, Internationa Student Edition, Oxford University Press, 1994.

[55] J. C. Weisshaar and C. B. Moore, The Journal of Chemical Physics **70**, 5135 (1979).

[56] W. E. Henke, The Journal of Chemical Physics **76**, 1327 (1982).

[57] W. E. Henke, The Journal of Chemical Physics **76**, 1335 (1982).

[58] H. Kato and M. Baba, Chemical Reviews **95**, 2311 (1995).

[59] R. G. Miller and E. K. C. Lee, The Journal of Chemical Physics **68**, 4448 (1978).

Chapter 4

High Resolution Ultraviolet Spectroscopy of OH

In the previous chapter, an ultraviolet spectrometer operating at 325, 316 and 308 nm was developed in order to probe rotational fine structure in the vibrational bands of the $\tilde{A} - \tilde{X}$ electronic band of formaldehyde. The performance of the spectrometer at 325 nm, using the external cavity diode laser (ECDL), was far superior to that of the stand-alone Fabry-Perot type diodes used to generate 316 and 308 nm due to the enhanced tunability provided by the external cavity. In light of this, this chapter explores the application of an ECDL to produce tunable radiation at 308 nm. The resulting spectrometer is first used to probe a continuous source of hydroxyl radicals by utilising cavity-enhanced absorption spectroscopy to determine the number of radicals generated in the flow cell, before measuring the pressure induced broadening of a rotational line by He, Ne, Ar and N_2 buffer gases. Wavelength modulation is also applied to determine the effects of noise reduction in the spectrometer.

Following this, the continuous-wave UV source is applied to detect nascent OH radicals generated in the 193 nm photodissociation of nitric acid, and the relaxation rate of the speed distribution is measured from the nascent line profiles of the OH radical.

4.1 Introduction

Hydroxyl radicals are a key constituent of the troposphere, taking part in many reaction pathways. Most compounds present in the troposphere, such as CH_4 and other volatile organic compounds (VOCs), are relatively stable species which are relatively unreactive at the ambient temperature. These species are often greenhouse gases or deplete atmospheric

ozone following their own degradation in the upper troposphere/lower atmosphere, and it is the hydroxyl radical which oxidises these compounds through radical-chain pathways and thus cleans the troposphere. For this reason OH is often known as an atmospheric detergent.[1,2]

The hydroxyl radical is itself created in the atmosphere by the photolysis of ozone followed by reaction of the photo-generated $O(^1D)$ with small amounts of water.

$$O_3 + h\nu \rightarrow O(^1D) + O_2 \tag{4.1}$$

$$O(^1D) + H_2O \rightarrow 2\,OH \tag{4.2}$$

Once generated, the hydroxyl radical reacts with many species, some of which are shown in Figure 4.1. In an unpolluted environment, the OH reacts predominantly with CH_4 and CO.[1,2] The low concentrations of $O(^1D)$ and water vapour coupled with the high reactivity of the radical mean that the concentration of OH radicals is never very large, typically of the order of 10^6 molecules cm^{-3}, and the lifetime ranges from 10 ms in polluted air to 1 s in clean air.[2]

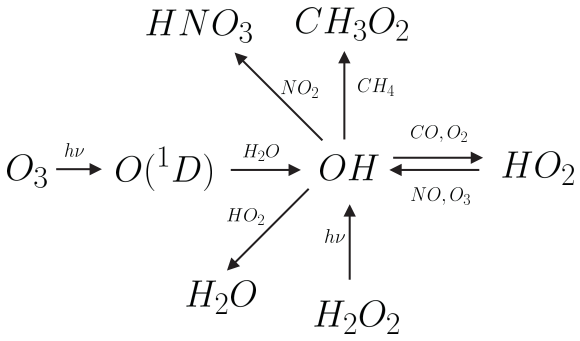

Figure 4.1: Some of the tropospheric process involving OH, adapted from *Atmospheric Chemistry.*[1]

The hydroxyl radical's involvement in the oxidation of pollutants has generated a large amount of interest in *in situ* measurements of its concentration, with the low concentration and short lifetime presenting significant technical challenges. Despite these challenges, many techniques have been applied to OH detection, including laser-induced fluorescence (LIF),[3] matrix isolation followed by electron spin resonance,[4] reaction of OH with ^{14}CO

and detection of the product,[5–7] chemical conversion to $H_2{}^{34}SO_4$ followed by mass spectrometry and differential optical absorption spectroscopy (DOAS).[2]

Laser-based detection methods are ideally suited to *in situ* measurements of gas phase species since they may provide nondestructive, portable, time resolved and species-specific detection, but there are problems. LIF generally requires a moderately high powered pulsed laser to excite the OH to a fluorescent state. However, this electronic transition can also dissociate ozone, generating more OH. This can be overcome by reducing the pressure to avoid the reaction in equation 4.2 in a technique known as laser-induced fluorescence spectroscopy at low pressure or fluorescence assay by gas expansion (FAGE) and is routinely employed with detection limits of the order of 10^5 molecules cm^{-3}. However FAGE is still based upon LIF and is therefore also highly sensitive to Raleigh scattering, Mie scattering and light scattering from the incident laser passing though the spectrometer and therefore requires very careful calibration.[2]

Absorption techniques are generally much less sensitive than LIF since LIF measures the number of photons reaching the detector, rather than relying on a difference measurement like absorption spectroscopy. Absorption spectroscopy records the difference between transmitted light intensity and incident light intensity and can be understood in terms of the Beer-Lambert Law, discussed in Chapter 3 and described by:

$$I_t = I_0 \exp(-\sigma_p[\mathrm{OH}]l) \tag{4.3}$$

for the case of OH as the absorbing species.

Differential optical absorption spectroscopy (DOAS) typically requires large path lengths, usually of the order of kilometres.[8,9] However, this leads to large amount of spatial averaging of the concentration. DOAS instruments have also been used in a multi-pass configuration, reflecting the incident light between two mirrors many times to increase the path-length, thus avoiding the large spatial averaging.[10] These instruments are portable and stable enough to be used in the field, despite the difficulty in their alignment and the large separation (20 m) between the two multi-pass mirrors.[11] These DOAS instruments typically use pulsed laser sources. These often have broadbandwidths and so analysis requires subtraction of all atmospheric species detected. This can become complex since the strong OH absorption at 308 nm is accompanied by absorption features arising from many

other atmospheric molecules such as CH_2O, SO_2 and some VOCs. A narrow-bandwidth source would avoid this problem by state-selecting an OH rotational line in the spectrum, ideally in a spectral window free from other absorbers. As demonstrated in the previous chapter, it is possible to extend the operating region of near-infrared diode lasers using sum frequency generation. In this chapter a purpose-built external-cavity diode laser using a 730 nm laser diode is incorporated into the spectrometer to allow spectroscopy to be carried out on OH samples generated both continuously using a mercury lamp and from the photolysis of nitric acid.

4.2 Experimental Set Up

As discussed in the previous chapter, the spectrometer combined the high power of a fixed frequency (532 nm) solid state laser with the tunability of a near-infrared ECDL using sum frequency generation. The same β-barium borate crystal as before was used as before and the refractive indices given in Table 4.1, and the frequency mixing parameters associated with these new wavelengths given in Table 4.2. The theoretical conversion efficiency was calculated to be $\gamma = 3.34 \times 10^{-4}\,\mathrm{W}^{-1}$.

Table 4.1: Values of the refractive indices in the crystal.

λ/nm	η_o	η_e
730	1.546	1.663
532	1.555	1.674
308	1.591	1.726

Table 4.2: The values used in the calculation of γ for the 308 nm spectrometer.

d_{eff}/pmV^{-1}	$\eta_{e,3}$	θ_m/rad	ρ/rad	B	h	γ/W^{-1}
1.470	1.669	0.670	0.0799	16.5	0.0433	3.34×10^{-4}

The experimental set up was identical to that used in the previous chapter, with the output from the fixed frequency 532.19 nm laser source combined with an external cavity diode laser (Toptica DL pro) with a 730 nm laser diode installed. The output of the near-infrared diode laser was monitored with a Fabry-Perot interferometer (Thorlabs

SA200-6A, 2 GHz free spectral range). As before, the two laser beams are overlapped and focused through the BBO crystal using a 10 cm focal-length lens. The generated 308 nm radiation is re-collimated and separated from the 532 nm and 730 nm radiation by passage through a filter (UG11). This produced 13 μW of UV from the 2 W of 532 nm radiation and 30 mW of 730 nm radiation focused through the crystal, which corresponds to 65% of the theoretical maximum.

The resulting 308 nm radiation was tuned by varying the angle of the grating in the ECDL; thus the spectrometer's scanning range was limited by the mode-hop-free tuning range of the near-infrared laser. In the previous chapter a Fabry-Perot 730 nm diode laser was used. Using an ECDL provides enhanced tunability and greater wavelength selection due to the grating. However, 730 nm diode lasers are difficult to manufacture due to problems in developing semiconductors with the required band-gap structures. Therefore, measurements were limited by the operating wavelengths of the near-infrared diode laser.

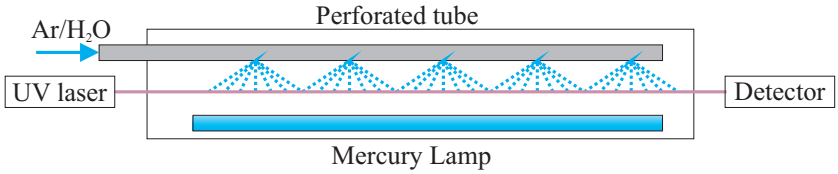

Figure 4.2: Experimental set up used to generate OH radicals.

Samples of OH were generated continuously by flowing 1 bar of Ar through H_2O with the resulting Ar/H_2O mixture entering a partially sealed glass cell opposite a 23 cm long mercury discharge lamp (PenRay LSP034), as shown in Figure 4.2. The mercury lamp dissociated water at 185 nm to produce a continuous supply of approximately 9×10^{11} molecules cm^{-3} of OH, as determined from cavity measurements discussed in detail below. At this concentration, with an OH peak absorption cross section, σ_p, of 1.67×10^{-16} cm^2 $molecule^{-1}$;[12] and a single pass path length, l, of 23 cm; the absorbance is $\approx 0.4\%$, based upon the Beer-Lambert Law (equation 4.3). This amount of absorption is often difficult to measure with high signal-to-noise ratio, and it was necessary to employ some form of noise reduction or signal enhancement, or both, to improve the measurement sensitivity.

4.3 OH Spectroscopy: A $^2\Sigma^+$-X $^2\Pi$ Transition

The absorption lines discussed in this work all lie within the $\nu = 0$ to $\nu = 0$ vibrational band of the A $^2\Sigma^+$ - X $^2\Pi$ electronic transition which occurs in the ultraviolet around 308 nm.

The ground state configuration of the hydroxyl radical is $(1s)^2(2s\sigma)^2(2p\sigma)^2(1p\pi)^3$,[13] and hence it has non-zero projection of orbital angular momentum along the molecular axis due to the occupation of a π orbital by a lone electron. Coupling between the orbital angular momentum and the electron spin results in spin-orbit splitting of the ground state into $^2\Pi_{3/2}$ and $^2\Pi_{1/2}$ states. Furthermore, the (non-zero) orbital angular momentum interacts with the rotation of the molecule, splitting each rotational energy level into two levels, a phenomenon known as Λ-doubling.[14] The Λ-doublets are differentiated by their parities, which refer to whether the wavefunction is symmetric, $+$, or antisymmetric, $-$, under reflection in the plane of rotation.[13] Finally, the electron spin, S, couples to the rotational angular momentum, N, so that the rotational energy levels are described by the total angular momentum quantum number, J, where $J = N \pm S$. Furthermore, $J = N + 1/2$ is called an F_1 level and $J = N - 1/2$ is called an F_2 level.

The excited state of the hydroxyl radical has no orbital angular momentum, so some of the coupling effects in the ground state are not present in the A state. However, the electron spin still couples to the rotation of the molecule, according to Hund's case (b),[14] and so the rotational energy levels are once again described by J, and the labels F_1 and F_2 again refer to $J = N + 1/2$ and $J = N - 1/2$, respectively. In the excited state the parity of the rotational level is given by $(-1)^N$.

The rotational fine structure observed within the A $^2\Sigma^+$ - X $^2\Pi$ (0,0) transition is governed by the normal spectroscopic selection rules: $\Delta J = 0, \pm 1$ and $\pm \leftrightarrow \pm$ but $\pm \nleftrightarrow \mp$. The resulting rotational lines are labelled using the notation $\Delta J_{F_{\rm upper}F_{\rm lower}}(N_{\rm lower})$, with transitions corresponding to $\Delta J = 0$ labelled Q and transitions corresponding to $\Delta J = +1$ and $\Delta J = -1$ labelled R and P respectively. A transition between the same F states usually uses just a single subscript, for example the $Q_{11}(2)$ is often simply labelled $Q_1(2)$. All of the above features are summarised in Figure 4.3, where the dashed lines beside rotational lines are the satellites (i.e. the $P_1(1)$ has the $P_{21}(1)$ indicated) and the energy

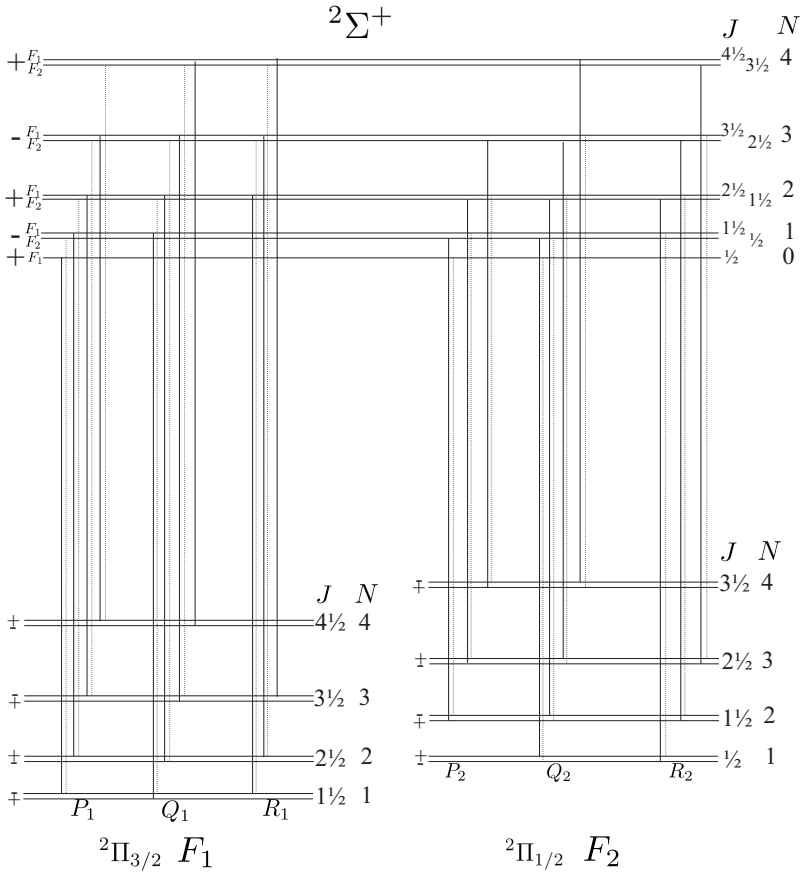

Figure 4.3: Energy level diagram showing the energy level splitting of the excited and ground states of OH. Some of the rotational transition are indicated with the $F_1 \leftrightarrow F_2$ satelllites shown as dashed lines. The Λ-doubling is greatly exaggerated.

difference between Λ-doublets is greatly exaggerated. [14]

4.4 Cavity-Enhanced Absorption Spectroscopy

As discussed above, direct absorption spectroscopy would result in an absorbance of ≈ 0.4%, which is difficult to see with the low signal to noise ratio associated with detecting low-power UV radiation. Therefore, it is necessary to either enhance the absorption signal or decrease the noise. Increasing the path length through an absorbing medium is one of the simpler methods of enhancing an absorption signal, and is the basis of cavity-enhanced absorption spectroscopy (CEAS). [15] Using highly reflective mirrors it is possible to effectively multi-pass laser radiation many times through the absorbing medium, and in practice a reflectivity, R, of greater than 99.99% ($R = 0.9999$) is possible in the visible

and near-infrared. Using a small cavity length of the order of $l = 50\,\text{cm}$, it is possible to achieve an effective path length on the order of kilometres. An adjusted form of the Beer-Lambert Law is used to account for the effective increase in path-length:

$$\frac{I_0 - I}{I} = \frac{\sigma c l}{1 - R}, \tag{4.4}$$

where the absorption is now proportional to the difference in light intensity in the presence of an absorber, I, and without an absorber, I_0.[15]

CEAS involves injecting laser light through the back of one cavity mirror and detecting the light escaping the opposite cavity mirror, after it has made many round trips within the cavity. Thus, the amount of light reaching the detector is significantly reduced relative to the laser intensity incident on the cavity, and the low power of radiation generated through frequency mixing necessitates detection using a photo-multiplier tube (PMT); in our experiments it was estimated that 15 pW of UV radiation exits the cavity.

In this work, the minimum detectable absorption, $\alpha_{\text{min}} = \sigma c_{\text{min}}$, has been estimated using:

$$\alpha_{min} = \frac{1 - R}{l} \frac{\Delta I_{min}}{I}, \tag{4.5}$$

where the quantity $\frac{\Delta I_{min}}{I}$ has been taken as the standard deviation of difference between the fitted line profile and the experimentally recorded data. Both equation 4.4 and 4.5 require knowledge of the loss associated with the cavity mirrors, $(1 - R)$. This can be determined by measuring a known absorber. However, the concentration of OH produced by the discharge source was not known and thus the mirror reflectivities were calibrated using the $2_0^3 4_0^3$ band of formaldehyde.

4.4.1 Mirror Reflectivity Determination

An alternative to calibrating the mirror reflectivities with a known absorber would have been to employ cavity ring down spectroscopy (CRDS).[16] CRDS requires injecting a pulse of light into the cavity and recording the decay in light intensity escaping the cavity, after multiple trips, as a function of time. Alternatively, for continuous-wave radiation, an acousto-optic modulator is used to rapidly 'switch off' the radiation incident on the cavity. This leads to a *ring down time*, τ, which, in the presence of an absorbing medium, depends

upon: the mirror reflectivity, R; cavity length, L; absorption coefficient, $\alpha = \sigma[\mathrm{OH}]$; and the length of the absorbing medium, d, according to equation 4.6. For an empty cavity without an absorbing medium this equation reduces to equation 4.7.[15]

$$\tau = \frac{L}{c\left((1-R)+\alpha d\right)} \tag{4.6}$$

$$\tau_0 = \frac{L}{c\,(1-R)} \tag{4.7}$$

From equation 4.7 it is possible to experimentally determine the mirror reflectivity, however with the current mirrors which had reflectivities of $R = 0.99786$, the resulting short ring down times, $\tau \approx 360$ ns, were too difficult to measure experimentally due to the low intensity of light leaving the cavity combined with the fast time response (and associated low resistance) required to reliably observe the decay on the PMT. Similarly, it is possible to measure the phase shift of sinusoidal modulated light as it passes through the cavity, but the low reflectivity of this cavity produces a phase shift of less than 10°, which was too small to accurately observe experimentally.[15,17,18] Consequently, the calibration of the mirror reflectivity was determined through a CEAS measurement of a known absorber, in this case formaldehyde.

As seen above, all cavity methods require a value of R to be determined in order to return absolute concentrations. Manufacturers quote a reflectivity for their mirrors; however these are not sufficiently accurate, and also, the quality of the mirror coatings may degrade with time, in addition to the variable quality of mirror coating. Therefore, it is necessary to determine the reflectivity experimentally.

The most feasible method for calibrating the reflectivity of the mirrors of our spectrometer is to use a known absorber in the cavity. As discussed in the previous chapter, there have been a number of measurements on formaldehyde around 308 nm.[19–21] Unfortunately, at the wavelengths near the OH spectral lines, the $2_0^3 4_0^3$ vibronic band of formaldehyde is poorly assigned and quite congested and the rotational constants are not known, possibly due to predissociation.[19,21] Therefore, the peak absorption cross section from a strong unidentified absorption feature of HCHO, near the $Q_1(2)$ OH transition at 32458 cm^{-1} was determined, chosen so as to minimise differences between the formaldehyde and the OH spectrometers, since mirror reflectivity also shows some wavelength dependence.

The formaldehyde samples were generated in the same manner discussed in the previous chapter. The peak absorption cross section of a blended spectral feature of formaldehyde was determined from the variation in the magnitude of an absorption signal with pressure. The measurements employed multi-pass direct absorption, passing the light repeatedly between a pair of mirrors separated by ≈ 40 cm, resulting in a optical path length of 282 cm. The variation of the spectral feature with pressure is illustrated in Figure 4.4a, with the resulting maximum absorption *versus* pressure plotted in Figure 4.4b, from which the peak absorption cross section was determined to be $\sigma_{\text{peak}} = (9.87 \pm 0.7) \times 10^{-21}\,\text{cm}^2\,\text{molecule}^{-1}$, using the Beer-Lambert law (equation 4.3). This value appears reasonable based upon similar spectra taken in this region.[19,21] As noted in Chapter 3, this method was used to determine the peak absorption cross section of a number of isolated rotational lines in the $2_0^2 4_0^1$ vibrational band of formaldehyde at 325 nm, and yielded good agreement with the literature and simulations, as illustrated in Table 3.5 in Chapter 3.[19–22]

Once the peak absorption cross section was known, an optical cavity was constructed, in which the 308 nm cavity mirrors were separated by 45 cm. The variation of the cavity signal with pressure was measured, as illustrated in Figure 4.4c, and the peak absorption cross section was used with equation 4.4 to determine the mirror reflectivity from a plot of the cavity signal *versus* pressure, shown in Figure 4.4d. The returned reflectivity was $R = 0.99786 \pm 0.00016$ and provides an enhancement factor, equivalent to $1/(1-R)$, of ≈ 500. While not a very substantial enhancement, mirror coatings in the UV do not currently produce mirror reflectivities substantially higher than those used in this work. A possible enhancement factor of ≈ 1000 may be achievable, but an enhancement of ≈ 100000 would be required to detect atmospheric OH with this spectrometer. However, this was not the goal in developing our UV source. The enhancement factor of 500 results in an effective path-length of $l/(1-R) = 210 \pm 17$ m, which is easily sufficient to detect the OH radicals generated with the mercury lamp.

4.4.2 Hydroxyl Radical Concentration

The strongest absorption feature in the A $^2\Sigma^+$ - X $^2\Pi$ (0,0) band is the $Q_1(2)$ rotational line, which occurs very close to the $Q_{21}(2)$ satellite line. An example spectrum of the two

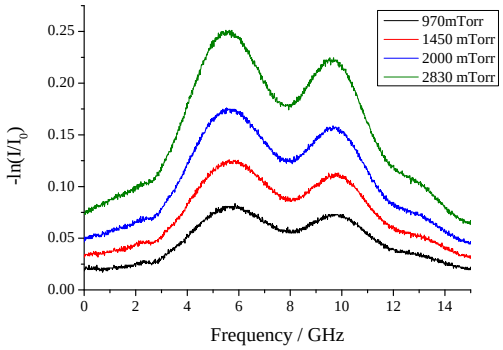

(a) Example HCHO multi-pass data.

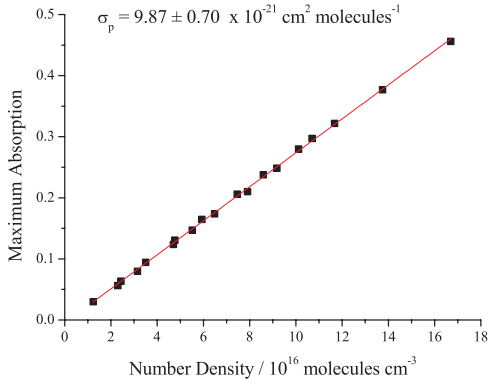

(b) Absorbance as a function of pressure, used to determine σ_p.

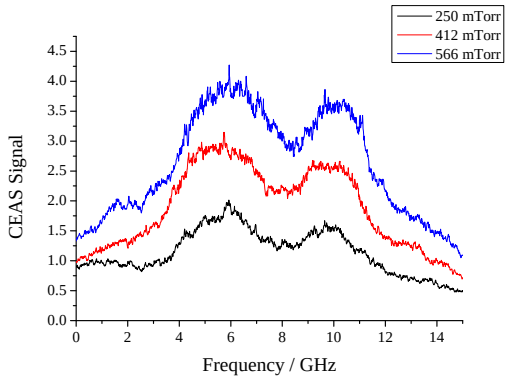

(c) Example HCHO cavity data.

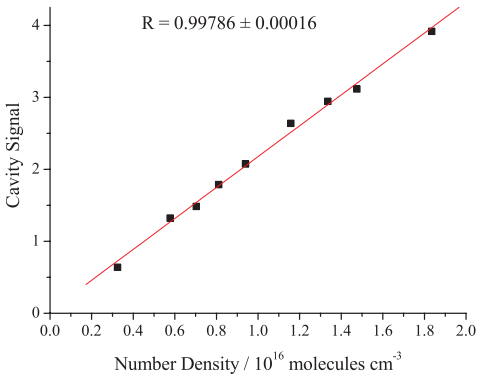

(d) CEAS signal as a function of pressure, used to determine mirror reflectivity.

Figure 4.4: Data used to calculate the reflectivity of the mirrors.

Q lines is shown in Figure 4.5, with a Voigt lineshape fitted to each line.

The line intensities are in the ratio 3:1, in agreement with Hancock and Kasyutich[23] and Dorn *et al.*[12] as well as simulations using LIFBASE.[?] In addition to this, the separation between the line centres is 17.5 GHz, in good agreement with LIFBASE which predicts a separation of 17 GHz. The discrepancy may be due to pressure-induced shift of the line centres, which Kasyutich reports to be 0.6 ± 0.1 GHz atm^{-1} and 0.6 ± 0.2 GHz atm^{-1} for the $Q_1(2)$ and $Q_{21}(2)$ transitions, respectively, when Ar is the buffer gas, and 0.4 ± 0.1 GHz atm^{-1} and 0.5 ± 0.1 GHz atm^{-1}, respectively, when N_2 is the buffer gas.[24] A further contribution to this difference could be due to nonlinear scanning of the frequency of the near-infrared diode laser at the extremes of the individual scans used to produce Figure 4.5. However, the frequency scale was determined in the same manner as in the

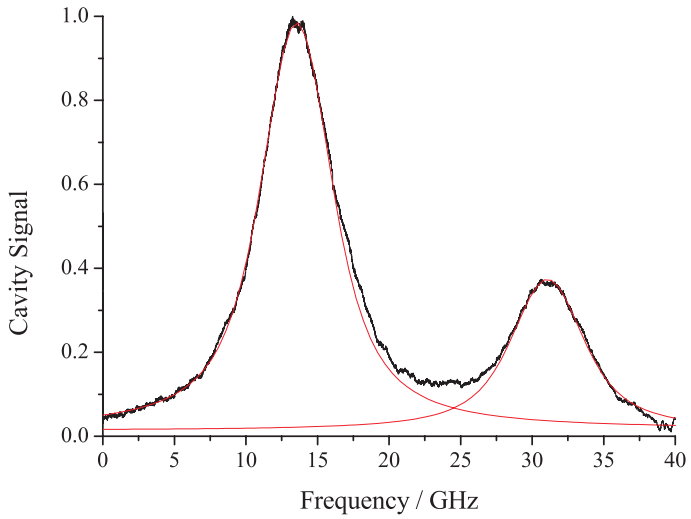

Figure 4.5: Example cavity data with the $Q_1(2)$ line shown on the left and the $Q_{21}(2)$ line shown on the right and the Lorentzian fit shown in red. This spectrum was pieced together by overlapping two mode-hop-free scans which both contained the $Q_1(2)$ line centre.

previous chapter for formaldehyde, which proved to be very robust even when piecing several spectral regions together.

The Voigt lineshapes were fitted using Origin Pro,[?] with a fixed Gaussian width equivalent to the thermal width of the hydroxyl radical, $w_G = 2.92\,\text{GHz}$, and allowing the Lorentzian width, w_L, to vary. Lineshapes fitted in this manner returned a Lorentzian width of 4.44 ± 0.21 GHz. This compares favourably with results in the literature of 3.6 ± 0.6 GHz and 3.8 ± 0.4 GHz from experiments employing the same mercury lamp system and Ar buffer gas with 308 nm radiation generated through frequency mixing of 835 nm and 488 nm laser beams;[23,24] and 4.0 ± 0.2 GHz from long-path absorption spectroscopy measurements.[12] Scan rates close to 100 Hz introduced significant instrumental broadening; thus the diode laser was scanned at 30 Hz for these measurements. Scan rates slower than 30 Hz returned the same Lorentzian widths, thereby confirming that instrumental broadening did not contribute significantly.

Initial measurements on the $Q_1(2)$ and $Q_{21}(2)$ lines were used to calibrate the quantity of OH produced by the mercury lamp and Ar/H_2O mixture. The analysis assumes the absorption cross section at line centre given by Dorn *et al.* ($\sigma_{\text{eff}}(\nu_0) = 1.67 \times 10^{-16}\,\text{cm}^2\,\text{molecule}^{-1}$ for the $Q_1(2)$ line),[12] and the mirror reflectivity determined above, and yields an OH concentration of $9 \times 10^{11}\,\text{molecules}\,\text{cm}^{-3}$. Furthermore, a detection limit of $\alpha_{\text{min}} = 4.65 \pm$

0.36×10^{-7} cm^{-1} was determined from the spectra in Figure 4.6, using equation 4.5.This compares well with previous detection limits of 1.25×10^{-6} cm^{-1} achieved using a similar cavity of length 58.5 cm.[23]

4.4.3 Pressure Broadening

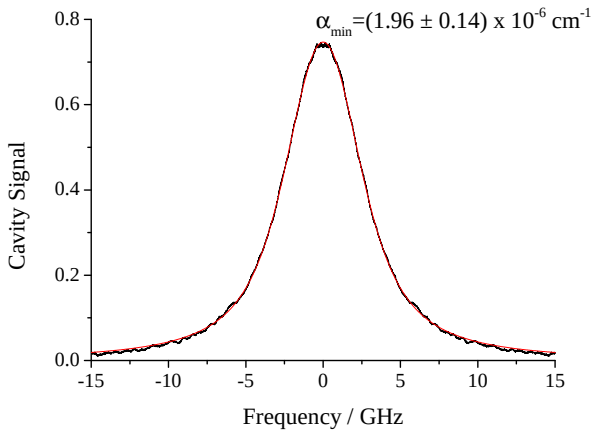

Figure 4.6: Example CEAS spectrum of the $Q_1(2)$ line of OH demonstrating the signal-to-noise ratio achieved and linewidth under the conditions discussed in the text. The data was recorded over a 20 s acquisition time.

As discussed in Chapter 1, in the presence of other species the spectral lineshape will be pressure broadened in addition to the natural broadening and the Doppler broadening. Since the area of the absorption profile is related to the concentration, pressure broadening of the lineshape is of interest in any experiment attempting to measure concentration and account must be made of the gas composition for *in situ* measurements.

In this work the measurements were limited by the experimental apparatus. Since the flow cell was open to the atmosphere, in order to allow a continuously replenishing supply of buffer/H_2O to enter, it was not possible to vary the pressure of the buffer gas. Measurements were taken by flowing the buffer gas of interest through the water at 1 bar, in place of Ar, but in the same manner as described above.

Collisionally broadened spectra were recorded with He, Ne, Ar and N_2 buffer gases and Voigt lineshapes were fitted using Origin Pro, fixing the Gaussian contribution to the thermal Doppler width. The Lorentzian widths, w_L, determined by this method are given

in Table 4.3, with literature values quoted for comparison. The literature values for the $Q_1(2)$ transition given in Table 4.3 were taken from Kasyutich,[24] and were recorded using sum frequency mixing of an 835 nm tunable diode laser with a frequency doubled diode laser operating at 488 nm. Kasyutich multi-passed the radiation through the same 23 cm mercury lamp OH generating system as used for our experiments, which was described above in Section 4.2. The literature values for the $P_1(2)$ transition given in Table 4.3 were taken from Shirinzadeh *et al.*,[25] where the frequency doubled output of a dye laser was used to probe OH radicals generated by the reaction of water vapour with $O(^1D)$. The $O(^1D)$ was formed by photolysing ozone using mercury lamps. The state averaged values in Table 4.3 were taken from Engleman,[26] where flash photolysis of H_2O_2 vapour was used to produce OH radicals which were then investigated using a quartz flash lamp. The probe flash lamp fired a few μs after the flash photolysis lamp, and the probe radiation was double passed through a 90 cm absorption cell to achieve a path length of 180 cm.

Table 4.3: The Lorentzian widths, w_L in GHz atm^{-1}, measured for various buffer gases both in this study and others.

	He	Ne	Ar	N_2
$Q_1(2)$ This work	2.87 ± 0.27	2.88 ± 0.3	4.44 ± 0.21	6.55 ± 0.31
$Q_1(2)$[24]	1.7 ± 0.2	1.8 ± 0.3	3.8 ± 0.4	5.3 ± 0.8
$P_1(2)$[25]	1.71 ± 0.07	1.46 ± 0.16	4.2 ± 0.07	6.5 ± 0.16
State averaged[26i]	1.5 ± 0.3	1.9 ± 0.4	4.0 ± 0.8	4.3 ± 0.9

[i] error estimated at $\approx 20\%$

The discrepancies between the pressure broadening linewidths recorded in this work and the literature values are possibly due to unaccounted broadening from N_2 in the atmosphere, since the flow tube was open to ambient air throughout these measurements. A more accurate method to determine these parameters would requiring varying the pressure of the collision partner, ideally in a sealed flow tube, but the method of creating a continuous supply of OH *in situ* used in this chapter does not allow this.

These measurements neglect the contribution from the water vapour to the broadening of the lineshape. Despite the high pressure broadening parameter of water, estimated to vary with J between 2.5 and 12 GHz atm^{-1},[26] the low concentration should not contribute to the width significantly. Previous measurements have found collisional broadening to be

independent of rotational state for all bath gases except water.[26] However, a more recent study has measured minor variations across the low J states, but negligible within the limitations of our spectrometer.[24]

In addition to indicating the sensitivity of the spectrometer to OH concentrations these measurements have calibrated the concentration of OH generated by the mercury lamp, which will be of use in the next section where modulation techniques are investigated. Modulation spectroscopy is of great interest with respect to our spectrometer. In Chapter 5 the application of frequency modulation to the $\tilde{A} - \tilde{X}$ electronic transition of CN photofragments is used in order to record nascent lineshapes. Combining frequency modulation and sum frequency generation may result in an ultraviolet absorption spectrometer which can measure vector correlations in photofragments. Furthermore, an important aspect of photodissociation studies is the Doppler shift in the photofragments, which reveals the translational energy of the fragment; this requires a large amount of confidence in the frequency scale of the spectrometer. In the previous chapter the formaldehyde Doppler width returned the expected thermal width of the lineshape. As discussed above, the linewidths of these cavity measurements are in reasonable agreement with the literature, and some other buffer gases have been used to further explore the frequency scale of the spectrometer.

4.5 Modulation Techniques

The cavity technique discussed above makes use of a path length enhancement to increase the signal intensity. Alternatively, the sensitivity of absorption spectroscopy can be increased by decreasing the noise in the detected signal. Some level of noise is unavoidable in any measurement; however the contribution noise makes may be decreased by considering two types of noise: white noise and pink noise.

White noise is so called because it occurs throughout the spectrum and its amplitude is independent of frequency. White noise occurs due to thermal fluctuations of the electrons, hence it is often termed thermal noise.[27] Conversely, pink noise is inversely dependent upon the frequency, hence it is also termed $1/f$ noise, and is often overshadowed by white noise at higher frequencies.[28] The occurrence of white noise across a whole frequency spectrum and the frequency dependence of pink noise allows the use of modulation techniques

to reduce the noise in a signal. This is achieved by encoding the signal at a high frequency by modulating the light intensity or frequency. Demodulation or phase sensitive detection of the resulting signal has two effects upon the noise: it reduces pink noise as detection happens at higher frequencies and the detection process can discard signals at any frequencies not corresponding to the modulation frequency, thereby reducing white noise.

Two methods of noise reduction through modulation have been used in this chapter, both of which rely upon modulating the laser light incident upon the sample. The simplest method of modulating the light source is to turn it off and on periodically. This is achieved by mechanically chopping the light beam, and is implemented in this experiment by chopping the diode beam incident upon the BBO crystal. The chopper wheel causes a sinusoidal variation in the light intensity at a fixed frequency, approximately 1 kHz, which is then used as a reference signal by a lock-in amplifier (EG & G 7265 Dual Phase DSP Lock-in Amplifier) to reduce the noise by attenuating anything not occurring at the reference frequency. The lock-in amplifier integrates the product of the detected signal and reference signal over a short timescale, in this case a few milliseconds, attenuating any noise not occurring at, or close to, the frequency of the reference signal and thus removing a large amount of white noise. In order to achieve this, the laser must be scanned at a frequency which is significantly less than the chopper frequency, typically a few Hz, requiring relatively long acquisition times. This is important to note as the laser stability drifts over time, introducing broadening and noise into lineshapes as mode-hops start to occur.

Under these conditions the same $Q_1(2)$ absorption line was investigated, using the optical cavity, and a comparable Lorentzian linewidth was determined, indicating little instrumental broadening. A minimum detectability of $(8.7 \pm 0.7) \times 10^{-6}$ cm^{-1} (2.13 ± 0.23 ppb) was found, which is larger than the detection limit without the lock-in amplifier. This is largely due to the longer acquisition times required due to the slow scan rate of the diode laser, with the total acquisition time limited by the frequency stability of the laser. A typical spectrum recorded using a cavity with a lock in amplifier is shown in Figure 4.7 where the acquisition time is the same as that of the CEAS measurement recorded without a lock-in amplifier, shown earlier in Figure 4.6.

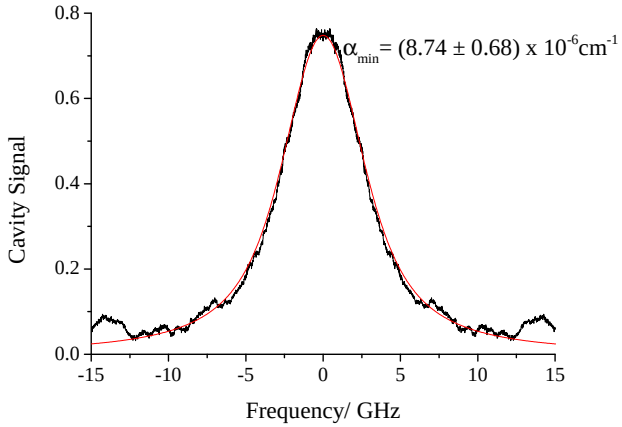

Figure 4.7: Example data measured using the cavity and lock-in amplifier demonstrating the noise and linewidth under the conditions discussed and over the same 20 s timescale as the CEAS measurement recorded without a lock-in amplifier, as shown in figure 4.6.

It was not possible to observe a signal without the optical cavity using the lock-in amplifier. However, the spectrometer was limited by the modulation frequencies achievable with a mechanical chopper wheel, since the laser scan rate must be a few orders of magnitude slower to allow the lock-in amplifier to integrate the signals. An acousto-optic modulator (AOM) or photoelastic modulator (PEM) can achieve the same sinusoidal variation in the light intensity, but both are capable of much higher switching frequencies than a mechanical chopper wheel. This would improve the acquisition time, thus avoiding the problem of frequency stability of the near-infrared diode laser. Higher frequency modulation would also reduce the 1/f noise. However, both AOMs and PEMs significantly reduce the power of the radiation passing through them, and since laser power is already a problem, these devices were not suitable for the current spectrometer.

The lock-in amplifier did not significantly reduce the noise in the signal at the modulation frequencies used. This suggested that perhaps higher frequencies or different modulation techniques might have more success. In particular, modulating the signal at MHz or GHz frequencies rather than kHz may produce a better signal-to-noise. These modulation frequencies are more readily achievable using techniques such as wavelength modulation.

4.6 Wavelength Modulation Spectroscopy

Wavelength and frequency modulation spectroscopy (WMS and FMS respectively) represents two limits of the same generaal approach. The former typically involves modulation at kHz frequencies and the latter modulation at frequencies of MHz or GHz. The theory of these techniques is well defined, having originally been used in nuclear magnetic resonance spectroscopy before their application to laser spectroscopy.[29] This chapter focusses on WMS, and the discussion herein will be limited to that technique. In Chapter 5 we will discuss and apply FMS to photodissociation dynamics of ICN.

4.6.1 Wavelength Modulation Theory

The theory for both WMS and FMS relies on the same principle: the electric field of the laser oscillates at the carrier frequency, ω_0, according to:

$$E(t) = E_0 \exp(i\omega_o t) \ . \tag{4.8}$$

A sinusoidal variation, $M \sin \omega_m t$, applied to the carrier frequency, ω_0, alters the electric field, according to:

$$E(t) = E_0 \exp[i(\omega_o t + M \sin \omega_m t)] \ . \tag{4.9}$$

This new description of the electric field has terms depending upon the applied modulation frequency, ω_m, and the modulation index, M.[30]

The theory of wavelength modulation is treated in terms of the instantaneous frequency, defined as the rate of change of the phase, given by the complex exponential of equation 4.9. The instantaneous frequency, w_i, is given by:

$$\omega_i(t) \equiv \frac{d}{dt}(\omega_0 t + M \sin \omega_m t) = \omega_0 + \Delta F \cos \omega_m t \tag{4.10}$$

where $\Delta F = M\omega_m$ is known as the modulation amplitude.

The light intensity transmitted through an absorbing medium is attenuated by absorbance, a, according to:

$$I_T = I_0 \exp(-a) \ . \tag{4.11}$$

In the limit of small absorbance, $a \ll 1$, this may be simplified to give:

$$I_T(\omega) = I_0(\omega)[1 - a(\omega)] \ . \tag{4.12}$$

Expanding this as a Taylor series about the carrier frequency leads to equation 4.13

$$I_T(\omega) = I_0\left[1 - a(\omega_0) - \left.\frac{da}{d\omega}\right|_{\omega_0}(\omega - \omega_0) - \frac{1}{2!}\left.\frac{d^2a}{d\omega^2}\right|_{\omega_0}(\omega - \omega_0)^2 \ldots\right] \tag{4.13}$$

Making use of the instantaneous frequency in equation 4.10, it is possible to write equation 4.13 in terms of the modulation amplitude and modulation frequency:

$$I_T(\omega) = I_0\left[1 - a(\omega_0) - \left.\frac{da}{d\omega}\right|_{\omega_0}\Delta F\cos\omega_m t - \frac{1}{2!}\left.\frac{d^2a}{d\omega^2}\right|_{\omega_0}(\Delta F\cos\omega_m t)^2 \ldots\right] \ . \tag{4.14}$$

The component of the transmitted intensity which is oscillating at the modulation frequency, ω_m, is given by:

$$I_T \propto \left.\frac{da}{d\omega}\right|_{\omega_0}\Delta F \tag{4.15}$$

and can be retrieved by demodulating at the modulation frequency, achieved by mixing with a reference channel, itself modulated at w_m. This is known as the first harmonic,[i] and the WMS signal is equivalent to the derivative of the absorption signal. Demodulation at the n^{th} harmonics produce WMS signals equivalent to the n^{th} derivative of the absorption signal.[31]

The modulation frequencies used for WMS are typically much smaller than the spectral linewidth, $\omega_m \ll \Gamma$ where Γ is the FWHM. Typically, modulation frequencies at kHz are used. The modulation amplitude, $\Delta F = M\omega_m$, is determined experimentally from the maximum frequency excursion from the near-infrared diode laser carrier frequency, w_0, as seen on a near-infrared spectrum analyser. This is illustrated in Figure 4.8. The modulation amplitude is the frequency difference between the red trace and the edge of the frequency envelope in the black trace.

The limit of a modulation amplitude being much less than the FWHM, $\Delta F = M\omega_m \ll \Gamma$, is known as the derivative limit of WMS, where the lineshape is described by the

[i]The $\cos^n\omega_m$ terms can be rewritten as $\cos n\omega_m t$ terms, i.e. oscillate at higher harmonics of the modulation frequency ω_m.

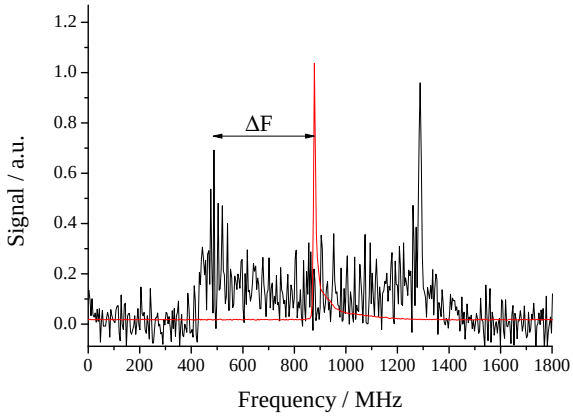

Figure 4.8: Spectrum analyser trace showing the range of frequencies generated by modulating the near-infrared diode laser current. The spectrum analyser trace of the unmodulated laser output is shown in red.

above discussion. This limit does not produce the maximum signal size or, therefore, the maximum sensitivity. As the modulation amplitude is increased the signal size increases; however, the experimental linewidth also increases with modulation amplitude. Taking the ratio of the FWHM and the modulation amplitude and assigning a dimensionless parameter, b, defined as:

$$b = \frac{2\Delta F}{\Gamma} \tag{4.16}$$

leads to experimentally observed optimum values of b for different lineshapes and harmonic frequencies, shown in Table 4.4.[32,33]

Table 4.4: The optimum values of b for Doppler and Lorentzian broadened lineshapes at different harmonics.[33]

Harmonic frequency	1	2	4	6
Doppler	1.6	2.1	3.6	5.2
Lorentzian	2.0	2.2	3.9	7.4

Typically, experiments are not performed in the derivative limit but rather at the optimum value of b, achieved experimentally by increasing the modulation amplitude until broadening becomes more significant than the gain in signal size. This is illustrated in Figure 4.9b where the red line shows the predicted effect of increasing signal size, measured

as the difference between the two peaks shown in Figure 4.9a. The black dots were measured from this experiment and correspond to the values obtained from Figure 4.9a.

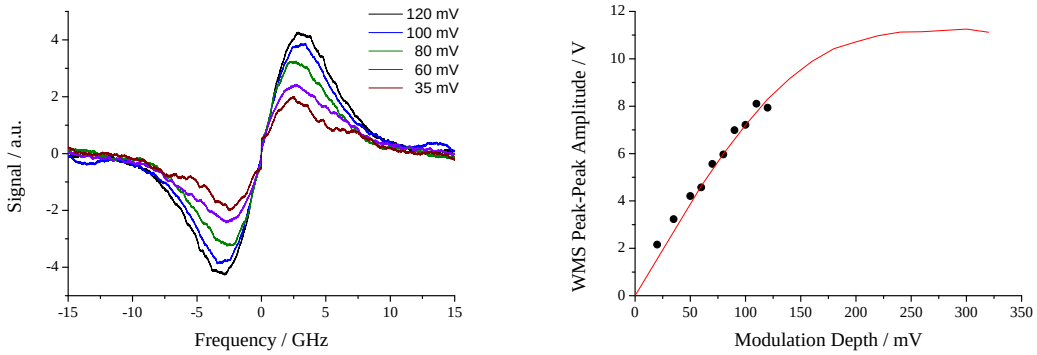

(a) Example WMS-CEAS spectra recorded at various modulation amplitudes.

(b) The black dots are the effect of varying the modulation amplitude on the linewidth with the red line illustrating the theoretical trend, as discussed in the text.

Figure 4.9: Example WMS-CEAS spectra with the variation in the WMS signal peak to peak amplitude as a function of the modulation depth applied to the near-infrared diode laser.

The optimum modulation amplitude for the OH absorption lines measured with our spectrometer would lead to a modulation frequency greater than the scan range of the diode laser. This is due to the large Doppler width in the UV associated with a low mass molecule (equation 1.14). Therefore, a modulation frequency which produced large WMS signals at a modulation depth which was below the voltage ramp applied to scan the near-infrared diode laser's grating was used.

4.6.2 WMS Results

The WMS signal recorded using a single pass through the sample, with a path length of 23 cm, is shown in Figure 4.10. The WMS lineshape was fitted with a fixed Doppler width, allowing the Lorentzian width to vary, as before. This analysis was carried out using a Matlab script based upon the method of Kluczynski *et. al.*.[34] The returned value of $w_L = 4.11 \pm 0.40$ GHz compares well with the CEAS width determined above, though has larger error than the CEAS measurement ($w_L = 4.44 \pm 0.21$ GHz) since the signal-to-noise ratio is much lower in the WMS signal. The minimum detectability was determined

from:

$$\alpha_{\min}(BW_{\text{eff}}) = \frac{abs}{l(S/N)}\sqrt{\pi\tau n}\ , \tag{4.17}$$

where S/N is the signal to noise ratio (taken as twice the standard deviation of the residual); *abs* is the peak absorbance, l is the path length, τ is the time constant from the lock in amplifier and n is the number of averages.[35] The above measurements returned $\alpha_{\min} = (9.45 \pm 1.04) \times 10^{-7}\text{cm}^{-1}$, which is comparable with the $\alpha_{\min}$ determined from CEAS, $(4.65 \pm 0.36) \times 10^{-7}\text{cm}^{-1}$.

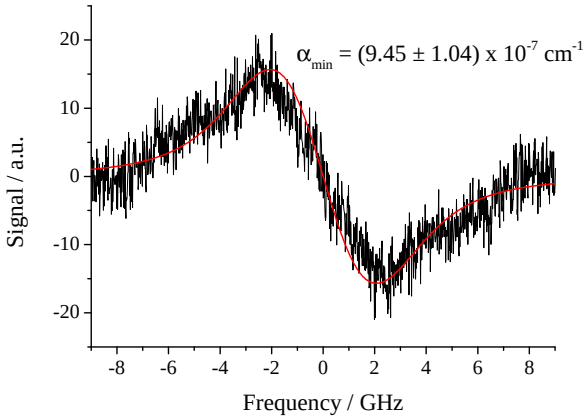

Figure 4.10: Example data using WMS in the absence of a cavity.

Comparing CEAS and WMS at this point could sensibly guide their experimental implementation and use. Whilst aligning an optical cavity is not as straightforward as simply modulating the laser current, the resulting signals from the optical cavity are far easier to interpret directly from the PMT. In contrast, the WMS signals require background subtraction to observe the absorption signal, making it more complicated to tune the laser to the transition. CEAS is therefore a more convenient tool for these studies.

4.6.3 WMS-CEAS

Combining CEAS with WMS allows the gain in path length to be combined with the noise reduction of WMS. This is simply implemented by modulating the laser current and injecting the UV radiation into the same optical cavity used before. The resultant signal is show in Figure 4.11, with a fitted Voigt lineshape shown. The fit employed the same

Matlab script as before with a fixed thermal Gaussian contribution.

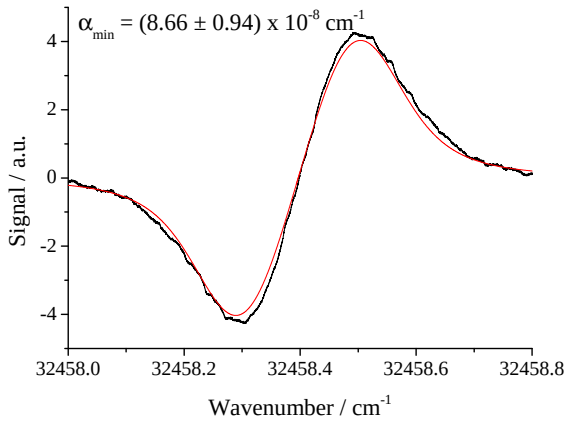

Figure 4.11: Example cavity data using WMS to reduce the noise.

The minimum detectability, $\alpha_{\min}$, for CEAS-WMS has been determined by adjusting equation 4.17 to include the mirror reflectivity, R:[35]

$$\alpha_{\min}(BW_{\text{eff}}) = (1-R)\frac{abs}{l^{S}/_{N}}\sqrt{\pi\tau n}. \tag{4.18}$$

This returned an $\alpha_{\min} = (8.66 \pm 0.94) \times 10^{-8}$ cm^{-1}, representing much greater sensitivity than either CEAS or WMS on their own.

4.7 Summary of OH Spectroscopy Using SFG

Up to this point this chapter has concentrated on extending the use of tunable narrow-bandwidth near-infrared diode lasers to the UV region of the electromagnetic spectrum, where the strong electronic transitions of OH occurs. The application of the narrow-bandwidth of the developed spectrometer has been explored through the use of cavity-enhanced absorption spectroscopy in conjunction with lock-in amplification and wavelength modulation, as well as wavelength modulation spectroscopy in the absence of an optical cavity. The minimum detectability of each of these techniques is summarised in Table 4.5.

Table 4.5: The values of $\alpha_{\min}$ measured for each of the techniques used in this chapter.

	CEAS	Lock-in CEAS	WMS CEAS	WMS
$\alpha_{\min}/10^{-8}\text{cm}^{-1}$	46.5 ± 3.6	877 ± 67	8.66 ± 0.94	94.5 ± 10.4

These detection limits do not compare well with mid-infrared studies in which detection limits of the order of 10^{-10} and 10^{-11} are achievable.[36] However, in these wavelength regions, mirror reflectivities of up to $R = 0.99999$ are possible, and the laser powers incident on the samples are of the order of 10 mW rather than the 10 μW of our spectrometer. Despite this, electronic transitions which occur in the UV have much larger absorption cross sections than the vibrational transitions which occur in the mid-infrared. Thus, the absorption cross section of the $Q_1(2)$ rotational line used in this work is $1.67 \times 10^{-16}\,\text{cm}^2\text{molecule}^{-1}$ and results in minimum detectable concentrations of $c_{\min} = (5.19 \pm 0.70) \times 10^8 \text{molecules}\,\text{cm}^{-1}$ or 21.0 ± 2.8 ppt (parts per trillion) for WMS-CEAS.

These detection limits also compare well with literature values; Hancock and Kasyutich quote $\alpha_{\min} = 1.25 \times 10^{-6}\,\text{cm}^{-1}$ for their CEAS measurement of OH employing a similar spectrometer based upon frequency mixing a 488 nm Ar ion laser and an 835 nm ECDL to produce 0.5 μW of tunable UV radiation.[23] This suggests that the increased laser power of the spectrometer used in this work (13 μW) provides greater sensitivity. Similarly, Oh[?] investigated direct absorption and $2f$ WMS spectroscopy using the $Q_1(1)$ rotational line of OH and an SFG system comprising a 488 nm Ar ion laser and an 835 nm diode laser, generating 2 μW of UV radiation. The OH gas sample was generated by reaction of H_2O with fluorine generated in a discharge and while the optical path length through the sample was short, at 5 cm, absorption of 6.3% was observed. For this system, Oh reports a WMS 2f detection limit of $\alpha_{\min} = 9.9 \times 10^{-7}\,\text{cm}^{-1}$, which is in agreement with the $1f$ WMS detection limit reported here.[?]

The experimental linewidths measured in this chapter demonstrate that the spectrometer does not contribute to line broadening. This narrow-bandwidth suggests that our spectrometer will be highly suited to the study of photodissociation dynamics studies, in which the experimental lineshape can provide further insight into the potential energy surfaces involved in the dissociation.

4.8 Nitric Acid Photolysis

Having used our UV source to probe a continuous stream of OH, attention now turns to time-resolved absorption spectroscopy. Nitric acid photolysis has been studied extensively *via* LIF of the OH fragment,[37–42] as well as in time-of-flight studies on both NO_2, NO and O fragments.[41–44] Since the absorption cross section of HNO_3 at 193 nm is large, $\sigma_{\text{peak}} = 1.6 \times 10^{-17}\,\text{cm}^2\text{molecule}^{-1}$, and the OH quantum yield is approximately 50%, a large number of OH radicals are produced when photolysing at this wavelength.[45] These factors make nitric acid photolysis a good prototype system for reaction dynamics studies employing the continuous-wave UV source.

Photolysis at 193 nm produces the products given in equations 4.19-4.23, with the OH quantum yield at this wavelength reported with some dispute. Various experimental methods have been used, such as high resolution infrared spectroscopy ($\Phi(\text{OH}) = 0.47 \pm 0.06$);[46] photofragment translational spectroscopy of both OH and the O atom ($\Phi(\text{OH}) = 0.6 \pm 0.1$);[43] and LIF of the OH product giving ($\Phi(\text{OH}) = 0.33 \pm 0.06$).[38]

$$\text{HNO}_3 + h\nu \rightarrow \text{OH}(X) + \text{NO}_2(X^2A_1) \tag{4.19}$$

$$\rightarrow \text{OH}(X) + \text{NO}_2(1^2B_2) \tag{4.20}$$

$$\rightarrow \text{O}(^1D) + \text{HONO}(X^1A') \tag{4.21}$$

$$\rightarrow \text{O}(^3P) + \text{HONO}(\tilde{a}^3A'') \tag{4.22}$$

$$\rightarrow \text{O}(^3P) + \text{HONO}(X^1A') \tag{4.23}$$

In addition to the large absorption cross section of the parent, a second favourable factor is that the OH fragment is produced with very little rotational or vibrational excitation, making it ideally suited to our spectrometer's operating region.[42,47–49] A LIF spectrum of the nascent OH is shown in Figure 4.12a with the 306.5 nm to 309 nm operating region of our spectrometer indicated by the red box.

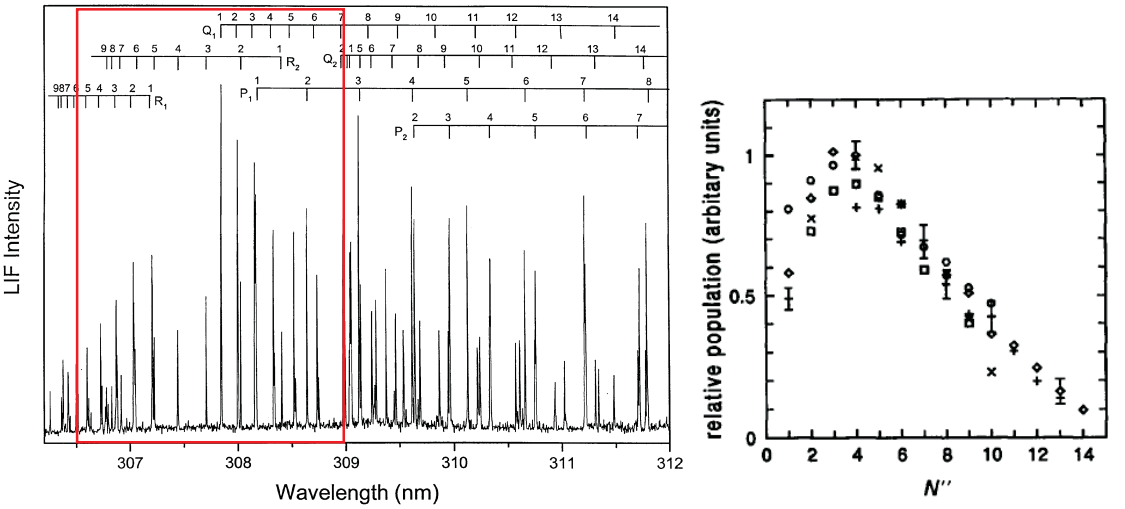

(a) Nascent OH LIF spectrum.

(b) Nascent OH rotational distribution.

Figure 4.12: (a)Nascent OH LIF spectrum following photolysis of a supersonic jet of HNO_3, reproduced from Li *et al.*.[42] The red box illustrates the working region of our spectrometer.
(b) Nascent OH rotational distribution following 193 nm photolysis of a thermal nitric acid sample. The symbols $\circ, \times, \square, \diamond$ and $+$ correspond to rotational states probed using R_2, P_1, P_2, Q_1 and Q_2 transitions, respectively, reproduced from Leu *et al.*.[40]

The energy available to the products may be written:

$$\begin{aligned} E_{\text{avl}} &= h\nu + E_{\text{int}}(\text{HNO}_3) - D_0(\text{HO} - \text{NO}_2) \\ &= E_{\text{int}}(\text{NO}_2) + E_{\text{rot}}(\text{OH}) + E_{\text{trans}}(\text{OH}) + E_{\text{trans}}(\text{NO}_2). \end{aligned} \tag{4.24}$$

Since there is very little internal excitation of the OH fragment, most of the available energy ($\approx 60\%$) is partitioned into internal energy of the NO_2.

However, the two possible NO_2 co-fragments, shown in equations 4.19 and 4.20, are formed with different amounts of energy, with the electronically excited NO_2 also possessing a larger amount of translational energy ($E_{\text{trans}} = 3600\,\text{cm}^{-1}$) than the ground state fragment ($E_{\text{trans}} = 1500\,\text{cm}^{-1}$).[42] This leads to a bimodal distribution of the OH recoil velocity. Slow OH fragments ($E_{\text{trans}} = 4000\,\text{cm}^{-1}$) are formed with ground state NO_2, and fast OH fragments ($E_{\text{trans}} = 9700\,\text{cm}^{-1}$) are formed with the electronically excited NO_2, in the ratio 2.2:1, as shown in Figure 4.13. Table 4.6 summarises the above discussion and gives the partitioning of available energy into the NO_2 and OH products.[42–44]

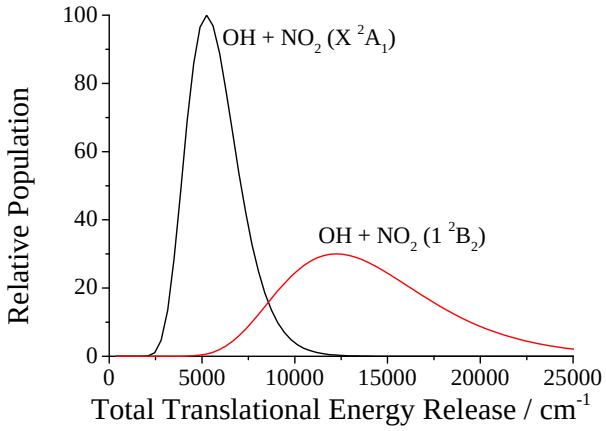

Figure 4.13: Bimodal translational energy distribution showing the slow channel in black and the fast channel in red. Adapted from Myers *et al.*.[44]

Table 4.6: Energy partitioning following 193 nm photolysis of nitric acid in a supersonic jet with $E_{\mathrm{avl}} = 35\,100\,\mathrm{cm}^{-1}$ and $D_0(\mathrm{HO-NO_2}) = 200\,\mathrm{kJmol}^{-1}$.[42]

	$OH+NO_2(X^2A_1)$ (eq 4.19)		$OH+NO_2(1^2B_2)$ (eq 4.20)	
	Energy / cm^{-1}	% of E_{avl}	Energy / cm^{-1}	% of E_{avl}
$E_{\mathrm{trans}}(\mathrm{OH})$	4000	11.4	9700	27.6
$E_{\mathrm{trans}}(\mathrm{NO_2})$	1500	4.3	3600	10.3
$E_{\mathrm{rot}}(\mathrm{OH})$	1700 (thermal)	4.8	120 (nonthermal)	0.3
$E_{\mathrm{int}}(\mathrm{NO_2})$	27900	79.5	21680[1]	61.8

[1] includes $9726\,\mathrm{cm}^{-1}$electronic excitation

The photodissociation of nitric acid at 193 nm occurs via the $S_3(2\ ^1A')$ excited state. As shown in Figure 4.14, the transition dipole moment connecting the ground state and the S_3 state lies perpendicular to the N-OH bond and parallel to a line connecting the terminal oxygens. The resulting bond fission causes the OH fragment to recoil in a perpendicular direction with respect to the initial transition dipole moment and, for a fast dissociation, perpendicular to the polarisation of the photolysis laser, i.e. the recoil anisotropy is negative and near limiting at $\beta \approx -0.6$.[45] If the probe radiation is counter propagating with respect to the photolysis laser, the velocity of the OH fragments is predominantly directed along the probe propagation direction, resulting in a large Doppler shift and an exceedingly large full width half maximum for the absorption profile of $\approx 16\,\mathrm{GHz}$.[45,50] This provided an additional experimental challenge, as the spectrometer is not able to

scan the full line profile. Instead, the spectrometer was stepped across more than half of the line profile and the results were symmetrised.

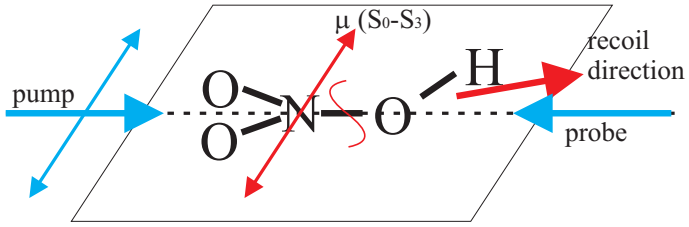

Figure 4.14: Illustration of the bond breaking process leading to OH from 193 nm photolysis.

4.9 Experimental

The spectrometer is the same setup discussed earlier in the chapter, with the sum frequency generated ultraviolet radiation directed through a 1.5 m flow cell where it overlaps with the output from an Excimer (Lamda Physik COMPex 205) operating at 193 nm, counter propagating through the flow cell. The probe laser was detected using an AC coupled avalanche photodiode (Hamamatsu APD module C5331-1) and the signals recorded using a digital storage oscilloscope (LeCroy Waverunner 6100A, 1 GHz bandwidth).

The grating of the near-infrared ECDL was stepped across the transition in discrete steps of 200 MHz, with the total frequency range limited by the single mode scan range of the diode, typically up to 20 GHz. The discrete voltage steps were applied to the grating by a 16 bit 100 kHz DAQ card (National Instruments); the DAQ card also recorded the output from the spectrum analyser to allow calibration of a frequency scale. A MATLAB program managed the control of the spectrometer and acquisition of data, with the communication with the oscilloscope occurring over a local area network.

The nitric acid was delivered into the cell by pumping the vapour above a 70% solution of aqueous nitric acid through the flow cell, with fresh samples used for each experiment and the sample kept in the dark to avoid photodecomposition. This method is predicted to give a 1:1 ratio of $HONO_2$:H_2O in the vapour.[51] Due to the large absorption cross section of $HONO_2$ the flow pressures were kept below 100 mTorr to avoid total absorption of the photolysis light. In addition to this, fluorescence interfered with the detected signal,

requiring the detector to be placed a significant distance from the cell, with the probe light passed through numerous irises to attenuate and discriminate against the fluorescence. The fluorescence has previously been attributed to electronically excited NO, generated from the decomposition of NO_2;[52] however, attempts to filter the fluorescence suggested that it occurs at 308 nm and is more likely to be fluorescence from nascent OH in the A state. Attenuation of the photolysis laser power reduced the fluorescence, but did not eliminate it, therefore background subtraction was employed for data collection.

4.10 Results

Initial measurements focused on the $Q_1(2)$ transition of the OH fragment due to its line strength and large population resulting from the photolysis, as discussed above. An example of the early time data (integrated over the time period 100 to 200 ns post photolysis) and its near-thermal late time counterpart (integrated over time period 8.9 to 9 µs post photolysis) are shown in Figure 4.15. The FWHM of 16.18 ± 0.55 GHz for the nascent profile was determined by fitting the distribution to a Gaussian. This compares well with the literature value of 16.3 GHz, recorded using photofragment translational spectroscopy on the OH^+ ion generated from HONO and OH produced by photolysing a molecular beam of nitric acid at 193 nm.[42,43] Fitting a Gaussian profile is an oversimplification of the absorption signal but provides a measure of the velocity distribution to compare with the literature. The measured FWHM corresponds to an average kinetic energy release of 9540 ± 120 cm^{-1}, very close to the energy of 9700 cm^{-1} reported for the fast channel, reported by Li *et al.*.[42]

4.10.1 Polarisation Dependence

As discussed above, the recoil anisotropy is known to be negative and near limiting.[45] In order to confirm this with our spectrometer, the excimer laser was polarised using a Rochon polariser. The two geometries discussed in Figure 1.9 of Chapter 1 were switched between by employing a photoelastic modulator, which will be discussed in greater detail in Chapter 5. Example spectra recorded using these two geometries are shown in Figure 4.16 along with a simulation in red. The two lineshapes and areas are essentially identical,

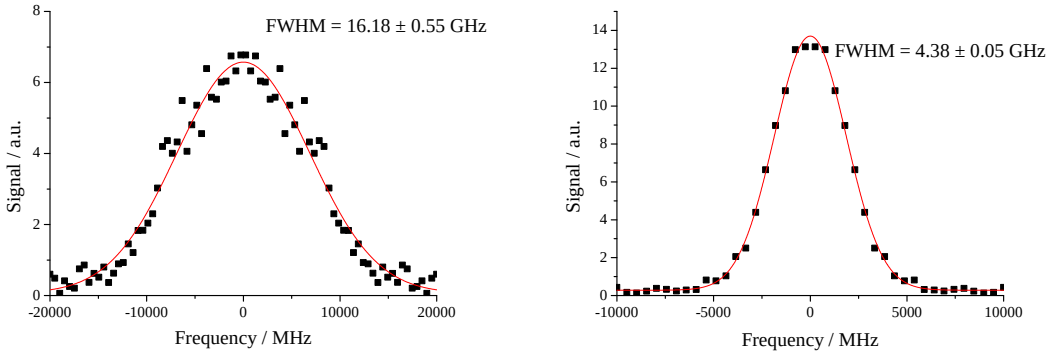

(a) (b)

Figure 4.15: Example OH absorption signals recorded on the $Q_1(2)$ transition following 193 nm photolysis. (a) Early time, 100 - 200 ns. (b) Late time, 8.9 - 9 µs

which suggests that the bipolar moments relating to polarisation of the rotational angular momentum are close to zero as expected for $N = 2$, $J = {}^3/_2$. Thus equation 1.16 in Chapter 1 can be approximated to:

$$D(w) = \frac{1}{2v_0}\left[1 - {}^1/_2\beta P_2\left(\frac{w}{v_0}\right)\right] \tag{4.25}$$

for both spectra.

This equation has been used to simulate the data shown in Figure 4.16 by convolving equation 4.25 with a Gaussian distribution to account for the speed distribution of the OH fragment. The simulation assumed the speed averaged value of $\beta = -0.6$.[45] The FWHM of the Gaussian distribution was taken as $1900\,\mathrm{m\,s^{-1}}$. This FWHM is an estimate, since the translational energy release into the OH product is dependent on the partitioning of energy into the NO_2 co-fragment, and in the work of Myers *et al.* the total translational energy release, shown above in Figure 4.13, is averaged across all the states of NO_2 and includes the NO_2 translational energy. The literature does not contain OH state specific velocity distributions for photolysis at 193 nm, however, August *et al.* studied $HONO_2$ photolysis at 280 nm where they found similar energy partitioning to photolysis at 193 nm, with $E_{\mathrm{rot}}(\mathrm{OH}) = 4.6\%$ and $E_{\mathrm{int}}(\mathrm{NO_2}) = 70\%$ of E_{avl}. In that work, the $R_2(1)$ branch was studied, and yielded a root-mean-squared OH velocity of $2.4\,\mathrm{km\,s^{-1}}$ with a velocity

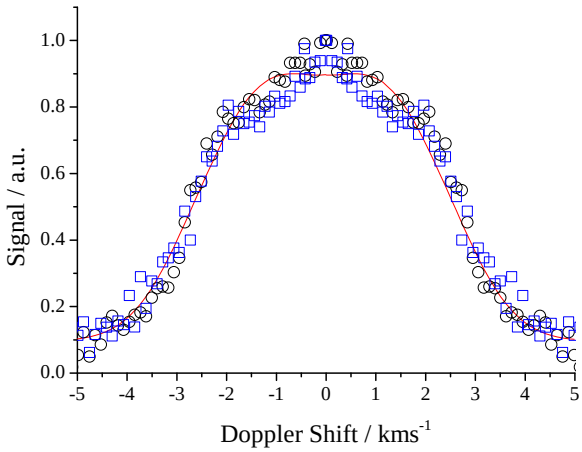

Figure 4.16: OH doppler profiles recorded in the two polarisation geometries of Figure 1.9 discussed in the text. The black hollow circles was recorded with the electric vectors of the pump and probe radiation parallel (Figure 1.9a); the blue hollow squares were recorded with the electric vectors of the pump and prove radiation perpendicular (Figure 1.9b); and the simulation produced by convolving equation 4.25 with a Gaussian with a FWHM of Gaussian $= 1900\,\mathrm{m\,s^{-1}}$ and using $\beta = -0.6$ is shown as a solid red line.

distribution consistent with a FWHM of $2.7\,\mathrm{km\,s^{-1}}$.[37] This suggests that the FWHM used here is reasonable.

The nascent lineshapes recorded on the $Q_1(2)$ absorption line do not show evidence of the slow reaction channel depicted in Figure 4.13. This is qualitatively in agreement with the data reported by Li *et al.* The Doppler profile widths are also comparable, though the data shown in their work has been deconvolved with their unspecified laser linewidth.[42] This suggests that the low rotational states are predominantly formed from the fast channel. Additionally, previous measurements[42] have shown that the slow channel possesses a greater amount of rotational energy than the fast channel,also suggesting that the low N fragments are produced in conjunction with the fast channel.

4.10.2 Translational relaxation

An advantage of continuous-wave absorption spectroscopy as a probe of nascent fragments is the ease of recording the complete temporal evolution of the signal, whereas this would be achieved by varying the delay between the photolysis laser and the LIF pumping laser in multiple LIF experiments. The example spectra in Figure 4.17 shows a single experiment's

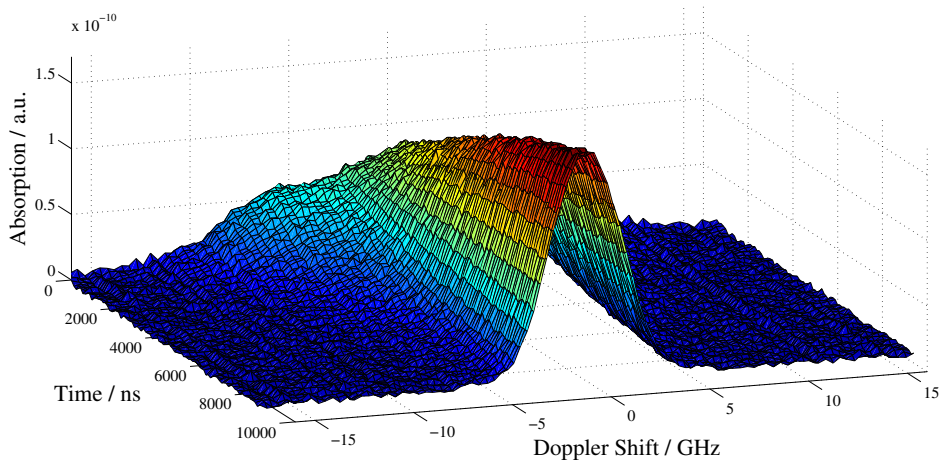

Figure 4.17: 3D plot displaying the lineshape narrowing towards a FWHM described by a thermal velocity distribution of the nascent OH fragments undergoing translational relaxation.

output with the probe laser stepped across the transition, along the Doppler Shift axis, and the time post photolysis averaged over 100 photolysis laser shots. From Figure 4.17 it is possible to observe the lineshape thermalising. Previous work on similar apparatus has also recorded this translational relaxation.[52]

The translational relaxation rate is estimated by taking time slices of the recorded spectra and approximating the experimental lineshape to a Gaussian. The resulting FWHM, $w_G(t)$, are then fitted to an exponential decay in time, assuming a single rate constant for collision with the vapour according to:

$$w_G(t) = (w_G(t=0) - w_{G,thermal})e^{-k_{trans}[\mathrm{HNO_3{:}H_2O}]t} + w_{G,thermal}, \qquad (4.26)$$

where $w_{G,thermal}$ is the thermal Gaussian width, calculated to be 2.92 GHz.

An example of data fitted in this way is shown in Figure 4.18. The first point of interest is that the thermal width, $w_{G,\mathrm{thermal}} \approx 4$ GHz, does not appear to reach the expected Doppler width of 2.92 GHz in any of the measurements. This is probably due to heating effects from the large amount of energy entering the reaction cell due to the near total absorption of the 193 nm photolysis beam. This effect is difficult to verify since the

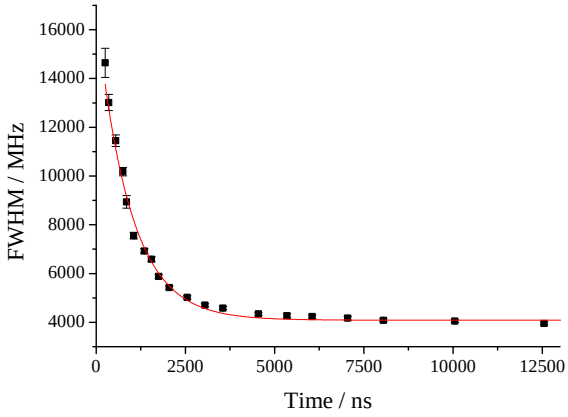

Figure 4.18: An example of the temporal decay of the FWHM of the OH lineshape shown in Figure 4.17.

OH diffuses out of the beam path over time and the frequency response of the AC-coupled detection is restricted such that the slow variation in the Doppler width at late times is unobservable. The extrapolated nascent FWHM, $w_G(t = 0) = 16.75 \pm 0.83$ GHz, agrees well with the literature, as discussed above.

In order to determine the rate constant for the thermalisation of OH the measurements were repeated at various pressures of the moist nitric acid vapour. To avoid total absorption of the photolysis beam these pressure were kept below 100 mTorr. The thermalisation rate was determined for each measurement from an exponential decay of the FWHM with the time post photolysis and the linear variation of these rate constants with pressure returned k_{trans}. The returned rate constant of $k_{\text{trans}} = (3.85 \pm 1.06) \times 10^{-10}\text{cm}^3\text{molecule}^{-1}\text{s}^{-1}$, in good agreement with similar experiments using a frequency mixing scheme which found $k_{\text{trans}} = (2.9 \pm 0.3) \times 10^{-10}\text{cm}^3\text{molecule}^{-1}\text{s}^{-1}$ on the $Q_2(2)$ transition in the same band. In the same work, the translational relaxation rate constants were typically around 1-3.5 $\times 10^{-10}$ cm^{3}molecule^{-1}s^{-1} over the $N = 1 - 7$ range of rotational states.[52] These values are fairly typical for translational relaxation: Matsumi *et al.* measured the relaxation of O(^1D) formed from 157 nm photolysis of O_2 with various collision partners (the rare gases, N_2 and O_2) using LIF and found values in the $1 - 2 \times 10^{-10}$ cm^{3}molecule^{-1}s^{-1} range; and Cline *et al.* found the relaxation rate constant of I($^2P_{1/2}$) from photolysis of C_3F_7I at 266 nm, using C_3F_7I and He as a bath gas,

to be $2.4 \pm 0.1 \times 10^{-10}\,\mathrm{cm^3 molecule^{-1} s^{-1}}$ using a similar technique to the time resolved near-infrared laser gain *vs.* absorption technique employed in Chapter 2.[53,54]

4.11 Conclusion and Future Work

It has been demonstrated that the spectrometer used in this work is capable of probing nascent OH photofragments. The next stage is to assess the full scope of information available. For example: the work described in this chapter has shown that the spectrometer can be used to record Doppler profiles, and it would be interesting to undertake a comprehensive study of the nascent Doppler profile of OH fragments in order to determine the spectrometer's sensitivity for measurements of angular momentum polarisation.

The experimental data presented in this chapter has been modeled using a speed-averaged literature value of β. These simulated nascent line profiles compared well with the experimental data measured in this work using counter propagating pump-probe geometries. As the next step towards measuring the translational anisotropy, the pump and probe geometry should be arranged so that the beams cross each others paths at 90°. This geometry yields a different lineshape, and has a different sensitivity to the recoil anisotropy from the geometries employed in this work, allowing β to be determined. Initial measurements with the new UV source utilised the laser geometries discussed above; however, a new reaction cell has recently become available and will allow improved measurement of the recoil anisotropy.

The narrow-bandwidth of the UV source generated by frequency mixing is one of its major advantages over LIF and spectroscopic measurements used pulsed laser light. In the case of nitric acid photolysis, the fast OH fragments produce broad lines in the counter-propagating experimental geometries used in this work, with lineshapes significantly broader than typically laser linewidths. The narrow-bandwidth UV source is ideally suited to probing slower OH fragments, as demonstrated earlier, since even room temperature OH radicals have Doppler widths two orders of magnitude greater than our instrument's resolution. However, since OH is such a light molecule, photolysis of any parent molecule tends to produce a fast OH fragment.

Another advantage of the current spectrometer, particularly for studying OH photoproducts, is that it employs an absorption technique. As discussed above, OH begins to

predissociate at high rotational energy levels and in excited vibrational states, making fluorescence techniques unsuitable. This predissociation occurs because the $^2\Sigma^+$ excited state is crossed by the dissociative $^4\Sigma^-$ state near the $\nu = 3$ vibrational level, as illustrated in Figure 4.19. With an appropriately selected near-infrared diode laser, nascent spectra of these states can be recorded, allowing determination of the excited state lifetimes in addition to the information provided by the nascent line profile. This data cannot be measured with LIF due to the short lifetime of the excited states, i.e. $\tau < 23\,\text{ps}$ for $\nu = 4$, $N = 0 - 7$, measured using UV-IR double resonance by Derro *et al.*[55]

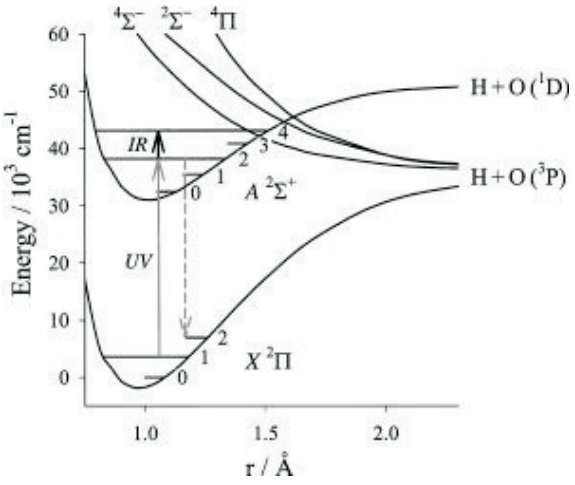

Figure 4.19: The OH PES involved in the $\tilde{A} - \tilde{X}$ transition and the dissociative curve crossings reproduced from Derro *et al.*.[55]

The limitation of our spectrometer is still the sensitivity, especially in comparison to LIF. This is illustrated by initial studies that were conducted on H_2O_2. The absorption cross section of H_2O_2 at 193 nm is $5.7 \times 10^{-19}\text{cm}^2\text{molecule}^{-1}$,[56] a factor of 30 lower than nitric acid ($1.6 \times 10^{-17}\text{cm}^2\text{molecule}^{-1}$). However, for the systems studied, this is mitigated by the fact that photodissociation of hydrogen peroxide generates two OH radicals, and the quantum yield of OH from nitric acid is $\Phi(\text{OH}) \approx 0.5$. The rotational distribution following 193 nm photolysisof H_2O_2 is reasonably hot, peaking around $N = 12$,[57] which presents an issue for the current spectrometer, as the low N states accessible are only marginally populated. Some initial measurements were attempted on the $Q_1(2)$ transition in analogous fashion to the nitric acid experiment. The data are shown in Figure 4.20. There was essentially no signal below 1 µs and the large absorption seen after this time is

already near-thermal, with FWHM= 3.3 ± 0.03 GHz.

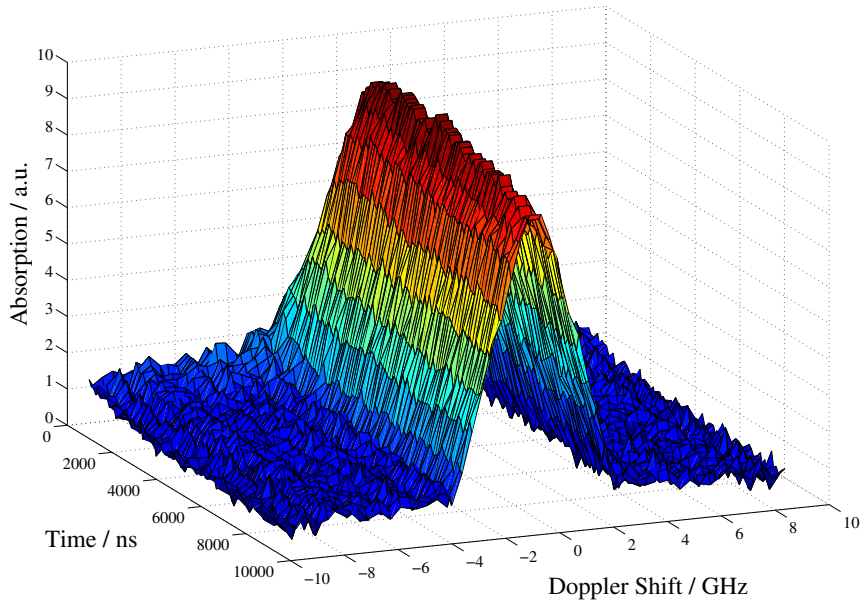

Figure 4.20: 3D plot displaying the initial results of the $Q_1(2)$ OH absorption transition following photolysis of H_2O_2 at 193 nm. Flow pressures were around 100 mTorr and increasing the pressure did not introduce any early time signals.

Recently, Chang *et al.*[58] have measured the orientation of the OH fragment following photolysis of hydrogen peroxide at 193 nm and 248 nm over a range of rotational states using LIF and Zeeman quantum beat spectroscopy. Whilst with our present spectrometer it is possible to observe the $N = 2$ state, it is not possible to observe the high N states. It appears that these high N states are also oriented. The orientation moments recorded by Chang *et al.* are reproduced in Figure 4.21 to illustrate this.[58] It would be possible to replace the 730 nm diode laser in our current spectrometer with a 780 nm diode laser, which would allow access to these high N states.

The study of hydrogen peroxide photolysis appears to represent a logical progression for this spectrometer: it produces an OH number density large enough to be detected; the OH product rotational angular momentum is known to be oriented; and the dissociation produces rotationally hot fragments which may display signs of predissociation in the absorption spectrum. However, the studies of H_2O_2 photolysis will require altering the

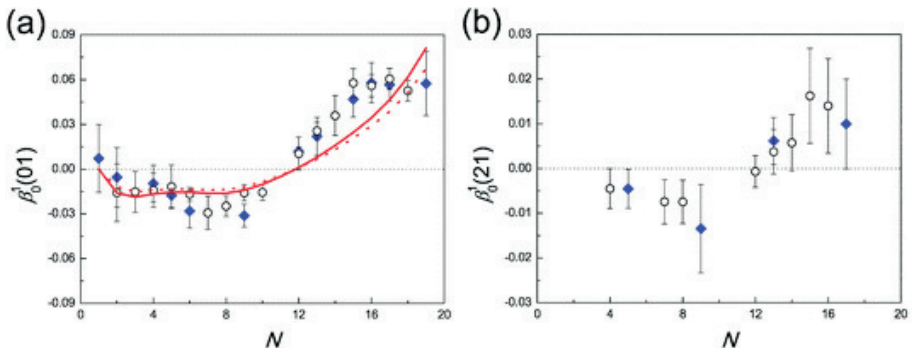

Figure 4.21: The orientation bipolar moments following photolysis of H_2O_2 at 193 nm reproduced form Chang *et al.*[58]

spectrometer to include a 780 nm laser diode instead of the current 730 nm laser diode.

Earlier results in this chapter presented the application of wavelength modulation to reduce the noise in the signal. The higher frequency counterpart of WMS, known as frequency modulation spectroscopy, is applied to nascent photoproducts, in particular those of the CN radical, in the next chapter.[30,59–63] In principle, frequency-modulation could be incorporated into the spectrometer, with frequency modulation of the near-infrared diode laser propagating through the sum frequency mixing scheme to generate frequency modulated UV radiation. However, this requires a significant amount of power to reach the detector, which may not be possible with the 3 μW generated here.

The next chapter illustrates the application of a frequency-modulated near-infrared diode laser to the A-X electronic transition in the nascent CN fragment following photolysis of ICN. The relationship between the recoil velocity, rotational angular momentum and dipole moment of the parent fragment is explored and highlights the exquisite details of the photodissociation process provided by laser spectroscopy.

References

[1] A. M. Holloway and R. P. Wayne, *Atmospheric Chemistry*, Royal Society of Chemistry, 2010.

[2] D. E. Heard and M. J. Pilling, Chemical reviews **103**, 5163 (2003).

[3] E. L. Baardsen and R. W. Terhune, **209**, 21 (1972).

[4] D. Mihelcic et al., Pure and Applied Geophysics PAGEOPH **116**, 530 (1978).

[5] C. C. Felton, J. C. Sheppard, and M. J. Campbell, Nature **335**, 53 (1988).

[6] M. J. Campbell, J. C. Sheppard, and B. F. Au, Geophysical Research Letters **6**, 175 (1979).

[7] C. C. Felton, J. C. Sheppard, and M. J. Campbell, Environmental Science & Technology **24**, 1841 (1990).

[8] U. Platt, M. Rateike, W. Junkermann, J. Rudolph, and D. H. Ehhalt, Journal of Geophysical Research **93**, 5159 (1988).

[9] G. H. Mount, Journal of Geophysical Research **97**, 2427 (1992).

[10] H.-P. Dorn, U. Brandenburger, T. Brauers, and M. Hausmann, Journal of the Atmospheric Sciences **52**, 3373 (1995).

[11] T. Brauers, M. Hausmann, A. Bister, A. Kraus, and H.-P. Dorn, Journal of Geophysical Research **106**, 7399 (2001).

[12] H.-P. Dorn, R. Neuroth, and A. Hofzumahaus, Journal of Geophysical Research **100**, 7397 (1995).

[13] J. M. Brown and A. Carrington, *Rotational Spectroscopy of Diatomic Molecules*, Cambridge Molecular Science Series, Cambridge University Press, 2003.

[14] K. Herzberg, G. and Huber, *Molecular spectra and molecular structure. I. Spectra of diatomic molecules*, Van Nostrand Reinhold, second edition, 1957.

[15] M. Mazurenka, A. J. Orr-Ewing, R. Peverall, and G. A. D. Ritchie, Annual Reports Section "C" (Physical Chemistry) **101**, 100 (2005).

[16] G. M. G. Berden, Rudy Peeters, International Reviews in Physical Chemistry **19**, 565 (2000).

[17] J. M. Herbelin et al., Applied optics **19**, 144 (1980).

[18] H. Willman, *Chapter 4 - OH*, PhD thesis, 2010.

[19] C. A. Smith, F. D. Pope, B. Cronin, C. B. Parkes, and A. J. Orr-Ewing, The Journal of Physical Chemistry A **110**, 11645 (2006).

[20] M. B. Crow et al., The Journal of Physical Chemistry A **113**, 6689 (2009).

[21] C. Tatum Ernest, D. Bauer, and A. J. Hynes, The Journal of Physical Chemistry A **116**, 5910 (2012).

[22] C. M. Western, PGOPHER, a Program for Simulating Rotational Structure.

[23] G. Hancock and V. Kasyutich, Applied Physics B **79**, 383 (2004).

[24] V. L. Kasyutich, The European Physical Journal D **33**, 29 (2005).

[25] B. Shirinzadeh, D. M. Bakalyar, and C. C. Wang, The Journal of Chemical Physics **82**, 2877 (1985).

[26] R. Engleman, Journal of Quantitative Spectroscopy and Radiative Transfer **9**, 391 (1969).

[27] A. Yariv and P. Yeh, *Photonics: Optical Electronics in Modern Communications*, The Oxford Series in Electrical and Computer Engineering, Oxford University Press, USA, 2006.

[28] M. Keshner, Proceedings of the IEEE **70**, 212 (1982).

[29] G. C. Bjorklund, Optics Letters **5**, 15 (1980).

[30] G. E. Hall and S. W. North, Annual review of physical chemistry **51**, 243 (2000).

[31] J. M. Supplee, E. A. Whittaker, and W. Lenth, Applied Optics **33**, 6294 (1994).

[32] J. Reid and D. Labrie, Applied Physics B Photophysics and Laser Chemistry **26**, 203 (1981).

[33] J. A. Silver, Applied optics **31**, 4927 (1992).

[34] P. Kluczynski, J. Gustafsson, A. M. Lindberg, and O. Axner, Spectrochimica Acta Part B: Atomic Spectroscopy **56**, 1277 (2001).

[35] M. L. Hamilton, R. Peverall, G. A. D. Ritchie, L. J. Thornton, and J. H. Helden, Applied Physics B **97**, 715 (2009).

[36] A. Foltynowicz, F. Schmidt, W. Ma, and O. Axner, Applied Physics B **92**, 313 (2008).

[37] J. August, M. Brouard, and J. P. Simons, Journal of the Chemical Society, Faraday Transactions 2 **84**, 587 (1988).

[38] A. A. Turnipseed, G. L. Vaghjiani, J. E. Thompson, and A. R. Ravishankara, The Journal of Chemical Physics **96**, 5887 (1992).

[39] M. Brouard, S. Duxon, P. A. Enriquez, and J. P. Simons, Journal of the Chemical Society, Faraday Transactions **89**, 1435 (1993).

[40] G. Leu, Chemical Physics Letters **257**, 481 (1996).

[41] F. Assenmacher, M. Gutmann, F. Noack, V. Stert, and W. Radloff, Optik **390**, 385 (2000).

[42] Q. Li, R. T. Carter, and J. Huber, Chemical Physics Letters **334**, 39 (2001).

[43] P. Felder, X. Yang, and J. Robert Huber, Chemical Physics Letters **215**, 221 (1993).

[44] T. L. Myers, N. R. Forde, B. Hu, D. C. Kitchen, and L. J. Butler, The Journal of Chemical Physics **107**, 5361 (1997).

[45] J. R. Huber, Chemphyschem : a European journal of chemical physics and physical chemistry **5**, 1663 (2004).

[46] A. Schiffman and D. D. Nelson, Computer **98**, 6935 (1993).

[47] A. Jacobs, K. Kleinermanns, H. Kuge, and J. Wolfrum, The Journal of Chemical Physics **79**, 3162 (1983).

[48] J. Schlütter and K. Kleinermanns, Chemical Physics Letters **192**, 94 (1992).

[49] D. C. McCabe et al., The Journal of Physical Chemistry A **107**, 7762 (2003).

[50] Y. Bai and G. A. Segal, The Journal of Chemical Physics **92**, 7479 (1990).

[51] G. L. Wilson and F. D. Miles, Transactions of the Faraday Society **35**, 356 (1940).

[52] L. J. Russell, *Studies in Gas Phase Chemistry with Diode Lasers*, PhD thesis, 2010.

[53] Y. Matsumi, S. M. Shamsuddin, Y. Sato, and M. Kawasaki, The Journal of Chemical Physics **101**, 9610 (1994).

[54] J. I. Cline, C. A. Taatjes, and S. R. Leone, The Journal of Chemical Physics **93**, 6543 (1990).

[55] E. L. Derro et al., The Journal of chemical physics **122**, 244313 (2005).

[56] C. L. Lin, N. K. Rohatgi, and W. B. DeMore, Geophysical Research Letters **5**, 113 (1978).

[57] A. Jacobs, M. Wahl, R. Weller, and J. Wolfrum, Applied Physics B Photophysics and Laser Chemistry **42**, 173 (1987).

[58] Y.-P. Chang, M. Brouard, R. Cireasa, T. Perkins, and S. A. Seamons, Physical chemistry chemical physics : PCCP **13**, 8213 (2011).

[59] S. W. North, X. S. Zheng, R. Fei, and G. E. Hall, The Journal of Chemical Physics **104**, 2129 (1996).

[60] M. L. Costen, S. W. North, and G. E. Hall, The Journal of Chemical Physics **111**, 6735 (1999).

[61] M. L. Costen and G. E. Hall, Physical Chemistry Chemical Physics **7**, 1408 (2005).

[62] M. L. Costen and G. E. Hall, Physical chemistry chemical physics : PCCP **9**, 272 (2007).

[63] G. Hancock et al., Molecular Physics **108**, 1083 (2010).

Chapter 5

Vector Correlations in ICN Photodissociation at 266 nm

In this chapter nascent line profiles of CN fragments from 266 nm photolysis of ICN are measured, allowing both the recoil anisotropy and the alignment and orientation of the ground and first excited vibrational energy level of the CN fragments to be determined. This chapter presents the first study of vibrationally excited CN fragments formed following 266 nm photolysis of ICN and the information that this reveals about the dissociation process.

5.1 Introduction

In Chapter 1, the general interest in photodissociation dynamics and the importance of understanding potential energy surfaces was discussed; in this chapter the focus turns to measuring vector properties of the CN fragment from ICN photodissociation at 266 nm and the insight this gives into the behaviour of the excited states during bond fission.

Diatomics such as Cl_2 and ICl have been the subject of many photodissociation studies. The restricted number of degrees of freedom coupled with the small number of products which are easily detected with conventional nanosecond pulsed laser studies (since there are no rotational or vibrational degrees of freedom for an atom), allows in depth study.[1–6] As a (simple) triatomic molecule, ICN is a natural step in the evolution of understanding and therefore has been extensively studied both experimentally and theoretically.[7–19] Interestingly, measurements of the nascent CN product from ICN photolysis provided the

first example of *orientation* in a molecular fragment, i.e. a preference for a vector to have direction, as discussed in depth in Chapter 1.[10] Orientation of the electronic angular momentum in atomic fragments had previously been observed.[20]

The previous experimental studies of ICN have mostly focused on the application of laser induced fluorescence (LIF) to the detection of the CN fragment, utilizing the B $^2\Sigma^+$ - X $^2\Sigma^+$ electronic transition in the ultraviolet region of the electromagnetic spectrum. However, more recently CN photofragments were the test case for probing a molecular fragment by using frequency modulated radiation to enhance the sensitivity of absorption spectroscopy. This allowed North *et al.* to investigate the A $^2\Pi$ - X $^2\Sigma^+$ electronic transition of the CN fragment, which occurs in the near-infrared.[21] This technique has since been applied to ICN photolysis with a large degree of success, as discussed below.[17–19,22] Investigation of the A $^2\Pi$ - X $^2\Sigma^+$ transition, rather than the B $^2\Sigma^+$ - X $^2\Sigma^+$, presents many advantages: the narrow-band nature of near-infrared radiation, compared with the broader bandwidth of pulsed UV sources, reduces the contribution of the laser linewidth to the experimental signal, as has been seen before in this thesis. In the specific case of CN, the A - X transition allows Q branches to be investigated, whereas the B - X does not. As discussed in Chapter 1, the Q branch has different sensitivity to the polarisation of angular momenta than the P or R branch, which have the same dependence in the high rotational quantum numbers studied here (see Appendix A. Therefore, having Q transitions in addition to P and R transitions for one rotational state allows improved fitting by simultaneously fitting to both Q and P or R branches, as discussed below.

This work focusses on the orientation of the CN fragment following photolysis of ICN at 266 nm. Measurements of the orientation and alignment of the ground vibrational state are compared with the work of Costen and Hall[17,18] before investigating the first excited vibrational state. As will be shown, coherent orientation of the $v = 1$ state is observed, but of opposite sign to the orientation of the $v = 0$ state from 248 and 266 nm photolysis.

5.2 ICN Photolysis

The photolysis of ICN in the $\tilde{A}$ band, between 200 nm and 320 nm, has two distinct electronic exit channels:

$$\mathrm{ICN} + h\nu \rightarrow \mathrm{I}(^2P_{3/2}) + \mathrm{CN}(X\ ^2\Sigma^+) \tag{5.1}$$

$$\mathrm{ICN} + h\nu \rightarrow \mathrm{I}(^2P_{1/2}) + \mathrm{CN}(X\ ^2\Sigma^+) \tag{5.2}$$

where $\mathrm{I}(^2P_{3/2})$ is the ground electronic state and $\mathrm{I}(^2P_{1/2})$ the excited electronic state, hereafter denoted I and I* respectively. The photolysis proceeds *via* excitation to three excited state potential energy surfaces, as seen in Figure 5.1a, forming a coherent superposition of two or more of these surfaces. The resulting wave packet experiences interference effects between the potential energy surfaces as it travels towards the product asymptote, thereby generating the orientation of rotational angular momentum, as discussed in Chapter 1. The three PESs accessed by the $\tilde{A}$ are the $^1\Pi_1$, $^3\Pi_{0+}$ and $^3\Pi_1$, states. The $^3\Pi_{0+}$ surface is diabatically correlated with the I* product, and the $^1\Pi_1$ and $^3\Pi_1$ surfaces are diabatically correlated to the I product. The $^1\Pi_1$ surface is purely repulsive, leading to the I product whilst the other two surfaces have shallow minima. These features are summarised in Figure 5.1b.[14]

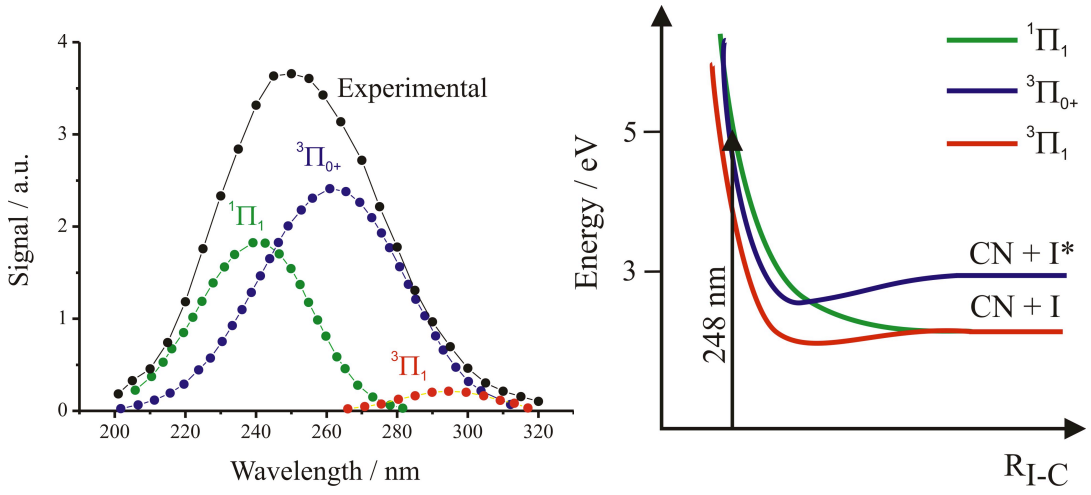

(a) $\tilde{A}$ band (b) PES of the $\tilde{A}$ band

Figure 5.1: The PESs constituting the ICN $\tilde{A}$ Band.[14,23]

Previous experimental results[17] and theory[14] have confirmed that photolysis around the centre of the $\tilde{A}$ band proceeds through a coherent excitation of parallel and perpendicular transitions, with a larger contribution of $\approx 85\%$ from the parallel transition.[8] A parallel transition from the ground state accesses the $^3\Pi_{0+}$ surface, whereas the $^3\Pi_1$ state is accessed by a perpendicular transition, and the contribution of the $^3\Pi_1$ state to the A $^2\Pi$ - X $^2\Sigma^+$ transition is essentially zero at 266 nm. In addition to this, there exists a conical intersection between the $^3\Pi_{0+}$ and $^1\Pi_1$ surfaces, which allows CN to be formed in combination with I products from either parallel or perpendicular transitions. These effects manifest themselves as a significant deviation from the limits of the recoil anisotropy expected for a pure parallel or perpendicular transition for both the I and I* fragments.[17]

During the photodissociation process the C–N bond acts as a spectator, with the vibrational population of the parent propagating through to the product.[14] This results in a very cold vibrational distribution, with more than 98% of the population in the vibrational ground state.[24]

The rotational distribution for the $v = 0$ level is generally described as bimodal for all the CN products of $\tilde{A}$ band photolysis of ICN.[17,25] This bimodal distribution correlates with the formation of I and I* products, as shown for 266 nm photolysis in Figure 5.2. Due to energy constraints CN fragments with the highest rotational energy can only be formed in conjunction with ground state iodine, whereas the lowest rotational energy CN fragments are produced mostly in combination with electronically excited iodine due to the surfaces involved, as discussed below. This interesting result of a rotationally hot fragment from a linear parent molecule is due to the topology of the PESs as they approach the products. In the Franck-Condon (FC) region all the excited states have energy minima at significantly bent geometries, as shown in Figure 5.3a, thus upon excitation the linear ICN molecule begins to bend. Upon bending the symmetry of the molecule is reduced from $C_{\infty v}$ to C_s, hence the descent in symmetry indicated in Figure 5.3a. At the conical intersection there is a preference for a linear geometry for the $^3\Pi_{0+}$ and $^3\Pi_1$ surfaces, with a small preference for bent geometries for the $^1\Pi_1$ surface. Amatatsu *et al.*[14] followed a trajectory initially starting on the $^3\Pi_{0+}$ surface, the main surfaces accessed at 266 nm, where the zero point energy of the bending vibration is amplified by the $^3\Pi_{0+}$ surface's preference for bent geometries, giving the CN fragment a large amount of rotational energy

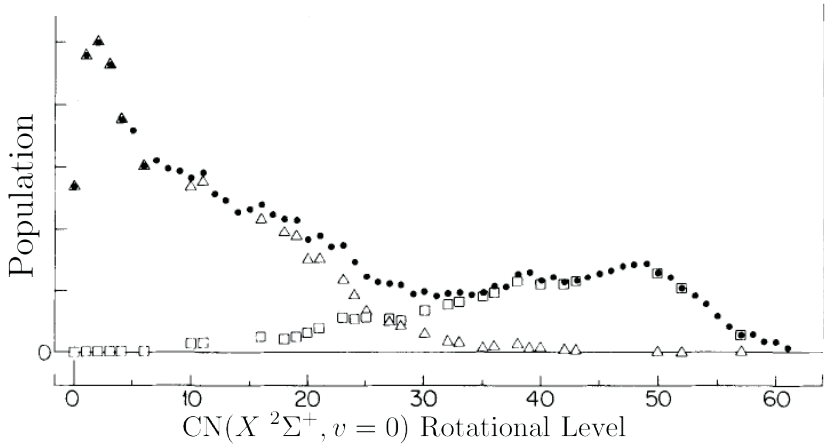

Figure 5.2: Rotational distribution of the vibrational ground state of CN following photolysis at 266 nm, the solid dots show the overall distribution with the △ and □ corresponding to I* and I, respectively. Reproduced from Nadler *et al.*.[24]

on approach to the conical intersection. At the conical intersection, rotational energy increases the coupling between the surfaces, therefore transfer onto the $^1\Pi_1$ surface to generate I fragments maintains the rotational energy, whereas continuation on the $^3\Pi_{0+}$ to generate I* products occurs with lower rotational energy, hence the lower rotational states are formed mainly in coincidence with I*. In addition to this, Amatatsu *et al.* found that the trajectories all proceed along the bottom of the C–N coordinate of the PESs, and thus do not involve excitation of the C–N stretch.[14]

The above discussion accounts for the observed rotational and vibrational distribution found in the products. The recoil anisotropy was also measured in these studies, and the recorded values were found to deviate significantly from the limiting cases, showing an I*/I dependence but not a rotational state dependence.[9,24] This was attributed to the three potential energy surfaces and conical intersection later treated theoretically by Amatatsu *et al.*[14] Similar studies using LIF to probe the rotational structure following 248 nm, 266 nm and 281.5 nm photolysis found that the spin channels, $F_1(J = N+1/2)$ and $F_2(J = N-1/2)$ discussed below, have unequal populations with a dependence on rotational level, N, which was attributed to interference effects between dissociation channels.[7] Further investigation of the products of 248 nm photolysis, using circularly polarised LIF to record the velocity averaged orientation, found that the degree of orientation varies with rotational quantum

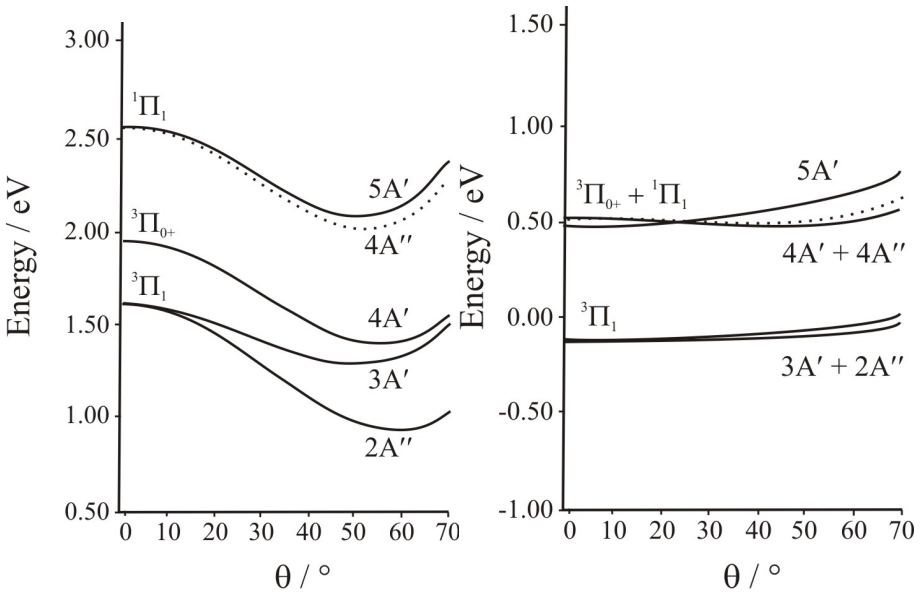

(a) FC region (b) Conical intersection

Figure 5.3: Variation of the PES with the bending angle, θ, of ICN at (5.3a) the FC region and (5.3b) the conical intersection taken from the literature.[14]

number as a result of the I^*/I branching ratio, shown in Figure 5.4.[10] Interestingly, later experiments found that the $v = 2$ excited state was also oriented, though of opposite sign to the $v = 0$ products.[11]

These early studies all focused on photolysis in the centre of the $\tilde{A}$ band, either at 248 nm or 266 nm, and utilised LIF to probe the CN fragment *via* the B–X transition. The more recent work of Costen *et al.* explored the photolysis wavelength dependence of the $\tilde{A}$ band using FM spectroscopy to probe the CN fragment *via* the A–X transition.[17] Costen *et al.* recorded the nascent line profiles over a range of CN rotational states following photolysis of ICN at 222 nm, 248 nm, 266 nm, and 308 nm. They were able to resolve both spin channels and fit line profiles to CN fragments produced in conjunction with both I and I*. Their fits returned the alignment of the velocity and the rotational angular momentum, parameterised using Dixon's bipolar moment formalism discussed in Chapter 1, and showed that the dynamics vary only slightly across the $\tilde{A}$ band. The CN fragment associated with I fragments displayed a recoil anisotropy reduced from limiting but positive, $2 > \beta > 1$. Similarly, the CN fragment associated with I* fragments displayed

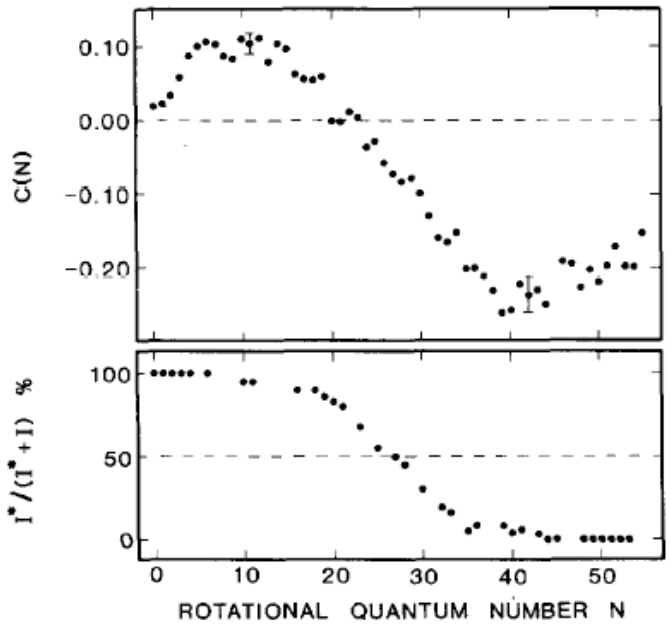

Figure 5.4: The normalised difference in intensity of data obtained with left circularly polarised and right circularly polarised light, C(N), as a function of rotational quantum number and the I* branching ratio, reproduced from Hasselbrink *et al.*[10] with the I* branching ration take from Nadler *et al.*[24]for the photolysis of ICN at 248 nm.

a positive β, but smaller than that measured for the I co-fragment. These observations are consistent with photolysis largely occurring *via* a parallel transition to the $^3\Pi_{0+}$ surface at all photolysis wavelengths.[17] Following this study, Costen and Hall[18] applied FM spectroscopy to measuring the orientation of the $v = 0$ CN fragments produced by photolysis at 248 nm and 266 nm, introducing new bipolar moments to account for the orientation observed by Black *et al.*.[11] As before, Costen and Hall reported a comprehensive selection of rotational states across the two spin-orbit channels and formed in association with I and I* products; the observed orientation demonstrated a rotational state dependence, as reported by Hasselbrink *et al.*,[10] and the CN formed in conjunction with I is oppositely oriented to CN formed with I*, as reported by Black *et al.*[11].[18]

The wealth of literature on ICN photolysis has focused primarily on the ground vibrational state of the CN fragment,[7–10,12,17,18] with the exception of Black *et al.* who reported orientation for the $v = 2$ products.[11] Recently, Hancock *et al.*[19] have reported the angular momentum polarisation for both the $v = 0$ and $v = 1$ vibrational levels of CN produced by 248 nm photolysis, determined using FM spectroscopy to record the nascent

lineshapes. In their work they found the ground vibrational level to be oriented, with the measured orientation moments in excellent agreement with Costen and Hall, however the first excited vibrational level displayed no orientation over the rotational states measured ($N = 38, 44, 48, 51$ & 52).[19] In addition to this, the alignment moments reported by Hancock *et al.* are comparable with those of Costen *et al.* for the $v = 0$ level,[17] and the alignment moments determined for the $v = 1$ level are comparable with those of the $v = 0$, revealing that the incoherent dynamics leading to the $v = 1$ products are very similar to those of the $v = 0$ products, despite the difference in the coherent dynamics demonstrated by the orientation.

5.3 CN Spectroscopy

The ground-state orbital configuration of the CN radical is: $2s\sigma^2 2s\sigma^2 2p\pi^4 2p\sigma^1$. It has a projection of total orbital angular momentum along the bond of zero and a spin of one half due to the lone electron, hence the term symbol $^2\Sigma^+$. The coupling of the spin and rotational angular momentum in the high rotational energy levels investigated in this work is described by Hund's case (b), in which the spin, S, couples to the rotational angular momentum, N, such that the total angular momentum is described by $J = N+S, N+S-1, \ldots |N-S|$. Since $S = 1/2$, the total angular momentum may either be $J = N + 1/2$ (F_1) or $J = N - 1/2$ (F_2). The splitting of the X state rotational levels is shown in Figure 5.5 where the parity of the rotational levels is given by $(-1)^N$.

The first excited state of CN lies 2.26 eV above the ground state, and has the orbital configuration: $2s\sigma^2 2s\sigma^2 2p\pi^3 2p\sigma^2$. The A state therefore has a total orbital angular momentum projection quantum number of $\Lambda = 1$ and an unpaired spin, hence the terms symbol $^2\Pi_{3/2}$ and $^2\Pi_{1/2}$.[26] As above with the X state, the A state is best described by Hund's case (b) for the states probed in this work. Similarly to the OH X($^2\Pi$) state, the non-zero orbital angular momentum couples to the rotation, splitting the rotational energy levels into Λ-doublets, differentiated by the parity of the wavefunction upon reflection in the rotational plane. These splittings are shown (greatly exaggerated) in Figure 5.5.[26]

The rotational fine structure observed in the A $^2\Pi$ - X $^2\Sigma^+$ transition is very similar to that discussed in Chapter 4, for OH with the same selection rules applying. The same notation as for the OH rotational transition is used here, though the satellite transitions

are neglected due to their weak transition strength. In Chapter 4 the $v = 0 \rightarrow v = 0$ vibrational band was probed, in this work the $v = 0 \rightarrow v = 2$ and $v = 1 \rightarrow v = 3$ bands have been used, sometimes called the (2,0) and (3,1) bands, respectively. The absorption transitions used in this work are too weak to be observed directly above the background noise. However, as discussed in the previous chapter, modulation techniques can improve the signal to noise significantly, and a technique similar to wavelength modulation was implemented here.

5.4 Frequency Modulation Spectroscopy

The technique of frequency modulation (FM) spectroscopy provides enhanced sensitivity over direct absorption while maintaining the fast time response associated with single pass absorption. FM is implemented by sinusoidally modulating the frequency of an electromagnetic wave. For diode lasers this is achievable either by directly modulating the laser current applied to the diode or by external modulation of the laser radiation using an electro-optic modulator (EOM). Direct modulation of the current applied to the diode laser often produces residual amplitude modulation, hence this work has used an EOM; the EOM consists of an electro-optic crystal which the diode laser is focused through, and a radio frequency signal generator is used to apply an electric field to the crystal, which leads to frequency modulation in the light passing though it. The electric field of the modulated light is given by:

$$E(t) = E_0 \exp[i(\omega_o t + M \sin \omega_m t)] \tag{5.3}$$

where $E(t)$ and E_0 are the electric field at time t and $t = 0$ respectively; ω_0 and ω_m are the laser frequency (or carrier frequency) and modulation frequency, respectively; and M is the modulation index. This may be written as a Fourier sum according to:

$$E(t) = E_0 \exp(i\omega_o t) \sum_{n=-\infty}^{+\infty} J_n(M) \exp(in\omega_m t), \tag{5.4}$$

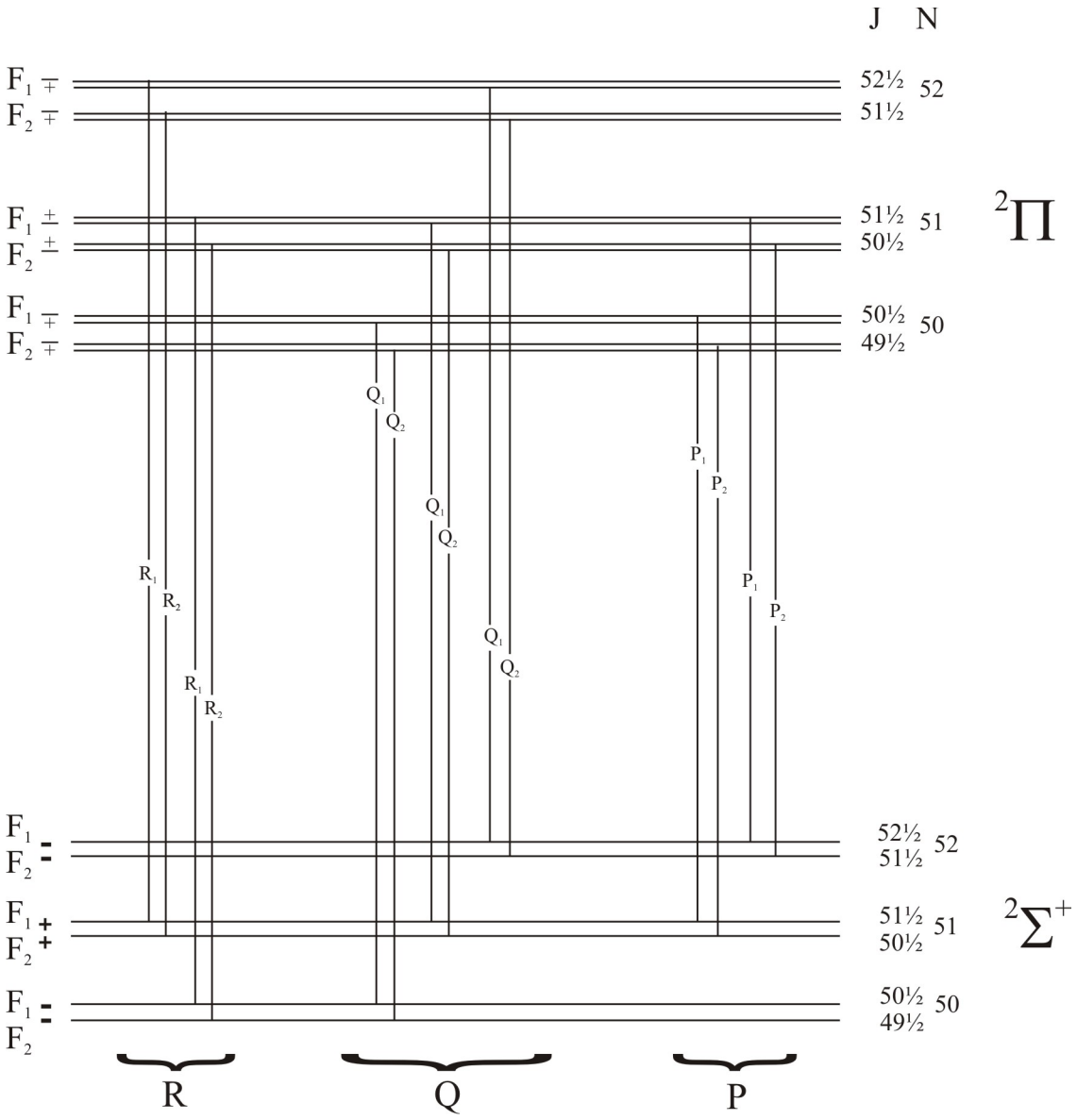

Figure 5.5: Rotational energy level diagram showing the A - X electronic transition of the CN radical.

where

$$J_n(M) = \sum_{\alpha=0}^{\infty} \frac{(-1)^m}{m!(\alpha+n+1)!} \left(\frac{\alpha}{2}\right)^{2\alpha+n} \tag{5.5}$$

and are Bessel functions.[27] This results in an electromagnetic wave with a sequence of frequency components (or sidebands), each separated from the carrier frequency by the modulation frequency, as shown in Figure 5.6 for a single set of sidebands, and with the n^{th} sideband having an amplitude given by the n^{th} order Bessel function of argument M, $J_n(M)$, given by equation 5.5. In the experiment detailed below, the modulation index was chosen such that the first order sidebands provided the major contribution to the FM spectra, with higher orders being negligible.

The modulation frequency is chosen to be comparable with the spectral feature's linewidth. This is in contrast to wavelength modulation spectroscopy, in which the modulation frequency is typically smaller than the spectral feature's linewidth, as discussed in Chapter 4. Moving detection into higher frequencies in this manner reduces the $1/f$ noise, thus increasing the sensitivity. In addition to this, it is possible to filter out signals not occurring at a harmonic of the modulation frequency, further improving sensitivity. Experimentally, the modulation frequency is limited by the response of the EOM; for the EOM used in this work the modulation frequency was limited to 400 MHz.

An example of how FM spectroscopy produces an FM absorption trace, A_{FM}, from an absorption profile, $g(\omega)$, is shown in Figure 5.6, where the central laser frequency, ω, sweeps across the profile and the difference in absorption of the two sidebands, one occurring at $\omega_0 + \omega_m$ and one at occurring at $\omega_0 - \omega_m$, is measured. This is illustrated mathematically by:[17]

$$A_{\mathrm{FM}} \propto g(\omega + \omega_m) - g(\omega - \omega_m). \tag{5.6}$$

Making use of the symmetry of the Bessel functions, $J_n(M) = (-1)^n J_n(M)$, it is known that the odd and even sidebands are in-phase and out of phase with the carrier frequency, respectively, thus FM spectroscopy is phase sensitive, and dispersion (the change in phase of an electromagnetic wave as it passes through a medium (D_{FM})) must be considered in addition to the absorption (the change in intensity of the wave as it passes through a medium (A_{FM})). Phase-sensitive detection at the modulation frequency, ω_m, reduces noise, and the signal will include dispersion-dependent terms.

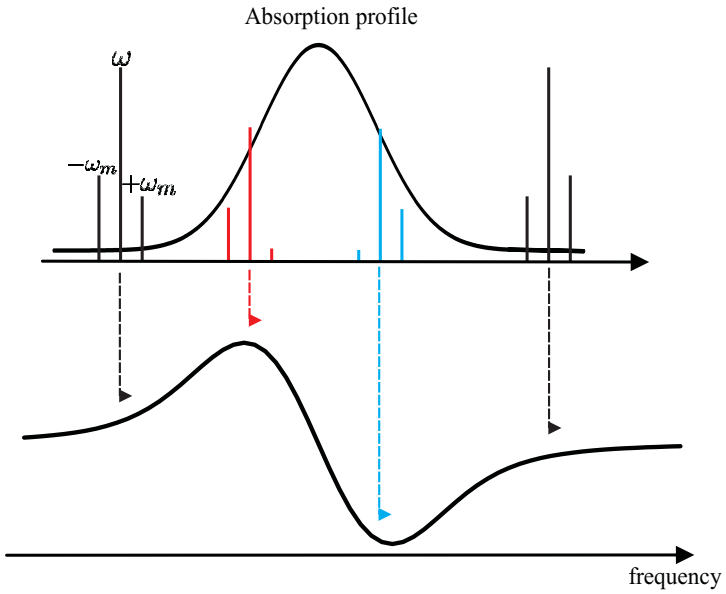

Figure 5.6: Scanning of the central laser frequency ω over an absorption profile with the resulting FM profile shown beneath. The two FM sidebands are shown at $+\omega_m$ and $-\omega_m$ and the resulting FM profile can be seen to be the difference in absorption between the two sidebands at each central laser frequency, ω.

In order to demodulate the detected signal and return the components oscillating at the modulation frequency an I and Q demodulator is used. The demodulated is a communication device which compares the detected signal with the modulation signal applied to the EOM, known as the reference signal. There is typically a phase difference between the reference and detected signals at the demodulator since they have traveled different distances; therefore, to account for this phase difference, the I and Q demodulator splits the detected signal into two signals, one of which is compared against the reference signal and the other of which is compared against a reference signal which is phase shifted by 90°. The two signals are known as the I-channel, I_{FM}, and Q-channel, Q_{FM}, respectively. The relationship of the I-channel and Q-channel to the absorption and dispersion profile are given by:

$$I_{\mathrm{FM}} = A_{\mathrm{FM}} \cos\theta + D_{\mathrm{FM}} \sin\theta \tag{5.7}$$

$$Q_{\mathrm{FM}} = A_{\mathrm{FM}} \sin\theta + D_{\mathrm{FM}} \cos\theta \tag{5.8}$$

in which θ is the phase difference or phase angle at the demodulator.

Using a known spectral feature, usually a Gaussian of a known width, such as a ther-

mally relaxed sample, the phase angle can then be determined from the I and Q signals and used on unknown spectra to convert these signals into pure absorption and dispersion profiles. The labels I and Q refer to *in-phase* and *quadrature*, respectively. An example of I and Q profiles and the resultant absorption and dispersion profiles is shown in Figure 5.7. This data were taken by integrating from 1.50 µs to 1.51 µs post photolysis on the P_1 $N = 50$ transition in the (2,0) band of CN produced in the 248 nm photolysis of ICN at a pressure of 60 mTorr.

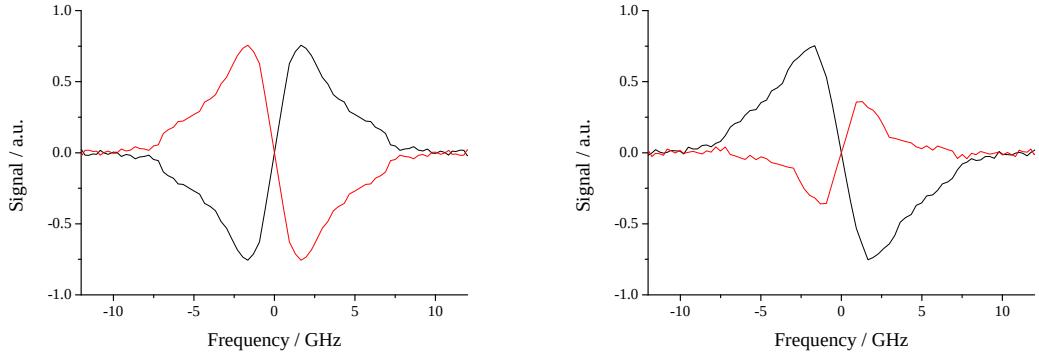

(a) I and Q (b) Absorption and dispersion

Figure 5.7: (a) Examples of I signal and Q signal in black and red, respectively; (b) the corresponding absorption and dispersion in black and red, respectively. The phase angle is $\theta = \frac{3\pi}{4}$.

The absorption profile generated through the isolation of the A_{FM} term from the above method is the FM absorption profile. While it is possible to convert these profiles into a direct absorption lineshape profile, it is not the method chosen here, since it is easier to convert the theoretical absorption profile into an FM profile and doing so introduces.The nascent absorption profiles have been fitted to the Doppler profiles introduced by Dixon[28] and adapted by Costen and Hall,[18] as detailed in Chapter 1 by equations 1.16 and 1.18, and also given in Appendix A by equations A.1 and A.5. These line shapes are convoluted with a Gaussian, to account for the recoil velocity distribution and the parent molecule's energy distribution, before being converted into FM line profiles to be fitted to the recorded spectra, as discussed below.

5.5 Experimental Features

The experiment was conducted using the experimental setup illustrated in Figure 5.8. Room temperature samples of ICN vapour were flowed through the reaction cell at pressures of approximately 40 mTorr, achieved by pumping the vapour pressure of solid ICN through the reaction cell. The 266 nm photolysis radiation was the fourth harmonic of a Nd:YAG laser (Continuum Powerlight 9020) operating at 20 Hz and directed through a PEM (Hinds Instruments PEM 90 F55 Optical Head) to allow polarisation control.

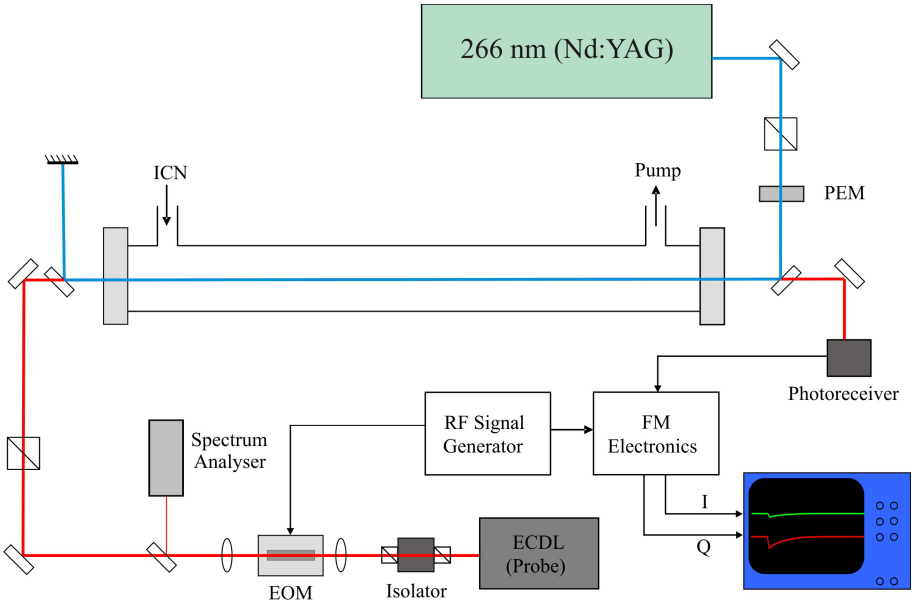

Figure 5.8: Experimental setup used to record nascent FM spectra.

The probe radiation was generated using an external cavity diode laser (Sacher Lasertechnik TEC 500), operating in the 825 nm – 875 nm wavelength region, and externally modulated using an electro-optic modulator (EOM, Quantum Technology Inc. 3500-P). The EOM modulated the laser light at 400 MHz while the laser frequency was stepped in discrete frequency steps, $\approx$ 100 MHz, across the spectral feature of interest. A scanning Fabry-Perot etalon (spectrum analyser) monitored the spectral output of the diode laser from a partial reflection taken after the EOM; this allowed calibration of a frequency scale.

The pump and probe beams were counter-propagated through the 150 cm long reaction cell and then separated, the pump beam was safely deposited into a beam dump while the probe beam was attenuated with a neutral density filter and focused onto a fast InGaAs

photodiode (1 GHz New focus). The output from the photodiode was amplified using two 500 MHz amplifiers (Minicircuits ZFL-500LN) and demodulated in an RF demodulator circuit (Pulsar Microwave) with reference to the rf signal applied to the EOM. The resulting pair of signals, the In-phase (I) and Quadrature (Q), were filtered using 39 MHz in-line filters (Minicircuits SLBP-39), which removed noise at the modulation frequency and its other harmonics, and recorded using a digital storage oscilloscope (LeCroy Waverunner 6100A, 1 GHz bandwidth). The frequency stepping of the laser, communication with the spectrum analyser and transfer of data from the oscilloscope were all managed in a MATLAB program which communicated with the oscilloscope *via* a local area network and all other equipment *via* a 16 bit 100 kHz DAQ card (National Instruments). The low population in the $v = 1$ vibrational level made measurements on this level much more difficult than for $v = 0$, therefore the pressure in this case was increased to 100 mTorr to allow signal detection. Measurements of the $(2, 0)$ $P_1(50)$ transition under similar conditions yielded no difference to the alignment or orientation measured at low pressures and give confidence that the conclusions derived from these higher pressure measurements are robust.

As discussed in Chapter 1, the experiment requires measurements to be made using different geometries of the pump and probe electric vectors. The four geometries are illustrated in Figure 5.9. These four geometries all require careful control of the polarisation of both the pump and probe radiation. Since comparisons should be drawn between absorption profiles recorded in the pairs of polarisation geometries indicated in these figures, it is desirable to record both in the course of a single run to minimise experimental differences, such as flow pressures and laser intensity. This is made possible by a employing photoelastic modulator (PEM). It was necessary to switch the polarisation of either the pump or probe beam; the pump was chosen since the PEM introduced amplitude modulation in the probe which interfered with the detected signals. The probe beam's polarisation was therefore set using a linear polariser, to ensure large polarisation purity in the beam, or using a quarter-wave plate to produce circular polarised radiation.

A PEM consists of a birefringent material with a stress-dependent retardation which, when it is compressed by a piezo electric driver, produces a sinusoidally varying retardation. This retardation varies between zero retardation and an experimentally set maxi-

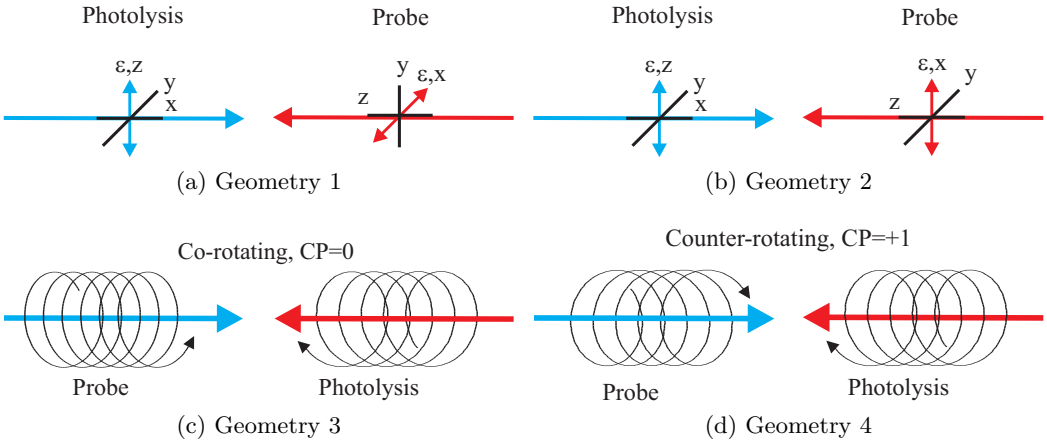

Figure 5.9: The four experimental geometries used to record FM Doppler profiles.

mum, typically either half-wave or quarter-wave, such that at certain points in the stress cycle the PEM behaved as one of these wave plates. Therefore, the pulsed laser was triggered to coincide with the appropriate point in the PEM stress cycle, and by altering the delay it was possible to record two polarisation geometries in one experiment. To illustrate this, Figure 5.10 demonstrates the four desired polarisations achieved by directing laser radiation through the PEM with the electric vector at 45° to the PEM's optical axis; thus making it possible to switch between two polarisations in one experiment: either Figure 5.10a and 5.10b or between Figure 5.10c and 5.10d.

5.6 Data analysis

The Doppler profiles described by equation 1.16, for linear pump-probe, and equation 1.18, for circular pump-probe, were convoluted with a Gaussian, to allow for the velocity distribution of the fragment, and the Gaussian width and bipolar moments were varied to fit the data from the experiment. One of the advantages of studying the CN fragment from ICN photolysis is that the atomic iodine co-fragment has translational and electronic energy only. As illustrated in Figure 5.2 and discussed above, the high rotational states studied in this work are generated in combination with ground state iodine only. In order to reduce the error in the determined bipolar moments the experimentally determined line profiles were fitted in their geometry pairs, i.e. fitted as geometries 1 & 2 and as

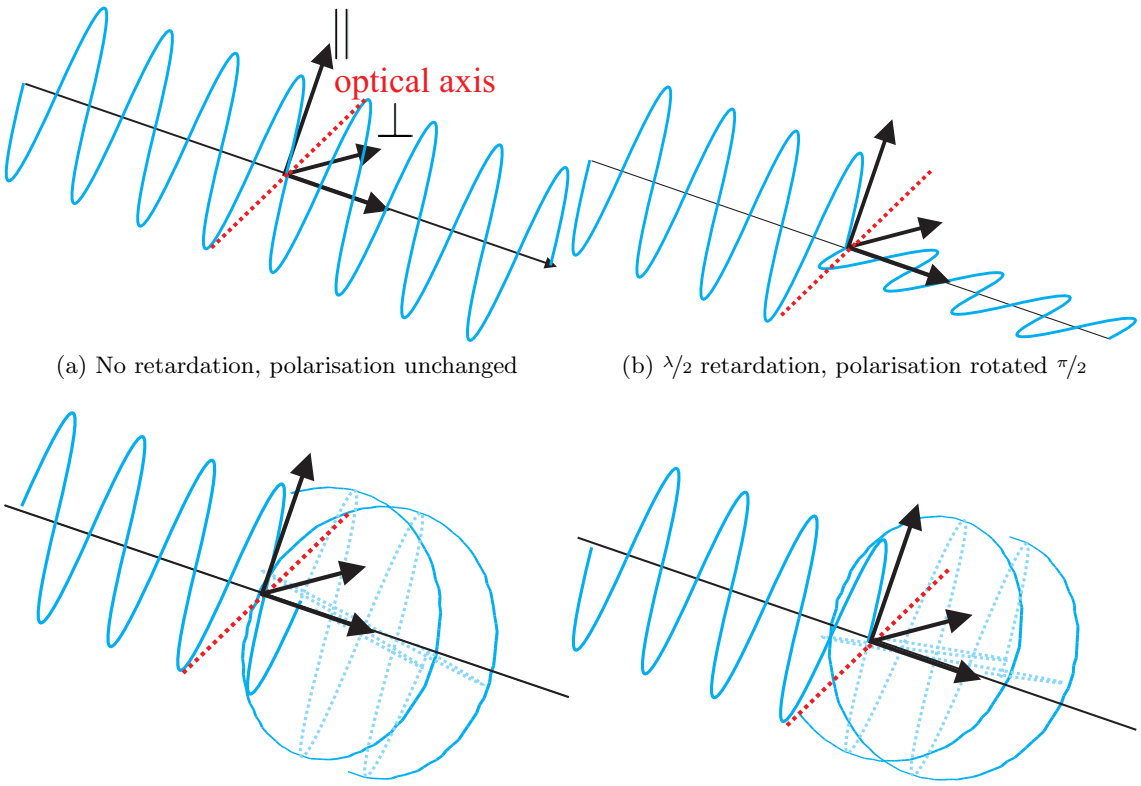

(a) No retardation, polarisation unchanged

(b) $\lambda/2$ retardation, polarisation rotated $\pi/2$

(c) $\lambda/4$ retardation, converted to clockwise circularly polarised light

(d) $\lambda/4$ retardation, converted to counterclockwise circularly polarised light

Figure 5.10: Illustration of the PEM's effect on the polarisation at the stages in the stress cycle. Parallel, $\parallel$, and perpendicular, $\perp$, refers to the axes parallel and perpendicular to the electric vector of the incident radiation. The dashed red line indicates the PEM's optical axis. In 5.10c and 5.10d the dashed blue line indicates the two components of polarisation which generate the circular polarisation.

geometries 3 & 4. Additionally, where possible, the line profiles were fitted with other profiles of the same rotational energy level and spin manifold, i.e. the pairs of linear profiles measured for $Q_1(50)$ and $P_1(50)$ were fitted together with the profiles of $P_1(50)$ determined with circular polarised light. As discussed above, the data were fitted directly (as FM profiles) rather than converting to absorption profiles, using equation 5.6. The analysis of errors was performed in the same fashion as Costen and Hall[18] and Hancock *et al.*[19]: generating 1000 noisy line profiles by combining the residuals with the fits, fitting these simulated profiles to determine the variation of each parameter and quoting twice the standard deviation.

5.7 Results

Measurements were taken for both the ground and first vibrationally excited states and over a range of rotational states of the CN fragment to allow comparison with previous literature results and to determine the alignment and orientation of the $v = 1$ fragment at this photolysis wavelength.

5.7.1 $v = 0$ Alignment

While comprehensive previous studies on ICN photolysis have concentrated on the ground vibrational level,[17,18] only three high rotational states have been reported in the operating region of our spectrometer ($N > 45$); therefore a selection of previously unrecorded states have been studied for comparison. Example data for the pairs of geometries discussed above are shown in Figure 5.11, recorded on the the Q and P branches of the (2,0) vibrational band of the A–X system, probing the $F_1(50)$ state. Also shown are the best fit line shapes, shown in red, generated by fitting to all 6 spectra simultaneously. The residuals from these fits were used to estimate the errors. This and other measurements made across a range of rotational states, and the alignment bipolar moments determined from them, are given in Table 5.1, with literature values included for comparison.

The spectra shown in Figure 5.11 highlight some of the details discussed above. Firstly, all the lineshapes are FM profiles, thus they appear as derivatives of the absorption profiles. Secondly, the marked difference in the Q_1 transition lineshape compared with the P_1 transition lineshape, shown in Figure 5.11a, is due to the increased sensitivity of the Doppler profile to the rotational anisotropy for this transition and geometry; as discussed previously, Q branches are not available in the B–X transition studied by LIF, providing a relative advantage to studying the A–X transition. Thirdly, the difference in the peak areas between pairs of profiles, for example the Q branch pairs shown in Figure 5.11a and 5.11b, indicates that there is a non-zero $\boldsymbol{\mu} - \boldsymbol{J}$ correlation.

The spectra recorded in this way compared well with previous studies, both qualitatively and quantitatively. The $F_1(50)$ transition has been measured previously by Costen and Hall following 266 nm photolysis, and the signal-to-noise, linewidths and lineshapes compare well with their work.[17,18] The same spectrometer has previously been used by

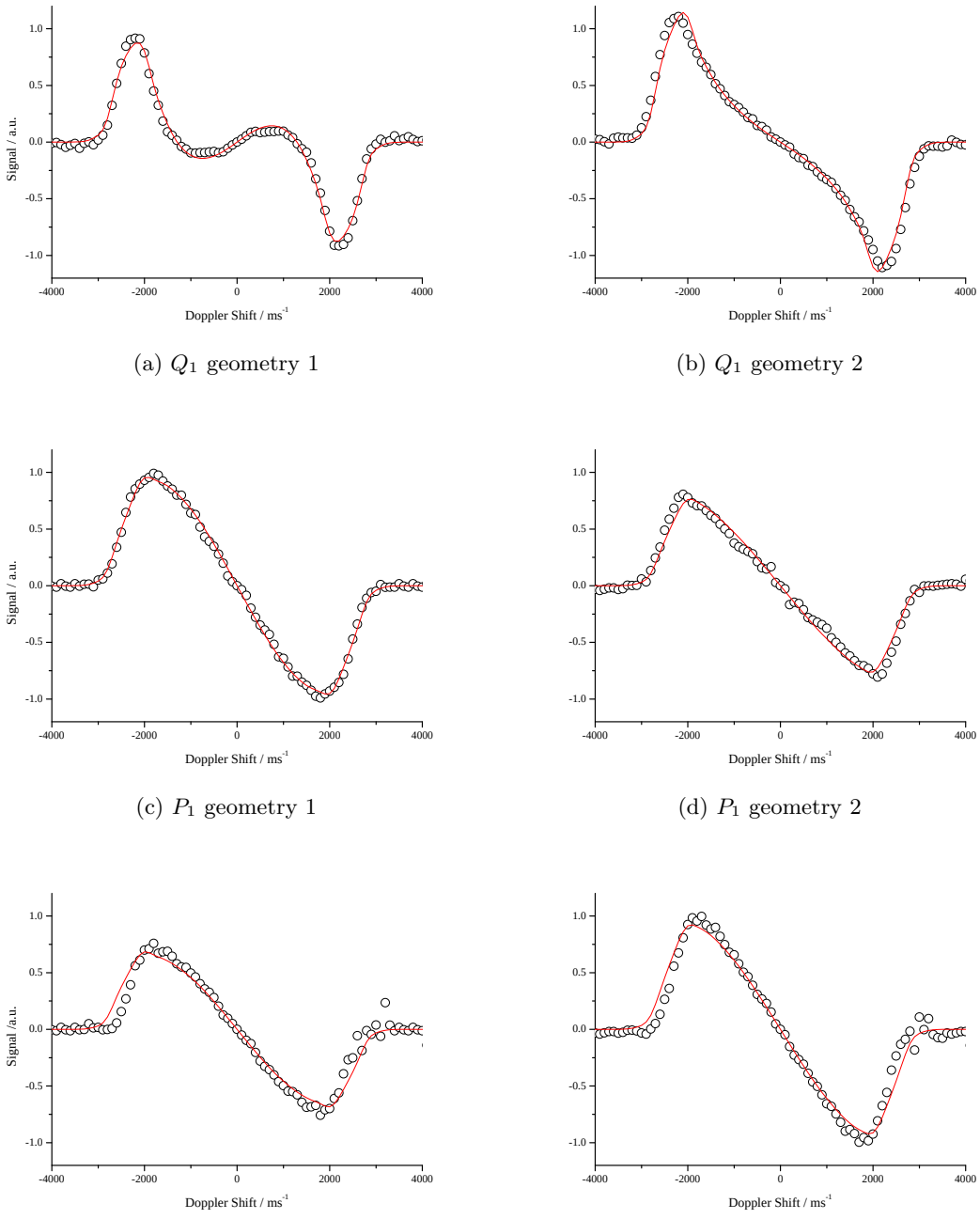

(a) Q_1 geometry 1

(b) Q_1 geometry 2

(c) P_1 geometry 1

(d) P_1 geometry 2

(e) P_1 geometry 3

(f) P_1 geometry 4

Figure 5.11: Example FM absorption profiles for the (2,0) $N = 50, F_1$ transition. The solid red line is the result of a simultaneous fit to all six profiles.

Hancock *et al.* to probe the photodissociation at 248 nm, and our data at 266 nm show comparable signals, both in terms of signal intensity and line shape, to their measur-

Table 5.1: Bipolar moments measured in this work on the (2,0) band. The $*$ indicates an F_2 transition and the † indicates a state taken from the literature.[18]

N	$\beta_0^2(02)$	$\beta_0^2(20)$	$\beta_0^0(22)$	$\beta_0^2(22)$	$\beta_0^2(42)$
Correlation	$\mu - J$	$\mu - v$	$v - J$	$\mu - v - J$	
Range	$-1/2 \leftrightarrow +1$	$-1/2 \leftrightarrow +1$	$-1/2 \leftrightarrow +1$	$-1 \leftrightarrow +1/2$	$-1/2 \leftrightarrow +1$
50†	-0.27 ± 0.08	0.70 ± 0.04	-0.42 ± 0.04	0.36 ± 0.03	-0.31 ± 0.04
50	-0.45 ± 0.03	0.72 ± 0.03	-0.48 ± 0.01	0.32 ± 0.01	-0.29 ± 0.034
51	-0.24 ± 0.09	0.89 ± 0.07	-0.5[i]	0.31 ± 0.04	-0.50 ± 0.07
52	-0.22 ± 0.05	0.75 ± 0.07	-0.38 ± 0.01	0.28 ± 0.02	-0.25 ± 0.04
53	-0.50 ± 0.07	0.55 ± 0.14	0.04 ± 0.03	0.26 ± 0.04	-0.43 ± 0.03
53$*$	-0.28 ± 0.03	0.91 ± 0.08	-0.21 ± 0.01	0.33 ± 0.02	-0.30 ± 0.02
54$*$	-0.41 ± 0.12	0.94 ± 0.09	-0.41 ± 0.02	0.40 ± 0.05	-0.41 ± 0.08
55†	-0.28 ± 0.06	0.77 ± 0.05	-0.43 ± 0.04	0.37 ± 0.06	-0.32 ± 0.03
55	-0.34 ± 0.03	0.87 ± 0.10	-0.22 ± 0.01	0.36 ± 0.03	-0.35 ± 0.03
56	-0.21 ± 0.10	0.63 ± 0.11	-0.42 ± 0.01	0.25 ± 0.02	-0.23 ± 0.07
56$*$	-0.27 ± 0.06	0.85 ± 0.16	-0.31 ± 0.03	0.26 ± 0.02	-0.64 ± 0.13
57	-0.48 ± 0.10	0.89 ± 0.05	-0.24 ± 0.03	0.50 ± 0.06	-0.18 ± 0.04

[i] Fixed at the limiting value to achieve fit.

ments.[19] The values of the alignment bipolar moments agree well with Costen and Hall and are very similar to those found following 248 nm photolysis. Previously it has been seen that the recoil anisotropy, $\beta_0^2(20)$, indicates a primarily parallel transition but reduced from the limiting value. This is also seen in the present work, consistent with a predominantly $^1\Sigma_0^+ \rightarrow {}^3\Pi_{0+}$ transition followed by crossing to the $^1\Pi_1$, since the $^3\Pi_{0+}$ correlates with I* products which can not be formed in conjunction with the high rotational states measured here. To further illustrate this, the bipolar moments have been converted into amplitudes in the limiting cases of vector correlations discussed by Dixon and described below,[28] performed using the conversion of Hall and Wu[29] (given in equation C.1 in Appendix C).

Dixon illustrated five limiting cases, labeled A to E, with the cases A ($\mathbf{v} \parallel \mu \perp \mathbf{J}$) and D ($\mu \perp \mathbf{v} \parallel \mathbf{J}$) implying deviation from the axial recoil limit in the dissociation of ICN and cases B, C and E are shown in Figure 5.12. Case B corresponds to the $^1\Sigma_0^+ \rightarrow {}^3\Pi_{0+}$ transition, whereas the $^1\Sigma_0^+ \rightarrow {}^1\Pi_1$ transition yields cases C and E. The A to E fraction for the (2,0) band studied in this work following 266 nm photolysis is shown in Figure 5.13a with the corresponding 248 nm photolysis results of Hancock *et al.* shown

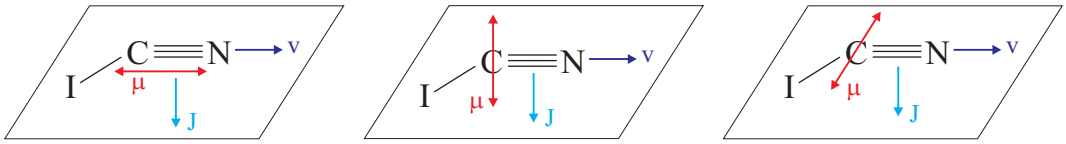

(a) Case B ($\mu \parallel \mathbf{v} \perp \mathbf{J}$) (b) Case C ($\mathbf{v} \perp \mu \parallel \mathbf{J}$) (c) Case E ($\mu \perp \mathbf{v} \perp \mathbf{J}$)

Figure 5.12: Illustration of Dixon's limiting cases, applied to ICN.

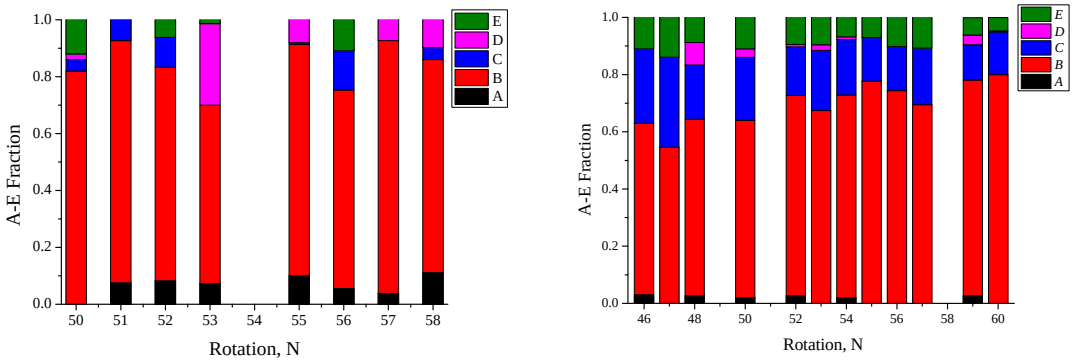

(a) 266 nm Photolysis (b) 248 nm Photolysis

Figure 5.13: The A to E amplitudes for the $v = 0$ CN fragment measured in (a) this work and (b) reproduced from the literature[19].

in Figure 5.13b.[19] The main feature of these figures is that both photolysis wavelengths yield predominantly case B dynamics over the range of rotational states studied, with an average contribution from case B of 69% following 248 nm photolysis and 79% following photolysis at 266 nm. Case B is more prevalent at 266 nm than at 248 nm, as expected, since the $\tilde{A}$ band consists of approximately equal contributions of $^1\Pi_1$ and $^3\Pi_{0+}$ at 248 nm and is largely (85%) $^3\Pi_{0+}$ at 266 nm, as discussed above and illustrated in Figure 5.1a. Similarly, the average recoil anisotropy is closer to limiting following 266 nm photolysis, $\beta = 2\beta_0^2(20) = 1.60$, than for 248 nm photolysis, $\beta = 2\beta_0^2(20) = 1.13$.

The rotational alignment in these high rotational states has been discussed by Amatatsu et al., and by Costen and Hall and is attributed to excitation to the $^3\Pi_{0+}$ state, which approaches the conical intersection with $^1\Pi_1$ at large bending angles, resulting in a large amount of rotational angular momentum in the CN fragment. Therefore the $\boldsymbol{\mu - J}$ correlation and the $\boldsymbol{v - J}$ correlation approach limiting values of $\boldsymbol{J}$ perpendicular to both

$\boldsymbol{\mu}$ and $\boldsymbol{v}$, as seen here and illustrated in Figure 5.12a.[14,17]

5.7.2 $v = 0$ Orientation

The orientation bipolar moments generated from fits to the two circular polarised geometries shown in Figure 5.11 are given in Table 5.2, along with previous measurements. These orientation bipolar moments are those introduced by Costen and Hall in their work on ICN photolysis[18] and used by Hancock *et al*[19]; the values recorded in this work compare well with both of these measurements on ICN. Much of the literature quantifies the orientation in different ways, so it is necessary to convert between these different notations to allow comparison. The coherent orientation parameter $\mathrm{Re}[a_1^1(\parallel,\perp)]$, introduced for diatomics by Rakitzis and Zare,[30] has been used by Costen and Hall to allow comparison between their orientation bipolar moments and previous studies.[18] Though strictly not appropriate for photolysis of a triatomic molecule they have been used here to allow comparison with earlier studies. Rakitzis has since extended these $a_q^k(\mathrm{p})$ parameters to include triatomics, but for comparison the conversion of Costen and Hall is used here.[18]

Through knowledge of the orientation bipolar moments and the recoil anisotropy, the $\mathrm{Re}[a_1^1(\parallel,\perp)]$ parameter can be determined from:

$$Re[a_1^1(\parallel,\perp)] = \frac{\left(5\beta_0^1(21) - 2\beta_0^1(01)\right)}{\sqrt{(1+\beta)(2-\beta)}}. \tag{5.9}$$

The values determined in this way have also been included in Table 5.2.[18]

As seen previously in ICN photolysis the orientation displays a rotational state dependence. This is evident in Table 5.2. These results have been plotted in Figure 5.14 alongside literature results for both the F_1 and F_2 spin manifolds and for both I and I* products, with the states from the present work shown as triangles in an overlay.[18] The orientation is the result of interference effects between the PESs as they approach the products. The $a_1^1(\parallel,\perp)$ polarisation parameter quantifies the phase difference, $\Delta\phi$, between surfaces with $Im[a_1^1(\parallel,\perp)]$ depending on $\sin\Delta\phi$ and $Re[a_1^1(\parallel,\perp)]$ depending on $\cos\Delta\phi$.[2] Since this depends upon the relative contribution of each of the surfaces to the wavepacket, in this case the $^3\Pi_{0+}$ and $^1\Pi_1$ surfaces, the interference between states will

Table 5.2: Orientation Bipolar moments measured in the (2,0) band. The $*$ indicates an F_2 transition and † is taken from the literature.[18]

N	$\beta_0^1(01)$	$\beta_0^1(21)$	$Re[a_1^1(\parallel,\perp)]$
50†	-0.07 ± 0.01	0.019 ± 0.001	≈ 0.15[i]
50	-0.093 ± 0.002	0.019 ± 0.001	0.238 ± 0.014
51	-0.070 ± 0.003	0.014 ± 0.001	0.266 ± 0.076
52	-0.033 ± 0.001	0.007 ± 0.01	0.090 ± 0.016
53	-0.036 ± 0.003	0.007 ± 0.001	0.078 ± 0.010
53$*$	-0.075 ± 0.003	0.015 ± 0.001	0.314 ± 0.058
54$*$	0.060 ± 0.004	-0.012 ± 0.001	-0.306 ± 0.105
55†	-0.03 ± 0.005	0.005 ± 0.001	≈ 0.10[i]
55	-0.013 ± 0.001	0.003 ± 0.001	0.048 ± 0.008
56	-0.013 ± 0.001	0.003 ± 0.001	0.031 ± 0.006
56$*$	0.041 ± 0.003	-0.008 ± 0.001	-0.138 ± 0.031
57	0.022 ± 0.001	-0.004 ± 0.001	-0.087 ± 0.011

[i] Estimated from the literature.

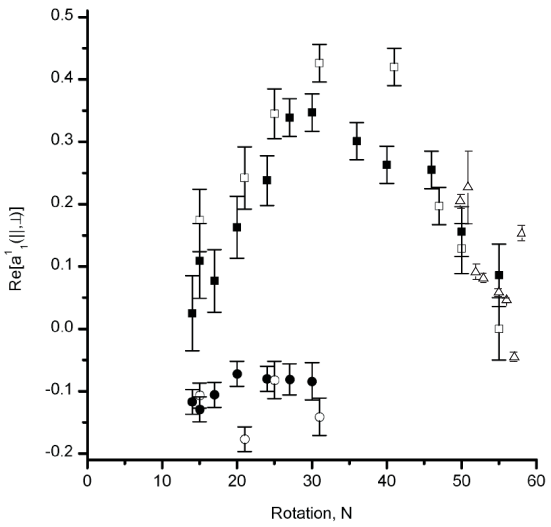

Figure 5.14: Re$[a_1^1(\parallel,\perp)]$ as a function of rotational state, reproduced from Costen and Hall with the states measured in this work shown as triangles, the squares correspond to CN formed with I and the circles CN with I*; the filled and hollow points correspond to F_1 and F_2, respectively.[18]

in turn depend upon the relative accessibility of the states, as shown in Figure 5.1a. This has been demonstrated in the literature, where Costen and Hall[18] and Hancock *et al.*[19] have observed photolysis wavelength dependence of the orientation across the $\tilde{A}$ band, as well as rotational and vibrational state dependence.

5.7.3 $v = 1$ Alignment

Whilst there has been a wealth of interest in the $v = 0$ CN fragments at various wavelengths,[9–11,16–18] only one previous study has measured the spatial anisotropy of the $v = 1$ CN fragment, at a photolysis wavelength of 248 nm.[19] As discussed above, this study found little or no orientation of the fragment formed in $v = 1$ but this fragment has very similar alignment to the fragment formed in $v = 0$ products. This has motivated the present study to determine the orientation of the $v = 1$ CN fragment following 266 nm photolysis. As with the ground vibrational level, the number of rotational states accessible to the diode laser limited the study to high rotational energy levels. The available states were further limited by the population distribution, with more than 99% of the population in the ground vibrational state and a rotational distribution which peaks around $J = 25$.[24,25] In addition to this, many of the accessible rotational lines were obscured by other, much stronger, spectral features. However, it was possible to record Doppler profiles for four quantum states.

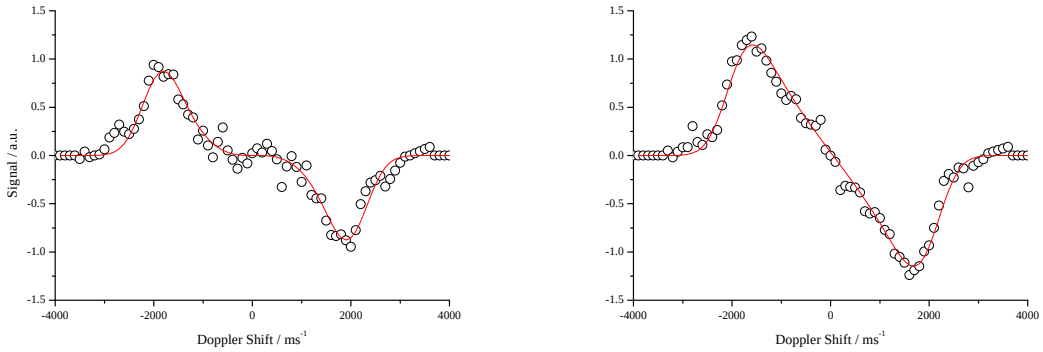

(a) $Q_1(50)$ geometry 1 (b) $Q_1(50)$ geometry 2

Figure 5.15: Example FM absorption profiles for the (3,1) transition. The solid red line is the result of fitting to the pair shown.

Example data for the $Q_1(50)$ transition, with both the pump and probe linearly polarised, is shown in Figure 5.15 along with the best fit to the data. The signal to noise ratio is noticeably lower than in the previous study[19] on CN($v = 1$) from 248 nm photolysis, probably due to the very small populations ($< 1\%$) of the states recorded in this work.

In contrast, the $v = 1$ vibrational state accounts for 4% of the vibrational population following 248 nm photolysis, with the rotational distribution peaking around $N = 50$.[25]

The alignment bipolar moments determined from fitting to this and other data are shown in Table 5.3. These are in reasonable agreement with those determined for the $v = 0$ level in this work; similarly, bipolar moments for $v = 0$ and $v = 1$ were found to compare well when photolysing ICN at 248 nm and the values obtained in that study are comparable to the values obtained in this work.[19] The similarity of the alignment bipolar moments reveals that the incoherent aspects of the photodissociation process do not vary between rotational or vibrational states or over the photolysis wavelength range studied. This indicates that the overall excitation process is remarkably uniform across the $\tilde{A}$ band.

Table 5.3: Bipolar moments measured in the (3,1) band following 266 nm photolysis of ICN.

N	$\beta_0^2(02)$	$\beta_0^2(20)$	$\beta_0^0(22)$	$\beta_0^2(22)$	$\beta_0^2(42)$
Correlation	$\mu - J$	$\mu - v$	$v - J$	$\mu - v - J$	
Range	$-1/2 \leftrightarrow +1$	$-1/2 \leftrightarrow +1$	$-1/2 \leftrightarrow +1$	$-1 \leftrightarrow +1/2$	$-1/2 \leftrightarrow +1$
38	-0.40 ± 0.04	0.87 ± 0.06	-0.38 ± 0.08	0.39 ± 0.03	-0.19 ± 0.04
45	-0.42 ± 0.04	0.72 ± 0.05	-0.28 ± 0.09	0.34 ± 0.03	-0.24 ± 0.04
48	-0.37 ± 0.12	0.89 ± 0.07	-0.41 ± 0.10	0.34 ± 0.05	-0.22 ± 0.07
50	-0.26 ± 0.05	1.00 ± 0.04	-0.50[i]	0.36 ± 0.04	-0.22 ± 0.09

[i] Fixed at the limiting value to achieve fit

Table 5.4: Bipolar moments measured in the (3,1) band following 248 nm photolysis, reproduced from Hancock *et al.*.[19]

N	$\beta_0^2(02)$	$\beta_0^2(20)$	$\beta_0^0(22)$	$\beta_0^2(22)$	$\beta_0^2(42)$
Correlation	$\mu - J$	$\mu - v$	$v - J$	$\mu - v - J$	
38	-0.17 ± 0.11	0.44 ± 0.04	-0.43 ± 0.06	0.23 ± 0.03	-0.28 ± 0.07
44	-0.34 ± 0.11	0.43 ± 0.03	-0.36 ± 0.04	0.26 ± 0.03	-0.24 ± 0.05
48	-0.22 ± 0.18	0.44 ± 0.04	-0.44 ± 0.08	0.26 ± 0.04	-0.25 ± 0.18
51	-0.23 ± 0.08	0.45 ± 0.12	-0.45 ± 0.03	0.22 ± 0.02	-0.25 ± 0.08
53	-0.23 ± 0.12	0.46 ± 0.18	-0.41 ± 0.04	0.26 ± 0.03	-0.19 ± 0.20

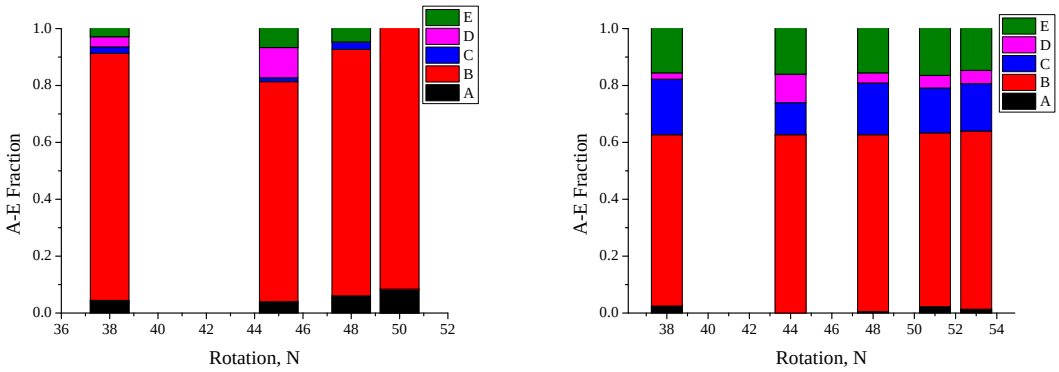

(a) 266 nm photolysis

(b) 248 nm photolysis

Figure 5.16: The A to E amplitudes for the $v = 1$ CN fragment measured in (a) this work and (b) reproduced from the literature.[19]

5.7.4 $v = 1$ Orientation

Example data for the $R_1(51)$ transition, with both pump and probe circularly polarised, are shown in Figure 5.17. Unfortunately efforts to probe the $R_1(51)$ and $Q_1(51)$ transitions using linearly polarised light were unsuccessful. Since it was not possible to record the desired linear $R_1(51)$ data set it was necessary to fit data in the pairs recorded by the spectrometer. As discussed above, the orientation bipolar moments are the only contribution to the line shape that varies between the two geometries; however, the alignment bipolar moments still contribute to the ratio of intensities (equation 1.18 in Chapter 1). Therefore, fitting the circularly polarised studies required using the lower order bipolar moments generated from linearly polarised studies. This should be valid since there is only a little variance in the bipolar moments between nearby states and across the entire $\tilde{A}$ band.[17]

Table 5.5: Orientation bipolar moments measured in the (3,1) band.

N	$\beta_0^1(01)$	$\beta_0^1(21)$	$Re[a_1^1(\parallel,\perp)]$
48	0.11 ± 0.03	-0.01 ± 0.01	-0.35 ± 0.16
50	0.07 ± 0.04	-0.00 ± 0.01	-0.21 ± 0.18
51	0.07 ± 0.03	-0.02 ± 0.01	-0.28 ± 0.16
52	0.03 ± 0.05	-0.01 ± 0.01	-0.13 ± 0.18

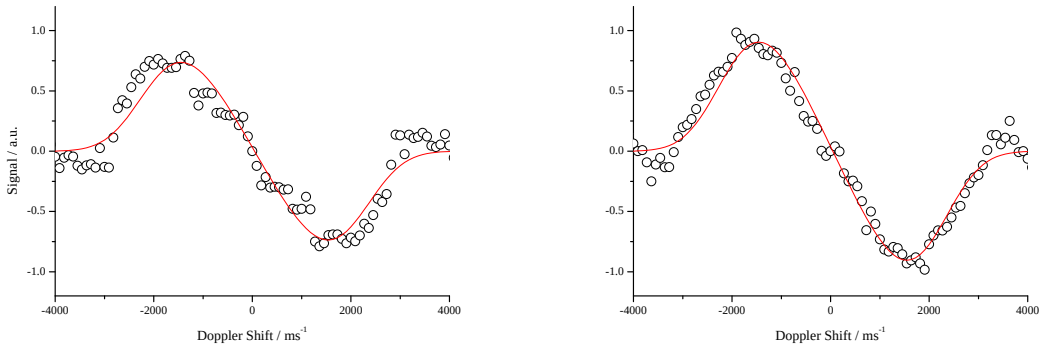

(a) $R_1(51)$ geometry 3

(b) $R_1(51)$ geometry 4

Figure 5.17: Example FM absorption profiles for the (3,1) transition. The solid red line is the result of fitting to each pair of profiles.

Table 5.6: Orientation bipolar moments measured in the (3,1) band following 248 nm photolysis, reproduced from Hancock *et al.*[19]

N	$\beta_0^1(01)$	$\beta_0^1(21)$	$Re[a_1^1(\|,\perp)]$
38	-0.023 ± 0.020	0.005 ± 0.004	0.05 ± 0.04
44	-0.038 ± 0.021	0.008 ± 0.004	0.08 ± 0.04
48	-0.032 ± 0.019	0.006 ± 0.004	0.07 ± 0.04
51	-0.044 ± 0.016	0.009 ± 0.003	0.09 ± 0.03
53	-0.010 ± 0.017	0.002 ± 0.003	0.02 ± 0.04

The orientation bipolar moments determined from these and other data are shown in Table 5.5. Interestingly, these orientation moments are of the opposite sign to the ground vibrational energy level, unlike the equivalent measurements following 248 nm photolysis, given in Table 5.6 for which the measured orientation is near-zero within error, and of opposite sign to the 266 nm measurements. The larger errors on the orientation moments of the $v = 1$ products of 266 nm photolysis relative to the $v = 1$ products of 248 nm are due to the very low population produced by 266 nm photolysis ($< 1\%$) relative to the 248 nm photolysis ($\approx 4\%$).

5.8 Discussion

The measurements taken on the $v = 0$ CN fragments compare well with the study at 248 nm[19] and across the $\tilde{A}$ band,[17,18] both in terms of the orientation and the alignment moments measured. This generates confidence that the spectrometer is returning the nascent line profiles, free of any experimental artefacts. Further to this, measurements of the alignment of rotational states in the $v = 1$ vibrational level also compare well with the $v = 0$ and the only other $v = 1$ measurement in the literature;[19] therefore inspiring confidence in the sign of the $v = 1$ orientation parameters measured.

In addition to the orientation parameter, older studies[11] quote the degree of orientation, $C(N)$, defined as the difference between the integrated areas, I_{p_1,p_2}, of the profiles observed with different helicities of circularly polarised light (divided by their sum). By integrating the Doppler profiles (equation 1.18) and performing the same procedure $C(N)$ can be determined from the orientation moment $\beta_0^1(01)$ and the rotational anisotropy parameter $\beta_0^2(02)$ according to equation 5.10, where $V(J) \approx 2$ for the rotational levels studied in this work. The full expression is given by equation A.7 in Appendix A, along with $h^{(1)}$ and $h^{(2)}$.

$$C(N) = \frac{I_{\circlearrowright\circlearrowright} - I_{\circlearrowright\circlearrowleft}}{I_{\circlearrowright\circlearrowright} + I_{\circlearrowright\circlearrowleft}} = \frac{3h^{(1)}\beta_0^1(01)}{2 - h^{(2)}V(J)\beta_0^2(02)} \tag{5.10}$$

Polarisation measurements for excited vibrational levels of CN have only been reported twice, by Hancock *et al.*[19] and Black *et al.*.[11] In the latter, Black *et al.* probed the $v = 2$ CN fragment from 248 nm photolysis using LIF on the B $^2\Sigma^+$ - X $^2\Sigma^+$ (0,2) band, where they found that the degree of orientation was of the opposite sign to that recorded *via* the B $^2\Sigma^+$ - X $^2\Sigma^+$ (0,0) transition studied in other work.[11,12,19] The value for the degree of orientation obtained by Black *et al.* is plotted in Figure 5.18, which is adapted from Hancock *et al.*[19] to include the results of 266 nm photolysis measured in this work.

This figure indicates that the lack of orientation in the $v = 1$ product following 248 nm photolysis observed by Hancock *et al.* arises as part of a trend. Since the population of the C-N stretch is believed to be largely carried through from the parent ICN vibrational population, this suggests that the vibrational excitation alters the interference between the two paths to the products. Hence, by changing the photolysis wavelength to sample different initial contributions of the $^3\Pi_{0+}$ and $^1\Pi_1$ states in the $\tilde{A}$ band, in addition to the

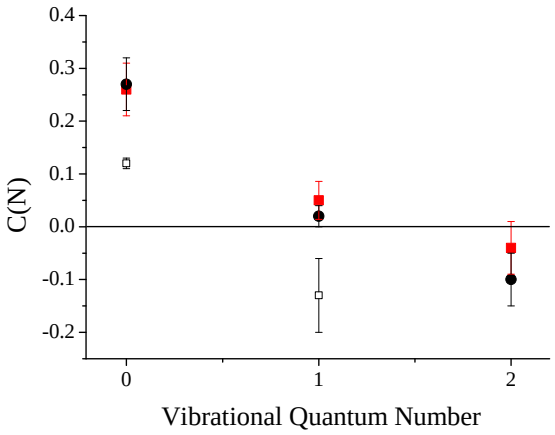

Figure 5.18: Degree of orientation, $C(N)$, for $v = 0$, 1 and 2 for 248 nm, shown as solid squares and taken from Hancock *et al.*[19] and Black *et al.*[11], and 266 nm photolysis recorded in this work, shown as open squares. For both wavelengths squares are $N = 48$ and black circles are $N = 53$.

effect of vibration, we see different orientation behaviour.

The degree of orientation can be related to the $Re[a_1^1(\parallel, \perp)]$ parameter through:

$$C(N) = Re[a_1^1(\parallel, \perp)] \frac{2h^{(1)}\sqrt{(1+\beta)(2-\beta)}}{4 - h^{(2)}V(J)\beta}, \tag{5.11}$$

where the the h^i factors are dependent on the type of transition and the rotational state involved and the $V(J)$ term depends upon the rotational state. Both are given in Appendix A.

Since the $Re[a_1^1(\parallel, \perp)]$ parameter depends upon $\cos\Delta\phi$, the change in sign of the degree of orientation or $Re[a_1^1(\parallel, \perp)]$ must occur either about a phase difference of $\Delta\phi = n\pi/2$ or at a point where there are no interference effects. Since the alignment moments are so similar across the vibrational and rotational levels studied in this work and by Hancock *et al.*, it is likely that interference between the excited states does occur. The deviations from limiting recoil anisotropyof $\beta = 2\beta_0^2(20) = 2$, across all states studied in this work, and the previous studies at 248 nm, demonstrate that photolysis in this region always occurs *via* mixed parallel and perpendicular transitions, so both excited states are reached. It is highly unlikely these states do not produce interference effects, especially since the high J states recorded in this and previous studies must be the result of curve crossing at the

conical intersection, as discussed above.

The non-zero orientation measured in this work suggests that the lack of orientation observed by Hancock *et al.* is the result of a phase difference of $\Delta\phi = n\pi/2$. This phase difference could be confirmed experimentally by measuring the $Im[a_1^1(\|,\perp)]$ parameter, which depends upon $\sin\Delta\phi$ and so should be at a maximum for the CN($v = 1$) products following 248 nm photolysis if the phase difference is $\Delta\phi = n\pi/2$. Unfortunately, frequency modulation spectroscopy is insensitive to the $Im[a_1^1(\|,\perp)]$ parameter. In order to measure this parameter a technique with a detection direction 90° to the probe direction is needed, such as LIF or REMPI.

5.9 Conclusion and Future work

In this chapter the application of frequency modulation spectroscopy to detect nascent CN fragments following 266 nm photolysis of ICN in the $\tilde{A}$ band has been reported. The alignment of the CN fragments across a range of rotational states in the first two vibrational levels was recorded and found to be similar to measurements taken on the CN fragment following 248 nm photolysis of ICN,[19] and in keeping with the general understanding of excitation in the $\tilde{A}$ band of ICN. Measurements of the orientation of these rotational states have revealed the $v = 1$ fragment to have opposite orientation to the $v = 0$ fragment, whereas the complementary studies at 248 nm found no orientation for $v = 1$,[19] with earlier work reporting opposite orientation for the $v = 2$ following 248 nm photolysis.[11] The difference between the orientations generated at the two photolysis wavelengths was interpreted in terms of the phase differences of the excited states accessed by each wavelengths, with the vibrational level dependence occurring due to the trajectories along these excited state potential energy surfaces. This could be confirmed by further experimental work, employing laser induced fluorescence to measure an orientation parameter to which our present spectrometer is insensitive.

References

[1] T. P. Rakitzis, Science **281**, 1346 (1998).

[2] A. J. Alexander et al., The Journal of Chemical Physics **113**, 9022 (2000).

[3] T. Rakitzis et al., Chemical Physics Letters **364**, 115 (2002).

[4] A. P. Clark, M. Brouard, F. Quadrini, and C. Vallance, Physical chemistry chemical physics : PCCP **8**, 5591 (2006).

[5] E. K. Campbell et al., The Journal of Chemical Physics **136**, 164311 (2012).

[6] A. J. Johnsen et al., The Journal of Chemical Physics **136**, 164310 (2012).

[7] H. Joswig, M. A. O'Halloran, R. N. Zare, and M. S. Child, Faraday Discussions of the Chemical Society **82**, 79 (1986).

[8] G. E. Hall, N. Sivakumar, and P. L. Houston, The Journal of Chemical Physics **84**, 2120 (1986).

[9] M. A. OHalloran, H. Joswig, and R. N. Zare, The Journal of Chemical Physics **87**, 303 (1987).

[10] E. Hasselbrink, J. R. Waldeck, and R. N. Zare, Chemical Physics **126**, 191 (1988).

[11] J. Black, E. Hasselbrink, J. Waldeck, and R. Zare, Molecular Physics **71**, 1143 (1990).

[12] J. F. Black, J. R. Waldeck, and R. N. Zare, The Journal of Chemical Physics **92**, 3519 (1990).

[13] J. Qian, D. J. Tannor, Y. Amatatsu, and K. Morokuma, The Journal of Chemical Physics **101**, 9597 (1994).

[14] Y. Amatatsu, S. Yabushita, and K. Morokuma, The Journal of Chemical Physics **100**, 4894 (1994).

[15] H. Wei and T. Carrington, The Journal of Chemical Physics **105**, 141 (1996).

[16] S. North, Chemical Physics Letters **276**, 103 (1997).

[17] M. L. Costen, S. W. North, and G. E. Hall, The Journal of Chemical Physics **111**, 6735 (1999).

[18] M. L. Costen and G. E. Hall, Physical chemistry chemical physics : PCCP **9**, 272 (2007).

[19] G. Hancock et al., Molecular Physics **108**, 1083 (2010).

[20] M. Glass-Maujean and J. A. Beswick, Journal of the Chemical Society, Faraday Transactions 2 **85**, 983 (1989).

[21] S. W. North, X. S. Zheng, R. Fei, and G. E. Hall, The Journal of Chemical Physics **104**, 2129 (1996).

[22] M. L. Costen and G. E. Hall, Physical Chemistry Chemical Physics **7**, 1408 (2005).

[23] E. M. Miller et al., The Journal of Chemical Physics **136**, 044313 (2012).

[24] I. Nadler, D. Mahgerefteh, H. Reisler, and C. Wittig, The Journal of Chemical Physics **82**, 3885 (1985).

[25] W. Fisher, Chemical Physics **89**, 457 (1984).

[26] K. Herzberg, G. and Huber, *Molecular spectra and molecular structure. I. Spectra of diatomic molecules*, Van Nostrand Reinhold, second edition, 1957.

[27] G. E. Hall and S. W. North, Annual review of physical chemistry **51**, 243 (2000).

[28] R. N. Dixon, The Journal of Chemical Physics **85**, 1866 (1986).

[29] G. E. Hall and M. Wu, The Journal of Physical Chemistry **97**, 10911 (1993).

[30] T. P. Rakitzis and R. N. Zare, The Journal of Chemical Physics **110**, 3341 (1999).

Chapter 6

Conclusion

This thesis has presented several applications of near infrared diode lasers to high-resolution spectroscopy of transient species. Time-resolved near-infrared laser gain *versus* absorption spectroscopy was utilised in Chapter 2 to determine the quantum yield for forming spin-orbit-excited iodine atoms, $\Phi(I^*)$, following ultraviolet photolysis of a selection of aryl iodides. Initial measurements of $\Phi(I^*)$ following 248 nm and 266 nm photolysis of iodobenzene return a value of $\Phi(I^*) = 0.28 \pm 0.04$, markedly lower than that reported previously by Kavita and Das. While the differences between the current work and Kavita and Das could not be satisfactorily resolved, a number of potential problems in the work of Kavita and Das were discussed, and the present method was found to be in very good agreement with the bulk of the literature.[1,2] The effect of fluorination on the quantum yield was also reported. Selective fluorination was used to lower the symmetry of the iodobenzene, in addition to influencing the excited state potential energy surfaces involved in the dissociation. These fluorinated aryl iodides displayed only minor differences in the quantum yield. However, complementary studies of the recoil direction and vibrational energy partitioning, performed using photofragment translational spectroscopy and velocity map ion imaging find fluorination alters the dynamics.[3,4]

Chapter 3 detailed the development of a narrow-bandwidth, tunable, continuous-wave ultraviolet radiation source. Sum frequency mixing allowed absorption spectroscopy based upon tunable near infrared diode lasers to be used to probe rotational fine structure in the $\tilde{A} - \tilde{X}$ electronic transition of formaldehyde. Three vibronic bands were studied, the $2_0^2 4_0^1$, $2_0^2 4_0^3$ and $2_0^3 4_0^3$. For the $2_0^2 4_0^1$ band the sub-Doppler resolution afforded by the source allowed Doppler limited lineshapes to be recorded at low pressures (sub Torr) and allowed

determination of absolute absorption cross sections, which compared very favourably with literature results and simulations.[5,6] For example, the ${}^{p}Q_{2,12}(13)$ rotational transition, occurring at $30\,598.20\,\mathrm{cm}^{-1}$ in the $2_0^2 4_0^1$ vibronic band, was determined to be $(1.09 \pm 0.06) \times 10^{-19}\mathrm{cm}^2\mathrm{molecule}^{-1}$ and the spectral simulation program PGOPHER predicts $1.07 \times 10^{-19}\mathrm{cm}^2\mathrm{molecule}^{-1}$. In the $2_0^2 4_0^3$ band the rotational constants were optimised and absolute absorption cross sections were determined. These were again consistent with PGOPHER predictionsbut at odds with the recent low resolution studies reported by Tatum Ernest *et al.*[7] In addition to this, the lifetimes of a small selection of excited states were measured in the $2_0^2 4_0^3$ vibronic band and all determined to be in the 0.7 – 1.5 ns range.

In Chapter 4 the UV radiation source developed in Chapter 3 was applied to the $A\,{}^2\Sigma^+ - X\,{}^2\Pi$ electronic band of the OH radical. Cavity enhanced absorption spectroscopy and wavelength modulation spectroscopy were used to probe a continuous supply of OH radicals, and the detection limits of these techniques was found to be comparable with those reported in the literature, with $\alpha_{\mathrm{min}} = (46.5 \pm 3.6) \times 10^{-8}\mathrm{cm}^{-1}$ for CEAS and $(9.45 \pm 1.04) \times 10^{-7}\mathrm{cm}^{-1}$ for WMS.[8–10] Pressure induced broadening parameters for the $Q_1(2)$ rotational transition for He, Ne, Ar and N_2 buffer gases were also measured. In Chapter 4, initial results of probing OH radicals from nitric acid photolysis at 193 nm were reported. The nascent speed distribution and line profile were shown to be in excellent agreement with the literature.[11,12] These preliminary results indicate the potential of this narrow-bandwidth tunable UV source as an absorption spectroscopy based probe of nascent Doppler profiles. The returned thermalisation rate constant of $k_{\mathrm{trans}} = (3.85 \pm 1.06) \times 10^{-10}\mathrm{cm}^3\mathrm{molecule}^{-1}\mathrm{s}^{-1}$ was in good agreement with literature results which are typically of the order of $10^{-10}\mathrm{cm}^3\mathrm{molecule}^{-1}\mathrm{s}^{-1}$.[13,14]

Chapter 5 reported the application of frequency modulation spectroscopy to detect nascent CN fragments following 266 nm photolysis of ICN in the $\tilde{A}$ band. The alignment of the CN fragments across a range of rotational states in the first two vibrational levels was determined, and was found to be similar to that found from measurements taken on the CN fragment following 248 nm photolysis of ICN,[15] and also in keeping with the general understanding of excitation in the $\tilde{A}$ band of ICN. The incoherent aspects of the photodissociation dynamics are essentially wavelength independent. Measurements of the

$\beta_0^1(01)$ and $\beta_0^1(21)$ orientation bipolar moments of these rotational states revealed the $v = 1$ level to have opposite orientation to the $v = 0$ level, whereas the complementary studies at 248 nm found no orientation in the $v = 1$.[15] However, the magnitude of the difference between the orientation of the $v = 0$ and $v = 1$ CN fragment formed following 266 nm photolysis is consistent with that measured following 248 nm photolysis of ICN. This is attributed to phase differences between the wavepacket propagating on multiple excited potential energy surfaces.

References

[1] K. Kavita and P. K. Das, The Journal of Chemical Physics **117**, 2038 (2002).

[2] W. H. Pence, S. L. Baughcum, and S. R. Leone, The Journal of Physical Chemistry **85**, 3844 (1981).

[3] A. G. Sage et al., Physical chemistry chemical physics : PCCP (2011).

[4] D. Murdock, M. B. Crow, G. A. D. Ritchie, and M. N. R. Ashfold, The Journal of Chemical Physics **136**, 124313 (2012).

[5] C. A. Smith, F. D. Pope, B. Cronin, C. B. Parkes, and A. J. Orr-Ewing, The Journal of Physical Chemistry A **110**, 11645 (2006).

[6] M. Motsch et al., Journal of Molecular Spectroscopy **252**, 25 (2008).

[7] C. Tatum Ernest, D. Bauer, and A. J. Hynes, The Journal of Physical Chemistry A **116**, 5910 (2012).

[8] D. B. Oh, Optics Letters **20**, 100 (1995).

[9] G. Hancock and V. Kasyutich, Applied Physics B **79**, 383 (2004).

[10] V. L. Kasyutich, The European Physical Journal D **33**, 29 (2005).

[11] Q. Li, R. T. Carter, and J. Huber, Chemical Physics Letters **334**, 39 (2001).

[12] J. R. Huber, Chemphyschem : a European journal of chemical physics and physical chemistry **5**, 1663 (2004).

[13] Y. Matsumi, S. M. Shamsuddin, Y. Sato, and M. Kawasaki, The Journal of Chemical Physics **101**, 9610 (1994).

[14] J. I. Cline, C. A. Taatjes, and S. R. Leone, The Journal of Chemical Physics **93**, 6543 (1990).

[15] G. Hancock et al., Molecular Physics **108**, 1083 (2010).

[16] J. Black, E. Hasselbrink, J. Waldeck, and R. Zare, Molecular Physics **71**, 1143 (1990).

Appendix A

Introduction

The equation for a Doppler profile using linear pump and probe given by equation A.1 as discussed in Chapter 1.[1]

$$D(w) = \frac{1}{2v_0}\left[g_0 + g_2 P_2\left(\frac{w}{v_0}\right) + g_4 P_4\left(\frac{w}{v_0}\right)\right] \tag{A.1}$$

The g_i terms give the dependence on the bipolar moments as in equation A.2.[1]

$$\begin{aligned} g_0 &= 1 + b_1\beta_0^2(02) \\ g_2 &= b_2\beta_0^2(20) + b_3\beta_0^0(22) + b_4\beta_0^2(22) \\ g_4 &= b_5\beta_0^2(42) \end{aligned} \tag{A.2}$$

The pre-mulitpliers, b_i, depend upon the experimental geometry as given in equation A.3 where θ is the angle between propagation of the two lasers, $\theta = \pi/2$ for the counter propagating experiments used in this thesis. χ is the angle between the photolysis x-y plane and the electric vector of the probe (ε or x), $\chi = 0$ for Figure A.1a or $\chi = \pi/2$ for Figure A.1b.[1]

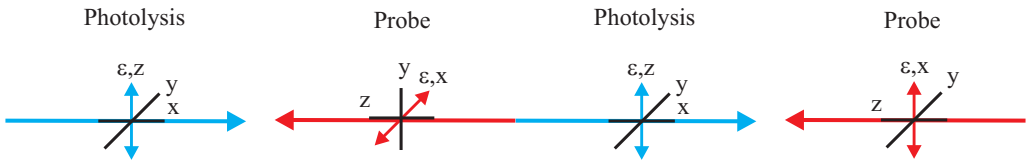

(a) Perpendicular electric vectors (b) Parallel electric vectors

Figure A.1: The reference frames involved in linearly polarized pump-probe theory.[1]

$$
\begin{aligned}
b_1 &= h^{(2)}\left[\frac{3}{5}\sin^2\theta\cos 2\chi - \frac{2}{5}P_2\left(\cos\theta\right)\right] \\
b_2 &= 2P_2(\cos\theta) \\
b_3 &= -h^{(2)} \\
b_4 &= h^{(2)}\left[\frac{6}{7}\sin^2\theta\cos 2\chi + \frac{4}{7}P_2(\cos\theta)\right] \\
b_5 &= \frac{h^{(2)}}{35}\left[9\sin^2\theta\cos 2\chi - 36P_2(\cos\theta)\right]
\end{aligned}
\tag{A.3}
$$

The $h^{(2)}$ terms are line strength factors which depend upon the type of branch being probed according to equation A.4.

$$
\begin{aligned}
Q:&\ h^{(2)} = +1 \\
P:&\ h^{(2)} = -J/(2J+3) \\
R:&\ h^{(2)} = -(J+1)/(2J-1)
\end{aligned}
\tag{A.4}
$$

For circularly polarised pump and probe radiation the Doppler profile is described by equation A.5. [2]

$$
\begin{aligned}
D(w) = 1 &+ 5\beta_0^2(20)P_2\left(\frac{w}{v_0}\right) \\
&+(-1)^{CP}\frac{3}{2}h^{(1)}\left[\beta_0^1(01) + 5\beta_0^1(21)P_2\left(\frac{w}{v_0}\right)\right] \\
&-h^{(2)}V(J)\left[\frac{1}{2}\beta_0^0(22)P_2\left(\frac{w}{v_0}\right) + \frac{1}{2}\beta_0^2(02)\right. \\
&\qquad\left. - \frac{5}{7}\beta_0^2(22)P_2\left(\frac{w}{v_0}\right) + \frac{9}{7}\beta_0^2(42)P_4\left(\frac{w}{v_0}\right)\right]
\end{aligned}
\tag{A.5}
$$

Once again the $h^{(1)}$ terms are line strength factors which depend upon the type of branch being probed according to equation A.6 and $V(J)$ is a rotational state dependence, given by equation A.7. [2]

$$
\begin{aligned}
R:&\ h^{(1)} = -J/(J(J+1))^{\frac{1}{2}} \\
P:&\ h^{(1)} = (J+1)/(J(J+1))^{\frac{1}{2}}
\end{aligned}
\tag{A.6}
$$

$$V(J) = \sqrt{\frac{(2J+3)(2J-1)}{J(J+1)}} \tag{A.7}$$

Table A.1: Summary of h factors for P, Q and R branches.[2]

	Q	P	R
$h^{(2)}$	$+1$	$-J/(2J+3)$	$-(J+1)/(2J-1)$
$h^{(1)}$		$-J/(J(J+1))^{\frac{1}{2}}$	$(J+1)/(J(J+1))^{\frac{1}{2}}$

Appendix B

Development of an Ultraviolet Continuous-wave Source

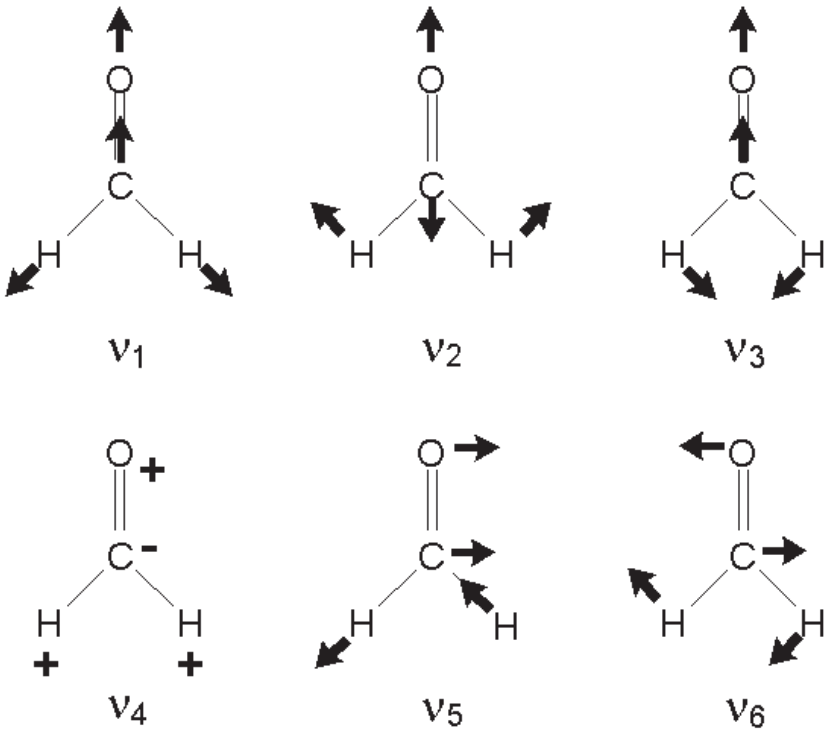

Figure B.1: Formaldehyde vibrational modes, reproduced from Bouwens *et al.*[3]

Appendix C

Vector Correlations in ICN Photodissociation at 266 nm

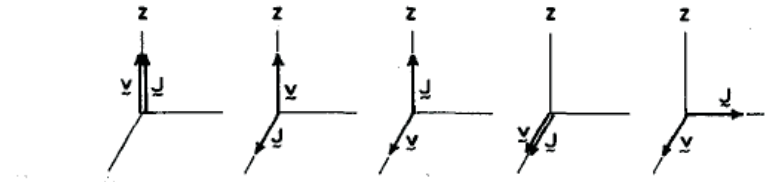

	(a)	(b)	(c)	(d)	(e)
$\beta_0^2(20)$	+1	+1	$-\frac{1}{2}$	$-\frac{1}{2}$	$-\frac{1}{2}$
$\beta_0^2(02)$	+1	$-\frac{1}{2}$	+1	$-\frac{1}{2}$	$-\frac{1}{2}$
$\beta_0^0(22)$	+1	$-\frac{1}{2}$	$-\frac{1}{2}$	+1	$-\frac{1}{2}$
$\beta_0^2(22)$	−1	$+\frac{1}{2}$	$+\frac{1}{2}$	$+\frac{1}{2}$	−1
$\beta_0^2(42)$	+1	$-\frac{1}{2}$	$+\frac{3}{8}$	$-\frac{1}{2}$	$+\frac{1}{8}$
$\beta_0^2(24)$	+1	$+\frac{3}{8}$	$-\frac{1}{2}$	$-\frac{1}{2}$	$+\frac{1}{8}$

Figure C.1: Dixon's A to E cases and the bipolar moments they represent, reproduced from Dixon.[1]

Amplitude in Dixon's limiting cases A to E are given by:

$$
\begin{aligned}
A &= \frac{1}{9}\left(1 + 2\beta_0^2(02) + 2\beta_0^2(20) + 2\beta_0^0(22) - 2\beta_0^2(22)\right) \\
B &= \frac{1}{9}\left(2 - 2\beta_0^2(02) + 4\beta_0^2(20) - 2\beta_0^0(22) + 2\beta_0^2(22)\right) \\
C &= \frac{1}{9}\left(2 + 4\beta_0^2(02) - 2\beta_0^2(20) - 2\beta_0^0(22) + 2\beta_0^2(22)\right) \\
D &= \frac{1}{9}\left(2 - 2\beta_0^2(02) - 2\beta_0^2(20) + 4\beta_0^0(22) + 2\beta_0^2(22)\right) \\
E &= \frac{1}{9}\left(2 - 2\beta_0^2(02) - 2\beta_0^2(20) - 2\beta_0^0(22) - 4\beta_0^2(22)\right)
\end{aligned}
\tag{C.1}
$$

reproduced from Hall and Wu.[4]

Table C.1: A-E fractions for Dixon's limiting cases for the rotational states measured in the (2,0) band.[1] The $*$ indicates an F_2 transition and † is taken from the literature.[2]

N	A	B	C	D	E
50†	0.03	0.77	0.12	0.02	0.06
50	-0.01	0.82	0.04	0.02	0.13
51	0.08	0.85	0.10	-0.08	0.05
52	0.08	0.75	0.10	0	0.06
53	0.07	0.63	-0.07	0.29	0.09
53$*$	0.13	0.81	0.02	0.06	-0.02
54$*$	0.05	0.91	0.01	0.01	0.0
55†	0.04	0.80	0.10	0	0.04
55	0.10	0.81	0.01	0.09	-0.01
56	0.06	0.70	0.14	0	0.11
56$*$	0.11	0.79	0.04	0.01	0.05
57	0.04	0.89	-0.02	0.14	-0.04

Table C.2: A-E fractions for Dixon's limiting cases for the rotational states measured in the (3,1) band.[1]

N	A	B	C	D	E
38	0.04	0.87	0.02	0.04	0.03
45	0.04	0.77	0.01	0.11	0.07
48	0.06	0.87	0.03	0	0.05
50	0.08	0.92	0.08	-0.08	0.01

References

[1] R. N. Dixon, The Journal of Chemical Physics **85**, 1866 (1986).

[2] M. L. Costen and G. E. Hall, Physical chemistry chemical physics : PCCP **9**, 272 (2007).

[3] R. J. Bouwens et al., The Journal of Chemical Physics **104**, 460 (1996).

[4] G. E. Hall and M. Wu, The Journal of Physical Chemistry **97**, 10911 (1993).